Study of the Mechanism of Nucleation in the Polluted Atmospheric Boundary Layer

A DISSERTATION
SUBMITTED TO THE FACULTY OF
UNIVERSITY OF MINNESOTA
BY

Modi Chen

IN PARTIAL FULFILLMENT OF THE REQUIREMENTS
FOR THE DEGREE OF
DOCTOR OF PHILOSOPHY

Peter H. McMurry

April 2013

Table of Contents

List of Tables iii
List of Figures iv
Chapter 1: Introduction 1
1.1 Review of atmospheric nucleation 1
1.2 Thesis overview 5
Chapter 2: Charge- and Material-Dependent Detection Efficiencies of Six Condensation Particle Counters for 1 to 7 nm Particles 10
2.1 Introduction 10
2.2 Experiment methods 12
2.2.1 Experiment setup and materials 12
2.2.2 CPC operation conditions 15
2.2.3 Detection efficiency fitting 19
2.3 Results and discussion 22
2.3.1 Detection efficiencies and cut-sizes 22
2.3.2 Influence of working fluid on particle detection 26
2.3.3 Particle composition effects 29
2.3.4 Influence of particle charging state 33
2.3.5 Impact of CPC operation conditions 38
2.4 Summary 40
Chapter 3: Time and Size Resolved Growth Rates for 1-5 nm Freshly Nucleated Particles in Atlanta 41
3.1 Introduction 41
3.2 Field measurements and observations 43
3.2.1 DEG SMPS 43
3.2.2 DEG Data inversion 46
3.2.3 Cluster CIMS measurement 51
3.2.4 Nucleation events during NCCN 52
3.3 Steady state growth rate 56
3.3.1 Size dependent growth rate 58
3.3.2 Size dependent growth enhancement 62
3.3 Summary 66
3.4 Supporting Information 68
3.4.1 Steady state particle size distribution 68
3.4.2 Model development 70
3.4.3 Estimated uncertainties 73
Chapter 4: Chamber Study of Amine on Sulfuric Acid Particle Formation and Growth 78
4.1 Introduction 78
4.2 Experiment Setup 80

4.3 Results and discussion 83
4.3.1 Particle size distribution in amine and non-amine experiments 84
4.3.2 Growth enhancement factors for chamber experiments 89
4.4 Summary 93
4.5 Supporting information 95
4.5.1 Sulfuric concentration decay rates inside the chamber 95
4.5.2 Modal growth rate of particles formed inside the chamber 98
Chapter 5: An Acid-Base Chemical Reaction Model for Nucleation Rates in the Polluted Atmospheric Boundary Layer 100
5.1 Introduction 100
5.2 Experiments and instrumentation 105
5.3 Model development 106
5.4 Comparison of observed and predicted nucleation rates 120
5.5 Summary 123
5.6 Supporting information 126
S 5.6.1 Methods of calculating "observed nucleation rates" 126
Chapter 6: Future Work 129
6.1 Detection efficiency of atmospheric particles 130
6.2 Charging mechanism for particles around 1 nm 132
6.3 Validation and further development of the nucleation model 136
6.3.1 Effect of ammonia and amines in stabilizing sulfuric acid clusters 136
6.3.2 Formation of sulfuric acid trimer and tetramer 137
Bibliography 139

List of Tables

Table 2.1 Materials and charging polarities investigated in this study…….14

Table 2.2 Summary of CPC operation conditions…….……16

Table 2.3 Ion detection efficiencies (%)……19

Table 2.4 Summary of fitting results…….24

Table 2.5 Summary of cut sizes…….25

Table 3.1 Growth Laws for Gas-to-Particle Conversion……...……62

Table S4.1. Comparison between observed and calculated sulfuric acid decay rates…...97

List of Figures

Figure 2.1 Experiment setup for CPC detection efficiency study…….……14

Figure 2.2 Influence from charger ions on Airmodus detection efficiency……...18

Figure 2.3 Comparison between four different expressions for correlating modeled and measured size-dependent CPC detection efficiencies…… ……..22

Figure 2.4 Comparison of detection efficiencies for neutral NaCl particles measured with the UMN DEG and TSI 3025……..……27

Figure 2.5 Comparison of detection efficiencies for neutral W particles measured with the UMN DEG and TSI 3025……..……..27

Figure 2.6 Comparison of detection efficiencies for neutral Ag particles measured with the UMN DEG and TSI 3025…….…….28

Figure 2.7 TSI 3025 detection efficiency for neutral particles.……..29

Figure 2.8 UMN DEG detection efficiency for neutral particles……..30

Figure 2.9 TSI 3786 detection efficiency for neutral particles……..……30

Figure 2.10. TSI 3025 detection efficiency for sodium chloride particles……..……..34

Figure 2.11. UMN DEG detection efficiency for sodium chloride particles…….34

Figure 2.12 TSI 3786 detection efficiency for neutral and negatively charged sodium chloride particles……35

Figure 2.13. Airmodus A09 detection efficiency for sodium chloride particles……..….37

Figure 2.14 Airmodus A09 detection efficiency for tungsten particles……...……..37

Figure 2.15 Comparison between TSI 3025 and BNL 3025……...……..39

Figure 2.16 Comparison between UMN DEG and BNL DEG……..39

Figure 3.1 Schematic of the scanning mobility particle spectrometer system using the DEG CPC and a booster butanol CPC (the DEG SMPS)…….....….45

Figure 3.2 DEG CPC activation efficiencies of positively charged 1.47 nm tetraheptyl ammonium ions and the number concentrations of the self-nucleated particles as a function of the saturator-condenser temperature difference……49

Figure 3.3 DEG CPC activation efficiencies of 1 to 6 nm sodium chloride particles carrying a single negative charge……50

Figure 3.4 Size-dependent particle transport efficiencies in the sampling lines, bipolar charging efficiencies (fractions of negatively charged particles carrying a single charge), nanoDMA penetration efficiencies, DEG CPC penetration efficiencies, and the transfer function of the nanoDMA with a fixed DMA voltage for 1.47 nm particles…..…….51

Figure 3.5 Composite contour plot of particle number size distributions measured by the PSD (top, 9–200 nm) and by the DEG SMPS (bottom, 1–9 nm) during atmospheric nucleation events on Aug 23, 2009…….53

Figure 3.6 Aerosol size distribution measured with three instrument systems during nucleation events in Atlanta, GA on August 23, 2009……..54

Figure 3.7 Observed growth rates and corresponding uncertainties as a function of particle geometric diameter $D_{p,geometric}$ for NPF events measured on 7 August 2009 (NCCN)…….……..60

Figure 3.8 Values of the growth rate enhancement Γ and their corresponding uncertainties are plotted as a function of particle geometric diameter $D_{p,geometric}$ for the NPF event observed on 7 August 2009 (NCCN)……64

Figure 3.9 Summary of Γ values for all 34 measurements during NCCN..……..65

Figure S3.1 Time-dependent particle number concentrations at various particle geometric diameters D_p for collision-controlled nucleation in the free-molecular regime for a system that is initially particle free……69

Figure S3.2 Particle size distribution on 13:00, August 7 during NCCN…….…….....73

Figure 4.1 Schematic of the nucleation reaction chamber system…….....83

Figure 4.2 Particle size distributions in (a) a non-amine experiment; (b) an amine experiment; and (c) a collision-limited simulation……..……86

Figure 4.3 Growth rate enhancement factor Γ at 1.1 nm…..……..91

Figure 4.4 Growth rate enhancement factor Γ as a function of particle diameter…….92

Figure S4.1 Sulfuric acid decay rates during four experiments after UV lights turned off.……97

Figure S4.2 Particle modal growth rate as a function of sulfuric acid monomer concentration during chamber experiments……99

Figure 5.1 Dependence of nucleation rates ($J = J_{1\ nm}$) in the atmospheric boundary layer on [H_2SO_4]……..…102

Figure 5.2 Observed dimer, trimer, and tetramer concentrations versus collision-limited values……..…108

Figure 5.3 Ratio of steady-state dimer to monomer concentrations (m/z 195/160) as a function of total amine concentration in chamber experiments……..…113

Figure 5.4 Comparison of measured (vertical axes) and modeled (horizontal axes) concentrations of dimer……..…114

Figure 5.5 Comparison of measured (vertical axes) and modeled (horizontal axes) concentrations of trimer……116

Figure 5.6 Conceptual acid–base reaction model for nucleation……120

Figure 5.7 Comparison of observed and calculated (Eq. 18) atmospheric nucleation rates……..……..122

Figure 5.8 Comparison of observed and calculated (Eq. 18) atmospheric nucleation rates……123

Figure 6.1 Detection efficiency of UMN DEG of negative sodium chloride and silver particles with 1 to 3 nm size range……..……131

Figure 6.2 Experiment setup for charging efficiencies of particles of different composition.……..……...…….134

Chapter 1: Introduction

1.1 Review of atmospheric nucleation

Atmospheric aerosol particles range in size from as small as a nanometer to as large as several microns. These particles can affect human health, visual air quality and climate (Wichmann and Peters 2000, Stieb et al. 2002, Menon et al. 2002, Lohmann and Feichter 2005, Andreae and Rosenfeld 2008, Leaitch et al. 2010). Nucleation, meaning the formation of these particles from gas phase precursors and their subsequent growth by the uptake of gas phase chemicals, has been shown to contribute significantly to the increase atmospheric aerosol number concentrations and also affects aerosol size distributions (Kuang et al. 2008, Nieminen et al. 2009, Jiang et al. 2011c, Spracklen et al. 2008b, Adams and Seinfeld 2003, Zhang, Wen and Jang 2010b). When aerosol particles grow to sizes that exceed 50 to 100 nm, they are able to serve as cloud condensation nuclei (CCN). Recent research shows that boundary layer nucleation can be an important potential source for global CCN (Lihavainen et al. 2003, Laaksonen et al. 2005, Kerminen et al. 2005, Spracklen et al. 2008b, Pierce and Adams 2009, Pierce and Adams 2007). This could alter the cloud albedo and ultimately the Earth's radiation balance (Leaitch et al. 2010, Ghan et al. 2001). This effect of aerosols is the largest source of

uncertainty in current global climate models (Gong, Stroud and Zhang 2011, Kazil et al. 2010, Liao et al. 2009), and our imperfect understanding of nucleation contributes significantly to these uncertainties.

In the atmospheric boundary layer, most nucleation events occur following a marked increase in sulfuric acid vapor concentrations. Sulfuric acid vapor is formed when the hydroxyl radical reacts with a sulfur-containing gas (usually sulfur dioxide), a process that is photochemically initiated. The formation of new particles leads to a large increase in the concentrations of particles smaller than 10 nm (Weber et al. 1996, Fiedler et al. 2005, Sihto et al. 2006). The first atmospheric nucleation study can be traced back to the beginning of the last century. With his extraordinary intuition, John Aitken (Aitken 1911) pointed out the possible connection between atmospheric nucleation and gas phase sulfate concentrations. In this pioneering work, Aitken carried out measurements of particle concentrations with his portable Aitken Particle Counter (Aitken 1911). Since then, aerosol scientists have been working on establishing a detailed understanding and accurate parameterization of the nucleation process. Atmospheric measurements have been carried out all around the world with modern instruments, from the remote boreal forest (Kulmala et al. 1998, Makela et al. 2001), to urban areas (Vakeva et al. 2000, Woo et al. 2001, O'Dowd et al. 2002b, Iida et al. 2008, Jiang et al. 2011b, Jiang et al. 2011c), and to coastal environments (O'Dowd et al. 1999). Weber et al. (Weber et al. 1996) found that nucleation rates for 3 nm particles in the atmospheric boundary layer vary in proportion to $[H_2SO_4]^p$, ($1<p<2$). Similar results, sometimes with $p>2$, were obtained

later in various locations with better instrumentation (Sihto et al. 2006, Riipinen et al. 2007, Boy et al. 2008, Kuang et al. 2008, Nieminen et al. 2009, Paasonen et al. 2009, Jokinen et al. 2012, Wang et al. 2011). Weber and coworkers also showed that the growth rates (GR) of newly formed atmospheric particles were usually larger than the GR due to sulfuric acid condensation alone (Weber et al. 1997, Weber et al. 1998). This is also confirmed by recent studies (Boy et al. 2005, Stolzenburg et al. 2005, Smith et al. 2008, Svenningsson et al. 2008, Dal Maso et al. 2005, Kuang et al. 2012b). Conditions for the aerosol aerosols to survive as they grow, rather than being scavenged by preexisting particles, have been discussed independently by McMurry and coworkers (McMurry and Friedlander 1979, McMurry et al. 2005, Kuang et al. 2010) and Kerminen and coworkers (Kerminen, Pirjola and Kulmala 2001). The competition between their GR from gas phase chemicals and scavenging rates by preexisting aerosols is one of the most important factors that determine the survival probability of newly formed particles. GR has been previously estimated by tracking the change of the particle modal GR over time (Stolzenburg et al. 2005). Kuang and coworkers (Kuang et al. 2012b) recently showed that GR depends both on particle size and time of the day. By taking an averaged modal GR, one can overestimate particle surviving probability by about a factor of two.

The mechanism of atmospheric nucleation in various environments and conditions, though, is still unclear to modern aerosol scientists. The multi-component classical nucleation theory (Vehkamaki et al. 2002, Merikanto et al. 2007) is often used to model nucleation in the atmosphere. This theory estimates nucleation rate by taking into account

the change of Gibbs free energy associated with forming the critical nucleus from its gas-phase constituents. However, this theory does not give the same dependence of nucleation rates on sulfuric acid concentrations as is observed in the atmosphere. Also the nucleation rates predicted are orders of magnitude lower (Chen et al. 2012).

Both atmospheric particle GR and nucleation rates are higher than can be explained by sulfuric acid alone, suggesting other species must also be involved. Since it's ubiquitous and reacts rapidly with sulfuric acid (Nowak et al. 2006), ammonia has generally been considered as a likely participant in atmospheric nucleation. Laboratory studies have also shown that adding ammonia to the binary sulfuric acid and water system can enhance the nucleation rate significantly (Zollner et al. 2012, Ball et al. 1999, Kirkby et al. 2011, Benson et al. 2011). Recently, more attention has been focused on the role of amines in affecting particle formation and growth rates. Smith and coworkers have developed and used the thermal desorption chemical ionization mass spectrometer (TDCIMS) to study the chemical composition of ambient particles during nucleation events in urban, rural, and remote areas (Smith et al. 2010, Smith et al. 2005, Smith et al. 2008). They found that signals corresponding to amines and organic acids increase in relative intensity during nucleation events. This observation implies the existence of aminium salts, formed by reactions of organic bases (amines) and organic acids. Laboratory experiments have also shown that nucleation rates of sulfuric acid are also significantly enhanced when amines are present, and this effect seems to be stronger for amines than for ammonia (Zollner et al. 2012, Yu, McGraw and Lee 2012). Recent quantum chemistry calculations

support this observation. By calculating the their formation free energies, Ortega and coworkers (Ortega et al. 2012) found that ammonia and dimethylamine form stable clusters with sulfuric acid.

My contribution mainly focuses on three topics: (1) characterizing condensation particle counters (CPCs) for accurate particle measurements down to 1 nm, the size close to the smallest stable sulfuric acid clusters; (2) developing a method of estimating time and size resolved particle growth rates and atmospheric nucleation rates based on data from both atmospheric and laboratory studies; (3) deriving of a simple semi-empirical acid-base reaction model for atmospheric nucleation in the polluted atmospheric boundary layer.

1.2 Thesis overview

In chapter 2, results of laboratory calibrations of the most 1 nm condensation particle counters (CPCs) developed over the past years are discussed. This study involves collaborations with researchers from the University of Helsinki, Brookhaven National Laboratory, the University of Paris and TSI, Inc. It includes a comprehensive study of CPC responses to sodium chloride, tungsten and silver particles from 1 nm to 7 nm with positive one, zero, and negative one charge. Ion clusters of tetraheptylammonium bromide (THABr, $N^+[C_7H_{15}]_4$), tetradodecylammonium bromide (TDDAB, $N^+[C_{12}H_{25}]_4$) as well as air ions generated by ionizing radiation in a Po 210 "neutralizer" are also studied. This study shows that CPC detection efficiencies are very sensitive to particle

composition and charge state for particles smaller than 3 nm in diameter. A new three-parameter fitting equation is developed to describe CPC performance. Aspects of this work have been published in Jiang et al. (2011b) and Kuang et al. (2012a).

In chapter 3, results from the field study "nucleation and cloud condensation nuclei" (NCCN) carried out in Atlanta, Georgia, during July and August 2009 are discussed. In this study, the scanning mobility particle spectrometer equipped with a diethylene glycol (DEG) CPC (the DEG SMPS) that was developed in Professor McMurry's laboratory, together with conventional particle instrumentation (Woo et al. 2001), was used to measure particle size distributions over the 1 to 500 nm range. Measurements with the NCAR cluster chemical ionization mass spectrometer (cluster CIMS) extends these measurements of number distributions down to one sulfuric acid molecule. These measurements represent the first measurements of the complete particle size distribution down to one molecule. By fitting the general dynamic equation to the steady state particle size distribution, a novel method of calculating time and size resolved GR for particles in the 1 to 5 nm range is derived. The growth enhancement factors (Γ), defined as the ratio between the actual GR and GR due to sulfuric condensation only, are around one at 1 nm for most cases, and increased as particle size increased. This indicates that while sulfuric acid condensation can usually explain all of the growth for 1 nm particles, additional compounds must also contribute to growth for particles larger than 1 nm. Although these measurements cannot identify the compounds that contribute the additional growth, they clearly demonstrate a process that needs to be explained by chemical models for growth

rates of atmospheric nanoparticles. Aspects of this work have been described by Kuang et al. (2012b) and by Chen et al. (2012). This is the first time that the size- and time-dependent growth rates of nanoparticles were measured.

In chapter 4, results from a chamber study carried out in Professor McMurry's laboratory in 2010 are discussed. This study aims at specifying the role of amines during nucleation in the presence of sulfuric acid. By adding gaseous amine into the reaction chamber, nucleation enhancement was observed. Steady state ratios of sulfuric dimer to monomer concentrations were also observed to increase as amine concentrations increased. The same method of estimating GR and Γ as discussed in chapter 3 was applied to these chamber data. In contrast to the atmospheric observations, where clusters that contained four or more sulfuric acid molecules were stable (i.e., did not evaporate to a measureable extent), small particles formed in the chamber appeared to be less stable. Growth rates were below the sulfuric acid condensation rate even for particles as large as 3 nm. Possible reasons including wall deposition, insufficient charging, and evaporation of small nucleated particles are discussed. Systematic errors during this study and their impact on our results are estimated. Aspects of this work have been described by Chen et al. (2012).

In chapter 5, a simple acid-base chemical reaction model for nucleation rates based on data from Atlanta and the Chamber study is developed. A paper describing this work was recently published in the *Proceedings of the National Academy of Sciences* (Chen et al.,

2012). Concentrations of sulfuric acid clusters were measured with the cluster chemical ionization mass spectrometer (cluster CIMS), a prototype instrument built specifically for this study by Dr. Mari Titcombe with the assistance of Dr. Fred Eisele (NCAR). Using these data together with a simple kinetic model for cluster formation and loss, evaporation rate constants were estimated. These evaporation rate constants allowed the development a chemical model for nucleation rates driven by reactions between sulfuric acid and basic gases. This model predicts that nucleation rates equal the sulfuric acid vapor collision rate times a prefactor that is less than unity and that depends on the concentrations of basic gaseous compounds (ammonia plus amines) and preexisting aerosols. While previous models differ from observations by many orders of magnitude, predicted nucleation rates from this model and their dependence on sulfuric acid vapor concentration are in reasonable agreement (±10X) with measurements from Mexico City and Atlanta.

In chapter 6, three unsolved problems are discussed: (1) detection efficiency of atmospheric particles with CPCs; (2) size-dependent steady state bipolar charged fraction of particles smaller than 3 nm; (3) validation and further development of the nucleation model introduced in Chapter 5. The first two questions are related to assumptions we made in inverting the atmospheric measurement data. And the last question comes from the simplifying assumptions we made for the nucleation model discussed in chapter 5: large variations still exist in predicted nucleation rates that cannot be explained solely by reactions of ammonia and amines with sulfuric acid. This indicates that other chemicals

also play a role. Identifying those compounds and quantifying their roles on nucleation rates is an important next step towards elucidating the mechanism of atmospheric nucleation.

Chapter 2: Charge- and Material-Dependent Detection Efficiencies of Six Condensation Particle Counters for 1 to 7 nm Particles*

2.1 Introduction

Condensation Particle Counters (CPCs) are widely used to detect small aerosol particles (McMurry 2000). Unlike electrical methods (Flagan 1998), which require particles to be charged, CPCs can detect neutral particles as well. Furthermore, because CPCs detect individual particles, exceedingly low concentrations can be measured. However, for several decades it has been recognized that for particles smaller than about 10 nm, CPC detection efficiencies decrease with decreasing particle size (Liu and Kim 1977). It is now known that size-dependent counting efficiencies are affected by instrument design (Gamero-Castaño and de la Mora 2000, Stolzenburg and McMurry 1991), particle composition (Stolzenburg and McMurry 1991), particle charge (Wilson 1899, Winkler et

* Aspects of the results described in this chapter (including some text and figures) have been published in Jiang et al. (2011b) and Kuang et al. (2012a).

al. 2008), and properties of the condensing vapor, frequently referred to as the "working fluid" (Magnusson et al. 2003, Iida, Stolzenburg and McMurry 2009). Until recently, the smallest size that could be detected by commercial CPCs was 2.5 to 3 nm (Stolzenburg and McMurry 1991, Hering et al. 2005). Laboratory prototype instruments that detect particles smaller than 2 nm have been described (Kim, Okuyama and de la Mora 2003, Sgro and de la Mora 2004). Iida and coworkers showed that diethylene glycol (DEG) is effective at activating particles as small as 1 nm (Iida et al. 2009) and a mixing-type CPC that uses DEG as the working fluid, the Airmodus 09, was recently commercialized (Vanhanen et al. 2011). Kuang et al. (2012a) recently showed that the minimum detection limits of laminar flow CPCs operated with both butanol and DEG could be reduced significantly by operating at higher saturator temperatures and higher flow rates than had been used previously.

Laboratory studies aimed at quantifying detection efficiencies of these CPCs for particles in the sub 10 nm size range have been reported. These studies included measurements with sodium chloride and silver particles for the TSI 3025 CPC (Kesten, Reineking and Porstendorfer 1991, Stolzenburg and McMurry 1991), sodium chloride, silver, and ammonium sulfate particles for the UMN DEG (Iida et al. 2009) and the TSI 3776 CPC (Mordas et al. 2008a), and silver and tungsten oxide for the Airmodus A09 (Vanhanen et al. 2011). In this study, we extend this work also to include instrument responses to neutral particles, which are especially important in atmospheric nucleation (Iida et al. 2008, Iida et al. 2006, Kulmala et al. 2007b, Laakso et al. 2004). Also this study

systematically compares the responses of these instruments using data obtained with the same apparatus and methods.

2.2 Experiment methods

2.2.1 Experiment setup and materials

The experiment setup showed in Figure 2.1 is based on the method for measuring CPC detection efficiencies originally reported by Liu and Pui (1974). Except for the components shown in the rectangular dashed box, which allow for measurements with electrically neutral particles, it is the same as the apparatus used by Kuang et al. (2012a). Reported CPC detection efficiencies are equal to the concentration detected by the CPC divided by the true concentration measured using the aerosol electrometer assuming that no multiply charged particles were present for these sub-8 nm particles (Fuchs 1963).

Table 2.1 summarizes the approach used to produce particles of varying composition. Filtered compressed air was used as carrier gas for tetra-alkyl ammonium and neutralizer ions. Pure nitrogen was used for all other materials. Particles were then charged inside a Po-210 neutralizer. For particles of sodium chloride, silver, and tungsten, complete detection efficiency curves were obtained from the minimum detectable size to around 7 nm. For tetra-alkyl ammonium ions, THABr monomer (1.47 nm mobility diameter) and

dimer (1.78 nm mobility diameter) and TDDAB monomer (1.70 nm mobility diameter) were studied (Ude and de la Mora 2005). Silver and tungsten wires were purchased from Good Fellow. Distilled water is used as the working fluid in the TSI 3786. Other chemicals including working fluids (DEG and butanol) and solvents (methanol) were all from Sigma Aldrich.

A high resolution differential mobility analyzer (HRDMA) (Rosser and de la Mora 2005) was used to select particles or ions of known electrical mobility. Two HEPA filters connected in series were used at the sheath flow inlet of the HRDMA to limit concentrations to < 0.1 cm^{-3} (measured by UMN DEG). The resolution of the HRDMA, which is defined as the ratio of the electrical mobility at the peak of the DMA transfer function to the width of the transfer function at half of its maximum value, was about 20 at 1.47 nm in this study. As an approximation, therefore, particles are assumed to be monodisperse. The HRDMA was calibrated using THABr positive ions daily after experiments to allow quantification of the relationship between HRDMA classifying voltage and mobility.

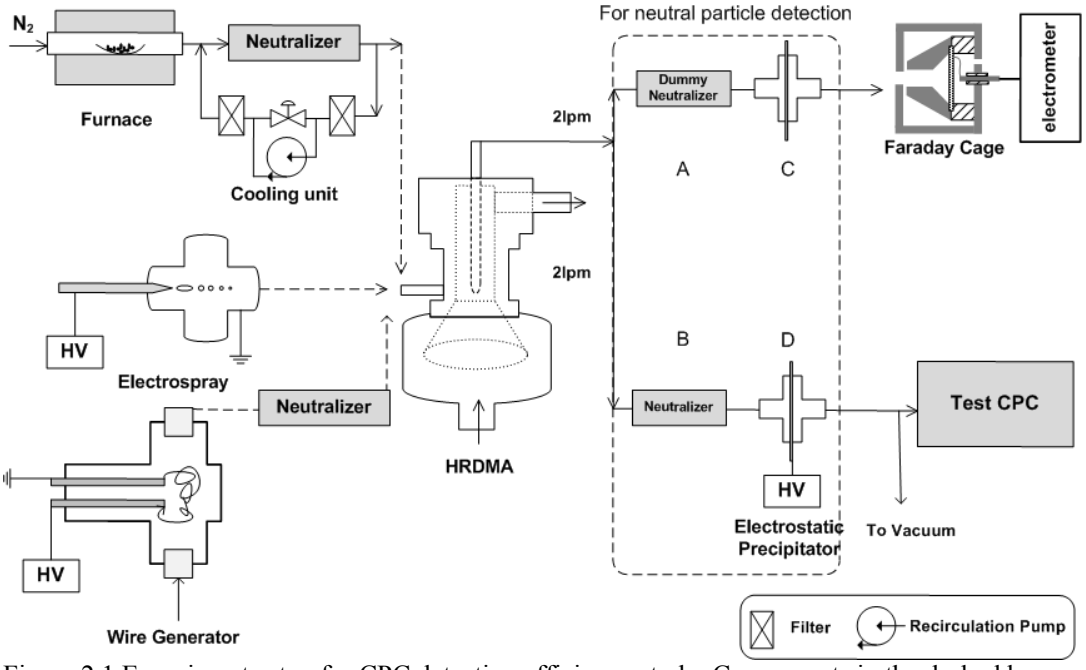

Figure 2.1 Experiment setup for CPC detection efficiency study. Components in the dashed box are for experiments with neutral particles.

Table 2.1. Materials and charging polarities investigated in this study[a].

Material Used	Generation Method	Reference
NaCl	Furnace	(Scheibel and Porstendorfer 1983)
THABr, TDDAB	Home-made Electrospray	(Ude and de la Mora 2005)
Ag	Wire Generator	(Peineke, Attoui and Schmidt-Ott 2006)
W	Wire Generator	(Peineke et al. 2006)

[a]Charger ions, which are not listed, were generated by radioactive decay inside the neutralizer.

For neutral particle detection, a second neutralizer and an electrostatic precipitator (ESP) were put in line before the test CPC. Mobility-classified particles were sent through the neutralizer, where over 95% of the aerosol particles below 8 nm became neutral (Wiedensohler 1988). The ESP then removed all the remaining charged particles so that only neutrals were sampled by the test CPC. A dummy neutralizer (the same neutralizer housing without radioactive material) and a dummy ESP (ESP without applied voltage) were used for the aerosol that flowed to the aerosol electrometer. Tubing dimensions and

aerosol flow rates for the parallel flows to the electrometer and test CPC were also equal, to ensure that both detectors were equally affected by diffusional deposition. The difference due to the removal of charged particles was corrected during data processing. Particle concentrations detected by CPCs in this study were maintained between 1000 cm^{-3} to 10000 cm^{-3} except for the smallest sizes, where concentrations were lower. All experiments were carried out at ambient pressure (about one atmosphere).

Following Iida et al. (2009), a TSI 3760 CPC was used as a "booster" to detect particles downstream of the UMN DEG, BNL DEG, and the Airmodus A09 CPCs. The booster is needed because, due to its relatively low vapor pressure, DEG does not grow particles sufficiently to enable them to be easily detected by light scattering. However, DEG is very effective at growing the smallest particles (~1 nm) to a size (~100 nm) that can easily be detected by the booster.

2.2.2 CPC operation conditions

Table 2.2 summarizes CPC operating conditions used in this study. The default settings suggested by the manufacturer were used for the TSI 3025 and TSI 3786. The UMN DEG was operated using the conditions described by Jiang et al. (2011b). Charged particles for Airmodus A09 were measured using the CPC operating conditions described by Vanhanen et. al. 2012, but with the mixing ratio (R) of 0.11. Mixing ratio of Airmodus A09 is defined as the mixing flow divided by the condenser flow. As listed in Table 2.2,

R=(condenser flow rate-aerosol flow rate)/condenser flow rate. Below 0.3, higher mixing ratio indicates higher saturation ratio for Airmodus A09. The BNL 3025 and BNL DEG were operated as described in Kuang et al. 2012 (a).

Table 2.2 Summary of CPC operation conditions.

CPC Name	Working Fluid	Condenser Flow Rate	Aerosol Flow Rate	Saturator Temp.	Condenser Temp.	Reference
TSI 3025	Butanol	0.3 LPM	0.03 LPM	37 ^{o}C	10 ^{o}C	Manual[c]
TSI 3786	Water	0.3 LPM	0.3 LPM	12 ^{o}C	75 ^{o}C[b]	Manual
UMN DEG	DEG	0.3 LPM	0.03 LPM	59 ^{o}C	20 ^{o}C	Iida et al. 2009
Airmodus A09	DEG	2.8 LPM[a]	2.5 LPM	72.5 ^{o}C	0 ^{o}C	Vanhanen et al. 2011
BNL 3025	Butanol	0.47 LPM	0.043 LPM	44 ^{o}C	10 ^{o}C	Kuang et al. 2012
BNL DEG	DEG	0.93 LPM	0.083 LPM	70 ^{o}C	20 ^{o}C	Kuang et al. 2012

[a] This value is for mixing ratio 0.11 of Airmodus A09.
[b] This is the temperature of the growth tube for the TSI 3786.
[c] TSI 3025 and TSI 3786 CPCs are calibrated according to their default settings from the manual.

In determining the CPC operating conditions, it is important to ensure that their detection of ions is suppressed, especially for CPCs with 1 nm particle detection ability since mobility diameters of air ions are also in this range. This has been previously discussed for laminar flow CPCs (Kuang et al. 2012a, Jiang et al. 2011b). Those studies show that air ions of a given mobility (i.e., ions produced by ionizing radiation in a bipolar charger) are detected with lower efficiency than sodium chloride or silver particles of the same mobility. However, if the CPC saturation ratio is too high, both air ions and particles can be efficiently detected. Therefore, to improve the likelihood that counts are from particles and not ions, saturation ratios for these instruments are usually set to levels where the particles are detected with reasonable efficiency but the air ions are not. An example is shown in Figure 2.2. Positive neutralizer ion detection efficiencies in mixing ratios of

0.11 (blue symbols) and 0.29 (red symbols) are compared. The detection efficiency of positive ions with mixing ratio of 0.11 is negligible. For the mixing ratio of 0.29, which results in a maximum saturation ratio of approximately 10 (Vanhanen et al. 2011), positive air ions from the charger are detected with efficiencies of 30%~40%. When the detection efficiencies of positive sodium chloride particles are characterized with a neutralizer (as shown in Figure 2.1), where high concentration of positive air ions are generated, the influence from these air ions is hard to avoid. As a result, instead of decreasing smoothly towards zero, the slope of the detection efficiency curve obtained for the mixing ratio of 0.29 exhibits an infraction at about 1.5 nm, where the peak concentration of positive charger ions lie. Most likely, at these small sizes both positive ions and sodium chloride particles are detected by the instrument, and thus both particles and ions influenced the calibration result.

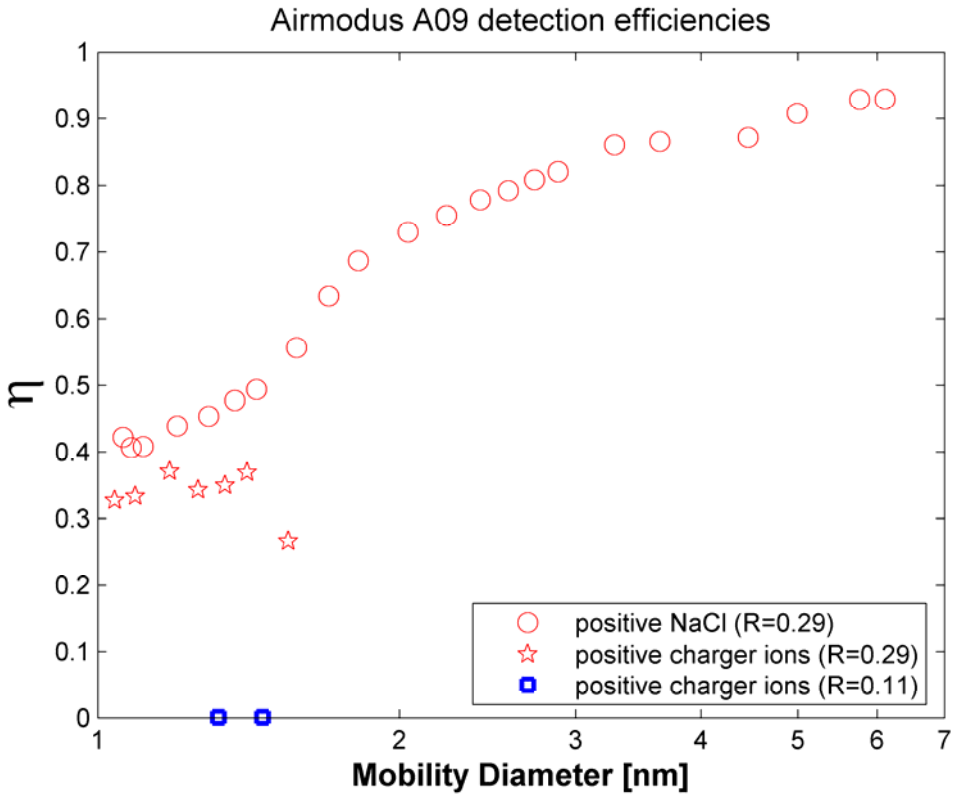

Figure 2.2 Influence from charger ions on Airmodus detection efficiency. Red symbols are for mixing ratio (R) of 0.29. Blue symbols are for R=0.11.

Ion detection efficiencies for CPCs (operated as in Table 2.2) in this study are listed in Table 2.3. The values for air ions generated from the charger are all below 0.1%. For tetra-alkyl ammonium ions, the efficiencies are all below 0.5%, except for BNL 3025. These low detection efficiencies mean that, even when these CPCs are used in an environment with high concentration of ions, most signals will still be from particles. This can significantly reduce the influence from the ions when interest is mainly focused on particles. By operating the CPCs in this way, we ensured that the problem shown in Figure 2.2 did not occur during this study. The calibration results for particle detection efficiency are valid even when the concentration of air ions cannot be neglected.

Table 2.3 Ion detection efficiencies (%).

	THABr monomer (1.47nm)[a]	THABr dimer (1.78nm)	TDDAB monomer (1.70nm)	Positive Air ion (1.4nm)	Negative Air ion (1.1nm)
TSI 3025	0	0.03	0.09	0	0
UMN DEG	0	0.11	0.17	0	0
TSI 3786	0	0.01	0.02	0	0
Airmodus A09[b]	0.02	0.11	0.37	0.1	0.02
BNL DEG	0	0.46	0.18	0	0
BNL 3025	0	2.59	3.83	0.08	0

[a] Diameters listed in this table are all mobility diameters.
[b] Airmodus A09 is operated in the condition of 0.11 mixing ratio.

2.2.3 Detection efficiency fitting

Several different empirical equations have been presented in the literature for fitting measured size-dependent detection efficiencies. Stolzenburg and McMurry employed a two parameter fitting equation for the activation efficiency (without explicitly taking diffusion losses into account) of the TSI 3025 CPC (Stolzenburg and McMurry 1991):

(1) $\eta(D_p) = 1 - e^{-\ln(2)(D_p - A_0)/(A_{50} - A_0)}$

where activation efficiencies are 50% at diameter A_{50} and go to zero at A_0. Implicit in this expression is that activation efficiencies approach unity as particle size goes to infinity. Mertes and coworkers proposed the following three parameter fitting equation, which they applied to the TSI 3010 CPC (Mertes, Schroder and Wiedensohler 1995):

(2) $\eta(D_p) = 1 - a \cdot (1 + e^{(D_p - D_1)/D_2})^{-1}$

In this equation, a, D_1, and D_2 are three free parameters. The minimum detectable size D_0 is determined by setting $\eta(D_p) = 0$, $D_0 = D_2 \ln(a-1) + D_1$. Later, Hering and Stolzenburg (2005) used equation (3) to describe the detection efficiency of the TSI 3785 water CPC.

$$(3)\quad \eta(D_p) = (1 - \frac{a}{D_p \ln D_p})(1 - e^{\frac{D_0 - D_p}{D_1}})$$

where D_1, D_0, and a are free parameters. This equation conditions the asymptotic limit of the detection curve with the parameter "a", thus agrees better with more CPC data. However, compared with equation (1), where parameters A_0 and A_{50} directly indicate the detection ability of the CPC, parameters D_1 and a in equation (3) do not provide any insight into processes that affect activation by themselves.

In this work, we propose the following new three-parameter equation, which incorporates the advantages of both equation (1) and equation (3). It well agrees with data points for different types of CPCs and its fitting parameters are physically meaningful.

$$(4)\quad \eta(D_p) = \eta_{act}(D_p) \cdot \eta_{dif}(D_p)$$

$$\eta_{act}(D_p) = 1 - 2^{(\frac{A_0 - D_p}{A_{50} - A_0})}$$

$$\eta_{dif}(D_p) = 1 - 5^{\frac{2}{3}} \cdot \frac{1 - P_{5nm}}{D_p^{\frac{2}{3}}}$$

In equation (4), $\eta_{act}(D_p)$ is an empirical expression for the activation efficiency, and $\eta_{dif}(D_p)$ is a first order approximation solution for effects of diffusional deposition on particle penetration in laminar tube flows (Gormley 1948). A_0 and A_{50} are the diameters

where 0% and 50% particles can be activated (the same as defined in Eq. 1), and P_{5nm} is the penetration for 5 nm particles. These three fitting parameters are determined numerically by fitting the equation to the experimental data. For most cases in this study, P_{5nm} is approximately the same as $\eta(5nm)$.

We have fitted each of the above functional forms to measured detection efficiencies and conclude that Eq. (4) provides the best overall fit. Typical R^2 values (defined as the ratio of the sum of squares of the regression and the sum of squares about the mean) for this fitting method are greater than 0.98. An example of comparison between different fitting methods is shown in Figure 2.3 for the Airmodus A09 CPC with negative sodium chloride particles. Mertes' and Stolzenburg's fitting equations cannot describe the detection curve in this case. Though Hering's fitting equation also agrees with this data quite well, finding the right initial values for its fitting parameters is tricky. For these reasons, Eq. (4) is used for fitting detection efficiency data in following sections.

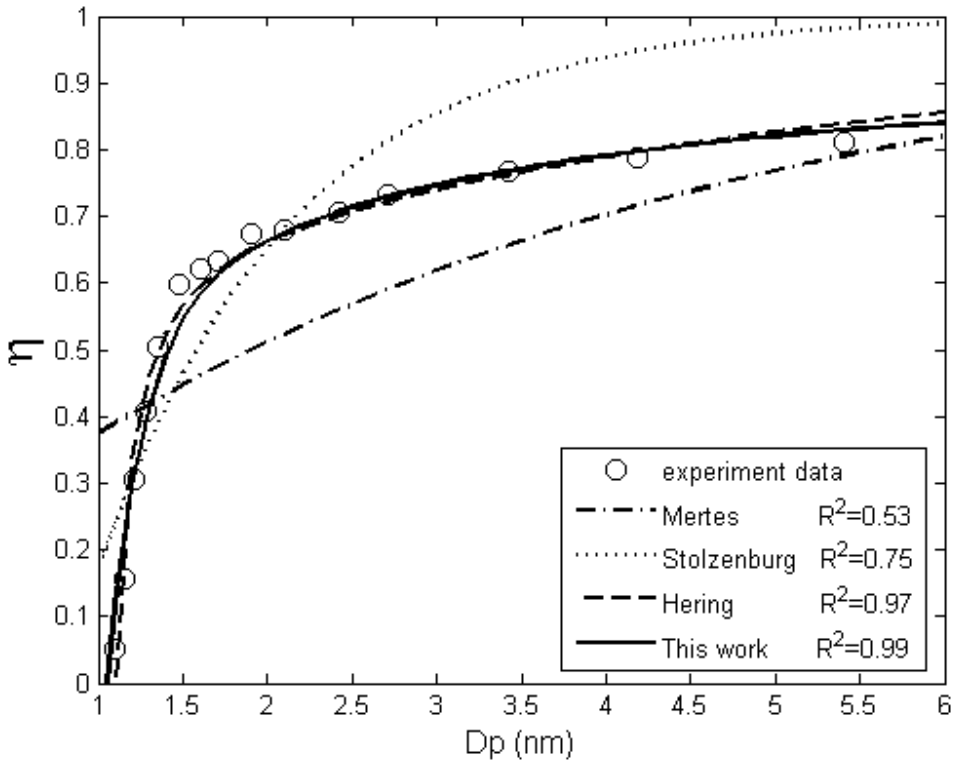

Figure 2.3 Comparison between four different expressions for correlating modeled and measured size-dependent CPC detection efficiencies. Stolenburg's fitting method is for activation efficiency, thus alone, it cannot well describe the detection efficiency curve. Hering's fitting and the method proposed in this work both agree with the experiment data well. However, it is difficult to determine the initial values for the fitting parameters in Hering's method.

2.3 Results and discussion

2.3.1 Detection efficiencies and cut-sizes

Table 2.4 summarizes all the fitting results for CPCs studied in this research. Ideally, the value of P_{5nm} should be the same for a given CPC regardless of particle material or

charging state. Since Eq. (4) is still an empirical approximation and cannot decouple the activation and diffusion processes exactly, P_{5nm} varies by about 10% for a given CPC as shown in table 2.4. A_0 and A_{50} values in the same table show the activation abilities of the CPCs. Since detection efficiencies of CPCs, are affected by particle diffusional deposition as well as activation, we also introduce cut-sizes (D10, D50, and D80) in table 2.5, which are defined as the mobility diameters that 10%, 50% and 80% particles can be detected, to better illustrate instrument performance. (Note, D0, which is not shown here, is the same as A_0 by definition, since the diameter where no particle can be activated is also the diameter where no particles can be detected.) These values are determined by setting $\eta(D_p)$ in Equation (4) equal to 0.1, 0.5 and 0.8 respectively.

Relative uncertainties of the results are estimated from the counting statistical error by the CPC and the variance of the electrometer signal during the two-minute sampling time for each data point. For sodium chloride and tungsten particles, relative uncertainties are around 4%. For silver, the variance of the electrometer signal is large since the silver concentration produced by wire generator is relatively unstable. Overall relative uncertainties for silver particles range from 10% to 15%. In order to present data clearly, relative uncertainties are only illustrated on Figure 2.7, Figure 2.11, and Figure 2.12 in following sections. Since uncertainties are determined from particle signal level and stability, relative uncertainty levels for the same material of different instruments are similar.

Table 2.4 Summary of fitting results.

	NaCl			**W**			**Ag**		
TSI 3025	**+**	**-**	**0**	**+**	**-**	**0**	**+**	**-**	**0**
A_0 [nm]	1.95	1.70	2.27	2.00	1.94	2.10	2.50	2.38	2.69
A_{50} [nm]	2.44	2.16	2.72	2.56	2.44	2.54	2.83	2.76	3.01
P_{5nm}	0.81	0.72	0.80	0.76	0.73	0.76	0.89	0.82	0.79
UMN DEG									
A_0 [nm]	1.47	1.09	1.31	1.50	1.24	1.27	1.80	1.78	2.06
A_{50} [nm]	1.86	1.67	1.43	1.84	1.76	1.50	2.18	2.12	2.45
P_{5nm}	0.80	0.78	0.68	0.79	0.80	0.80	0.85	0.80	0.80
TSI 3786									
A_0 [nm]	1.69	1.43	1.41	2.26	2.16	2.36	2.65	2.79	2.75
A_{50} [nm]	2.07	1.63	1.60	2.65	2.40	2.75	3.24	3.50	3.27
P_{5nm}	0.91	0.81	0.84	0.82	0.81	0.84	0.87	0.85	0.82
Airmodus A09 [a]									
A_0 [nm]	1.28	1.05		1.54	1.26				
A_{50} [nm]	1.42	1.18		1.62	1.45				
P_{5nm}	0.82	0.82		0.80	0.82				
BNL 3025									
A_0 [nm]	1.53	1.12		1.62	1.45				
A_{50} [nm]	2.20	1.67		2.02	1.93				
P_{5nm}	0.90	0.82		0.80	0.80				
BNL DEG									
A_0 [nm]	1.42	0.86		1.51	1.35				
A_{50} [nm]	1.65	1.31		1.68	1.55				
P_{5nm}	0.90	0.87		0.83	0.83				

[a] Airmodus A09 results shown here are for the mixing ratio of 0.11.

Table 2.5 Summary of cut sizes.

	NaCl			W			Ag		
3025	**+**	**-**	**0**	**+**	**-**	**0**	**+**	**-**	**0**
D10 [nm]	2.07	1.87	2.38	2.16	2.10	2.22	2.58	2.47	2.77
D50 [nm]	2.79	2.91	3.04	3.11	3.09	2.99	2.93	2.99	3.24
D80 [nm]	5.02	8.29	5.30	6.69	7.85	6.61	3.73	4.69	5.46
UMN DEG									
D10 [nm]	1.58	1.30	1.40	1.60	1.40	1.35	1.89	1.87	2.16
D50 [nm]	2.27	2.37	2.56	2.24	2.29	1.84	2.39	2.44	2.76
D80 [nm]	5.05	5.88	10.12	5.39	5.17	5.00	3.82	5.04	5.13
3786									
D10 [nm]	1.76	1.49	1.46	2.35	2.22	2.45	2.77	2.93	2.86
D50 [nm]	2.18	1.88	1.77	2.89	2.59	2.95	3.43	3.76	3.53
D80 [nm]	3.04	4.63	3.59	4.66	4.65	4.34	4.83	5.53	5.31
Airmodus A09[a]									
D10 [nm]	1.32	1.10		1.56	1.31				
D50 [nm]	1.61	1.42		1.75	1.69				
D80 [nm]	4.27	4.27		5.00	4.27				
BNL 3025									
D10 [nm]	1.66	1.28		1.73	1.58				
D50 [nm]	2.41	2.16		2.40	2.39				
D80 [nm]	3.84	4.61		5.08	5.15				
BNL DEG									
D10 [nm]	1.47	0.98		1.55	1.40				
D50 [nm]	1.75	1.62		1.85	1.76				
D80 [nm]	2.44	3.17		3.92	3.92				

[a]Airmodus A09 results shown are for a mixing ratio of 0.11.

2.3.2 Influence of working fluid on particle detection

CPCs count particles by condensing supersaturated working fluid vapor onto them, which grows them to a size that can easily be detected by light scattering. Fletcher theory and the Kelvin Equation (Seinfeld and Pandis 2006, Fletcher 1958, Winkler et al. 2008) have been used to describe the relationship between the saturation ratio and the minimum size that can be activated by heterogeneous nucleation. The tendency of a particle to undergo condensational growth is then influenced by the solubility of the particles in the working fluid and the wettability of the particle surface. By simulating over 800 different types of working fluids , Iida and coworkers (2009) concluded that working fluids with low vapor pressure and high surface tension were the best for nanoparticles detection. Results for the TSI 3025 butanol CPC and the UMN DEG are compared in this section. These two CPCs have exactly the same hardware and flow configuration. The surface tensions of DEG and butanol are, respectively, 47.2 dyne/cm and 25 dyne/cm. Their partial vapor pressures at the location where the highest saturation ratio is reached in the instruments are 2.03×10^{-4} and 2.01×10^{-2} respectively for UMN DEG and TSI 3025 (Iida et al. 2009).

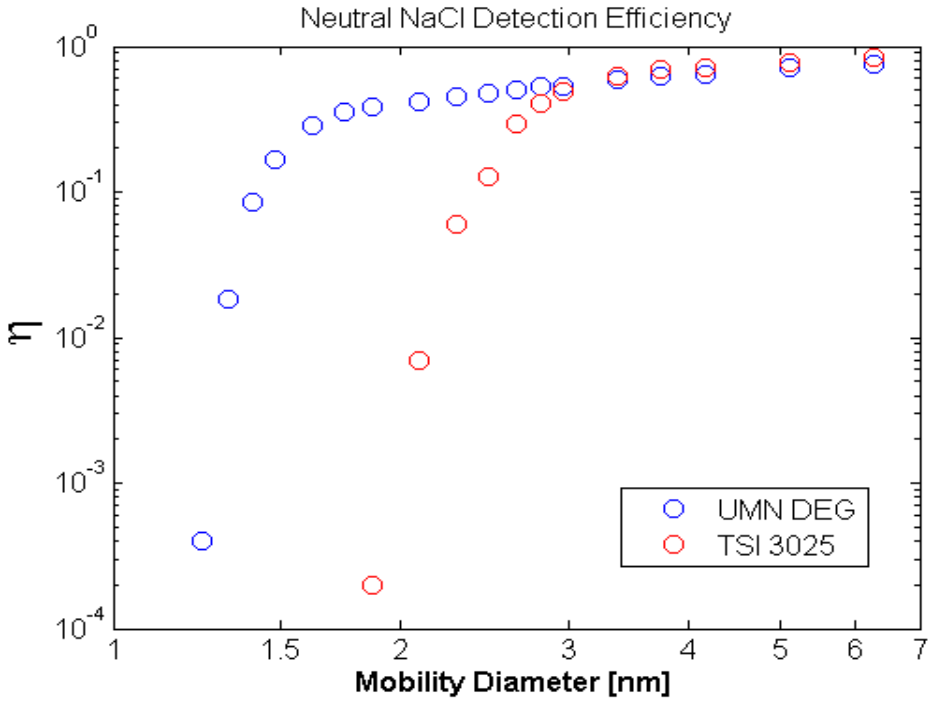

Figure 2.4 Comparison of detection efficiencies for neutral NaCl particles measured with the UMN DEG and TSI 3025.

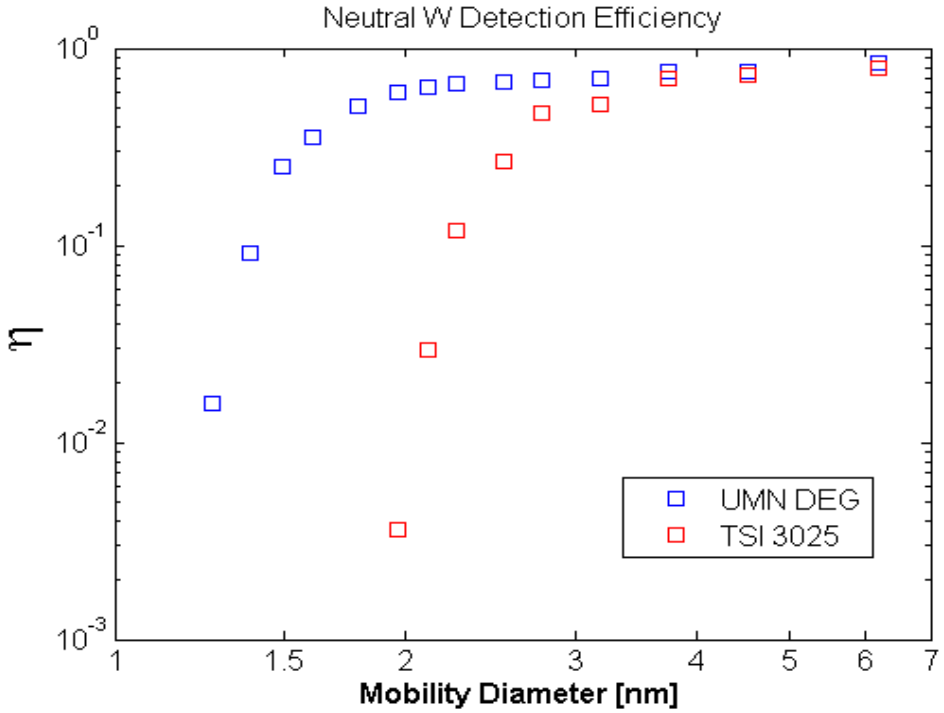

Figure 2.5 Comparison of detection efficiencies for neutral W particles measured with the UMN DEG and TSI 3025.

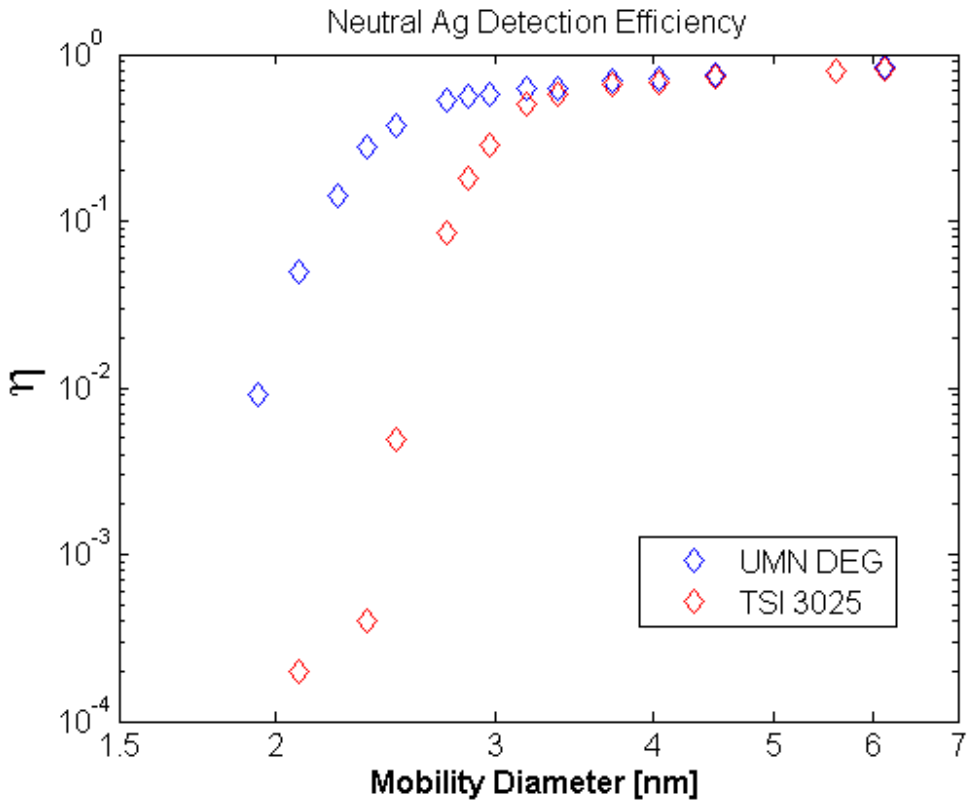

Figure 2.6 Comparison of detection efficiencies for neutral Ag particles measured with the UMN DEG and TSI 3025.

Figures 2.4-2.6 compare the detection efficiencies of the UMN DEG and TSI 3025 CPCs for neutral sodium chloride, tungsten, and silver particles. Detection efficiencies of charged particles for these two instruments are not plotted since they exhibit trends similar to the neutrals and have been published before (Stolzenburg and McMurry 1991, Kesten et al. 1991, Kuang et al. 2012a). Using butanol as the working fluid, the TSI 3025 can hardly detect anything below 2 nm, while the detection efficiencies of neutral sodium chloride and tungsten particles for the UMN DEG are 42% and 59% respectively. With the same hardware design and flow configuration, diffusion losses inside these two instruments are approximately the same. The enhancement of the detection efficiency observed here is solely due to the effect of the working fluid.

2.3.3 Particle composition effects

Besides the effects of the working fluid, particle chemical composition also influences how particles respond to the condensing vapor. In previous work some investigators have used this difference for additional insights into the properties of freshly nucleated particles (Kulmala et al. 2007a, Riipinen et al. 2009). In this section, the TSI 3025, UMN DEG, and TSI 3786 are taken as examples of CPCs that operate with butanol, diethylene glycol, and water as working

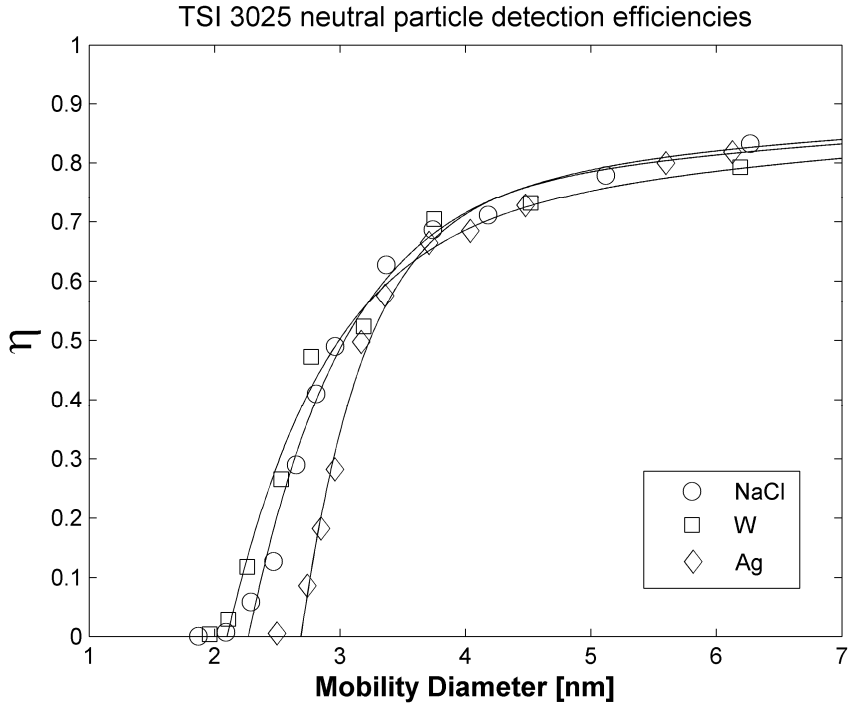

Figure 2.7 TSI 3025 detection efficiency for neutral particles. The lines are the fitting curves according to Eq. (4). Values used for the parameters can be found in table 2.4.

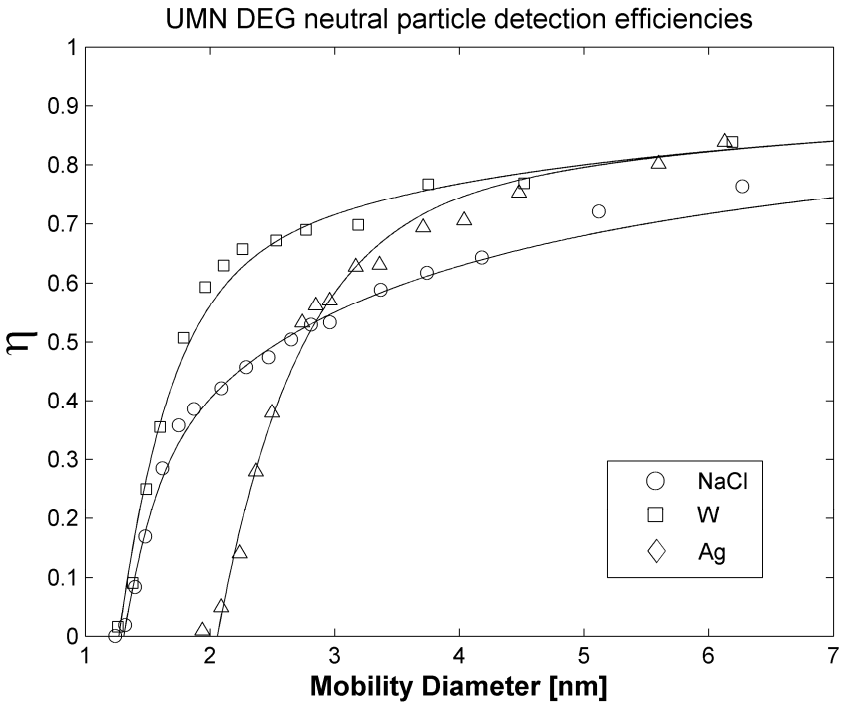

Figure 2.8 UMN DEG detection efficiency for neutral particles. The lines are the fitting curves according to Eq. (4). Values used for the parameters can be found in table 2.4.

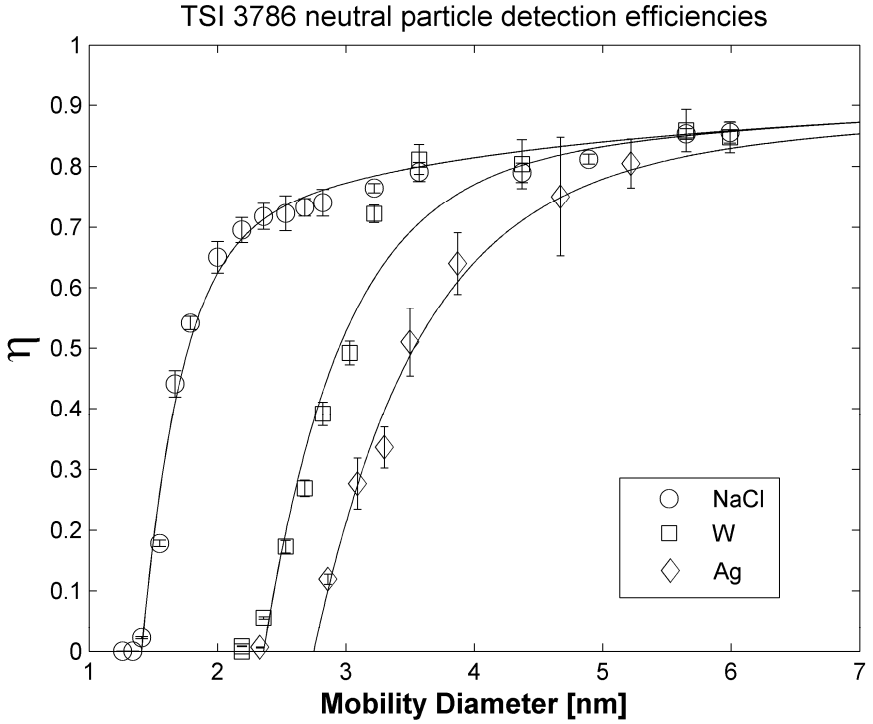

Figure 2.9 TSI 3786 detection efficiency for neutral particles. The lines are the fitting curves according to Eq. (4). Values used for the parameters can be found in table 2.4.

fluids to demonstrate the different responses due to different chemical compositions of neutral particles. Studies of the charged particles for some of these instruments have been individually published before (Iida et al. 2009, Mordas et al. 2008a, Stolzenburg and McMurry 1991). In general, the material dependence of charged particles is similar for these instruments. Data for charged particles obtained during this work are all summarized in table 2.4.

Figures 2.7-2.9 show the detection efficiencies of these three CPCs for neutral sodium chloride, tungsten, and silver particles. For these materials, detection efficiencies of particles larger than 5 nm are relatively insensitive to composition, but differences start to appear for particles smaller than this. For the TSI 3025 butanol CPC, A_0 values (the smallest size that can be activated) for neutral sodium chloride, tungsten and silver are 2.27 nm, 2.10 nm, and 2.68 nm respectively. Tungsten and sodium chloride particles respond similarly to the butanol condensation. Silver particles are slightly more difficult to detect at small sizes. The detection efficiency for 3 nm silver particles is about 30%, while it is about 50% for 3 nm sodium chloride and tungsten particles. Similar to the TSI 3025, the UMN DEG detects tungsten and sodium chloride more effectively than silver. A_0 values for neutral sodium chloride, tungsten and silver are 1.31 nm, 1.27 nm, and 2.06 nm. Neutral sodium chloride particles seem to converge to the diffusion limited detection efficiency slower than silver and tungsten particles. (Notice on Figure 2.8, that the fitting curve agrees nicely with sodium chloride particles smaller than 4.5 nm but not as well for larger particles.) The TSI 3786 water CPC is very sensitive to particle

composition. Water soluble particles are detected most easily, while hydrophobic particles are the most difficult to detect. As shown in Figure 2.9, 50% of neutral sodium chloride particles can be detected at diameters as small as 1.77 nm, with its A_0 value of 1.41 nm. The A_0 value for neutral tungsten particles is 2.36 nm. Almost no hydrophobic silver particles smaller than 3 nm can be detected.

It has been shown that, for homogeneous nucleation without "seed particles", the Kelvin equation can be used to describe particle growth for critical size down to several nanometer (Strey, Wagner and Viisanen 1994). In recent laboratory work, Winkler and coworkers (2008, 2012) showed that, for heterogeneous nucleation, the seed size could even be significantly smaller than the limit provided by the Kelvin equation. The heterogeneous nucleation process was then described as a two-step process (Winkler et al. 2008, Winkler et al. 2011). Firstly, as described by Fletcher theory (Fletcher 1958), the critical size particles were formed from seed particles by the statistical fluctuation of condensation and evaporation of the condensation vapor molecules. When these particles reached the Kelvin limit, they started to stably grow. Compared with the cloud chambers, which are widely used in these nucleation studies, conditions inside CPC are way more complicated. The saturation ratio of the condensing vapor (i.e., working fluid) inside a laminar flow CPC varies with both radial and axial locations. In contrast, saturation ratios in the cloud chamber used by Winkler and coworkers are spatially uniform. Thus, interpreting data from laminar flow instruments is more complicated. The Kelvin limit for laminar flow CPCs such as were used in this study cannot be simply determined.

Nevertheless, results for the water CPC qualitatively agree with the predication of Fletcher theory that the water-silver system has the highest free energy barrier to overcome in forming the embryo. Also, the fact observed in this study that particles around 1 nm can be efficiently detected without triggering self-nucleation inside the CPC also qualitatively supports the two-step heterogeneous nucleation assumption in this size range.

2.3.4 Influence of particle charging state

Classical thermodynamics can estimate the influence of charge on particle detection by calculating the effect of change on the Gibbs free energy of the particle-vapor system (Thomson 1870). Equilibrium between the working fluid liquid layer on the charged particle surface and the working fluid condensing vapor can be established at a lower saturation ratio than would occur for a neutral particle. This effect will be stronger when particle size becomes smaller (Thomson 1906). This implies that very small (<3 nm) charged particles should be much easier to detect than neutral ones.

Charge-enhanced condensation was observed for most results in this study. Figures 2.10-2.11 compare the detection efficiencies for negative and neutral sodium chloride particles for the TSI 3025, UMN DEG, and TSI 3786 respectively. For the TSI 3025 and UMN DEG, the

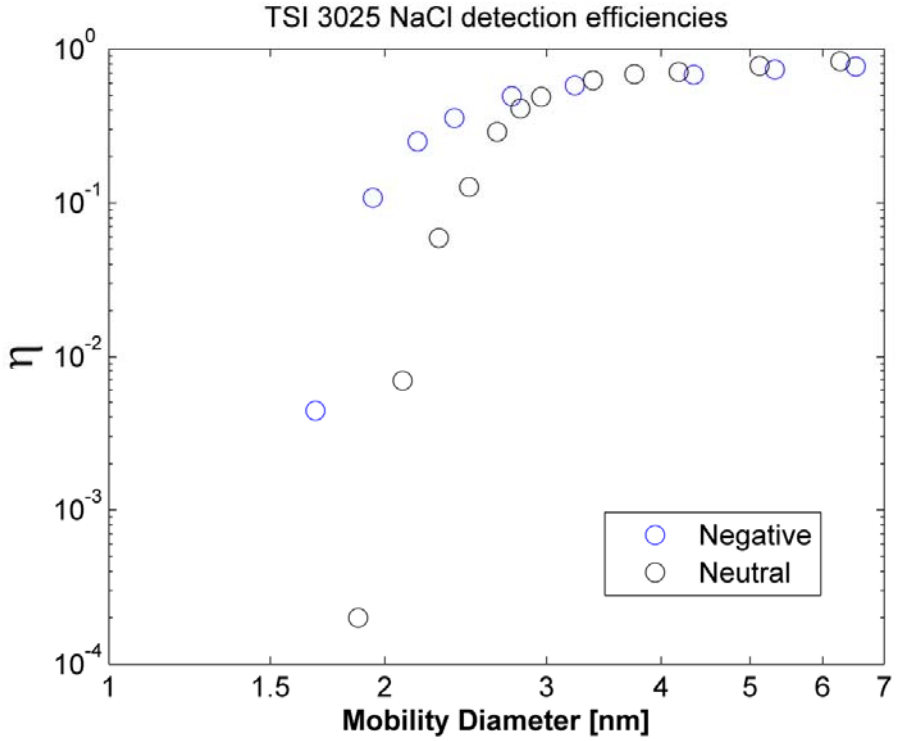

Figure 2.10. TSI 3025 detection efficiency for sodium chloride particles.

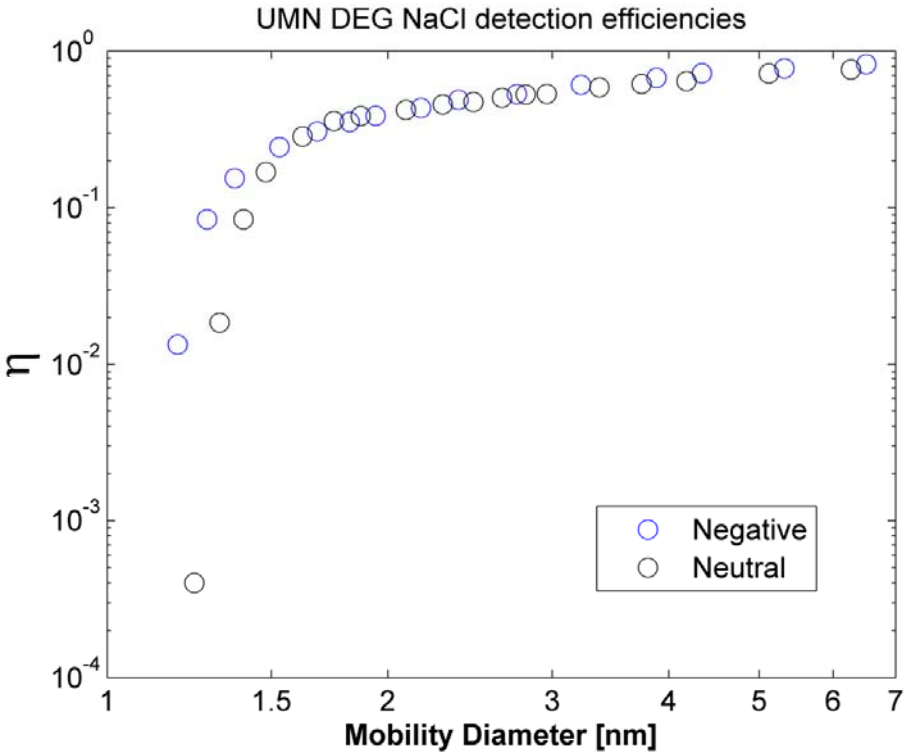

Figure 2.11. UMN DEG detection efficiency for sodium chloride particles.

difference was quite significant. For the TSI 3025, negative and neutral sodium chloride particles larger than 3 nm are detected at approximately the same efficiency. As predicted by the theory, the difference becomes larger when particle size decreases. At 2 nm, detection efficiencies of negative particles are more than 10 times higher than detection efficiencies of neutral particles. For the UMN DEG, differences in detection efficiency started to appear at about 1.5 nm. As shown in Figure 2.12, the effect of particle charge is not significant for the TSI 3786 water CPC with sodium chloride particles. This may be because both neutral and charged particles undergo deliquescence, which may be more important than charge state in determining activation.

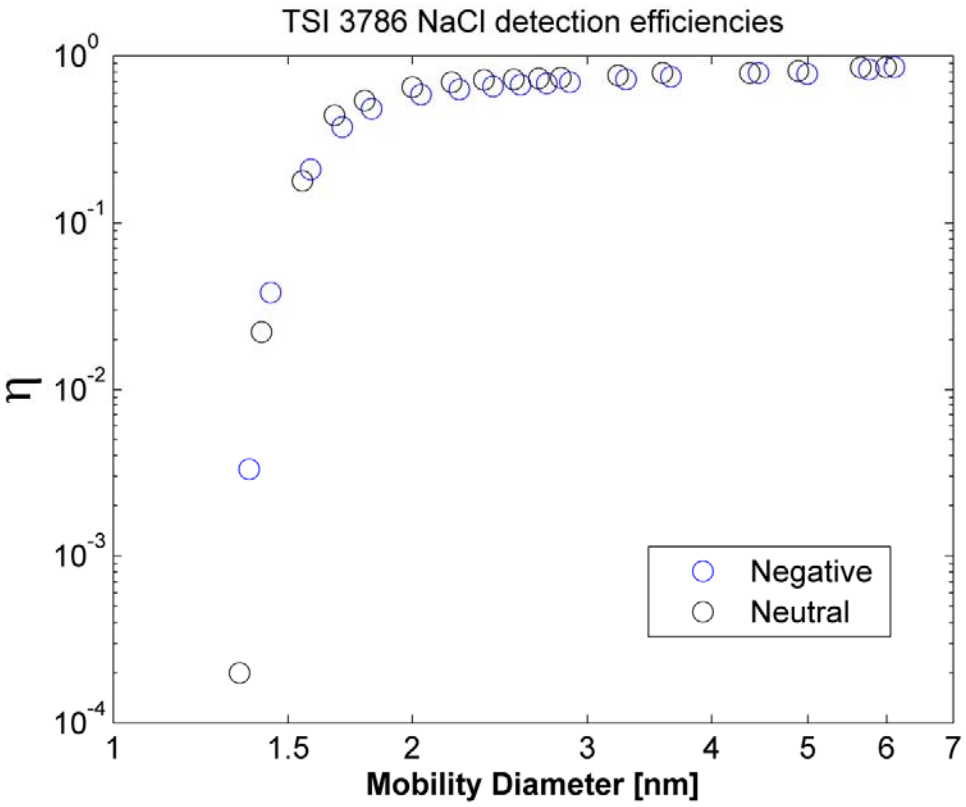

Figure 2.12 TSI 3786 detection efficiency for neutral and negatively charged sodium chloride particles.

Thompson theory does not differentiate between positive and negative ions, meaning the same detection efficiency should be expected with either positive or negative charged particles. However, sign preferences (either positive or negative particles are more likely to be activated) were observed in previous studies (Winkler et al. 2008, Iida et al. 2009, Sipila et al. 2009, Vanhanen et al. 2011). In this study, detection efficiencies for negatively charged particles are always higher than positively charged ones below 2 nm. Examples are shown in Figures 2.13 and 2.14 for the Airmodus A09 with sodium chloride and tungsten particles.

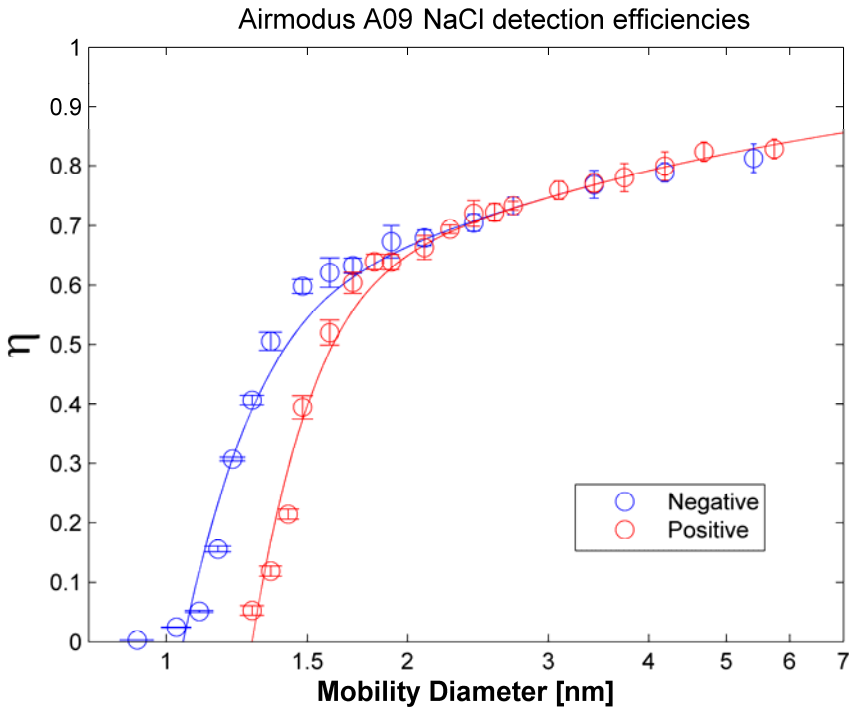

Figure 2.13. Airmodus A09 detection efficiency for sodium chloride particles.

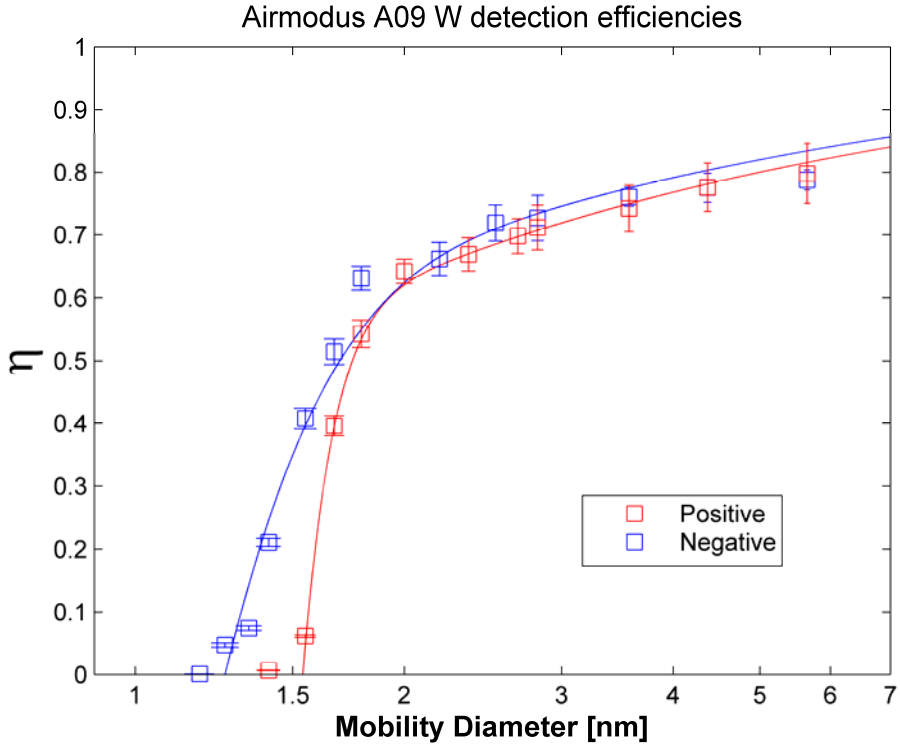

Figure 2.14 Airmodus A09 detection efficiency for tungsten particles.

2.3.5 Impact of CPC operation conditions

Higher saturation ratios in the activation and growing section of the CPC lead to higher detection efficiencies. However, if the saturation ratio is too high, particles formed by self-nucleation of the working fluid can interfere with measurements. Most CPCs are operated at sufficiently low saturation ratios to avoid self-nucleation. Exceptions are some pulse-height instruments (Sipila et al. 2009, Mordas, Sipila and Kulmala 2008b), which separate counts produced by self-nucleation from those produced by sampled particles. Counts from nucleated and sampled particles are differentiated by measuring the pulse height of the scattered light, which is a measure of droplet size. Sampled particles grow to a larger ultimate size than nucleated particles, and therefore produce larger pulses. By increasing the saturator and condenser flow rates, Kuang showed that the TSI 3025 and UMN DEG laminar flow CPCs can be operated at a higher saturation ratio (by increasing the saturator temperature) without self-nucleation (Kuang et al. 2012a). Thus, higher detection efficiencies can be achieved. The modified CPCs are called BNL 3025 and BNL DEG. These two instruments are calibrated in this work with the same setup. Detection efficiencies for negatively charged sodium chloride particles are compared for the TSI 3025 and BNL 3025 in Figure 2.15, and for the UMN DEG and BNL DEG in Figure 2.16. A detailed description of the modifications and their effects on saturation profiles can be found in Kuang et al. 2012.

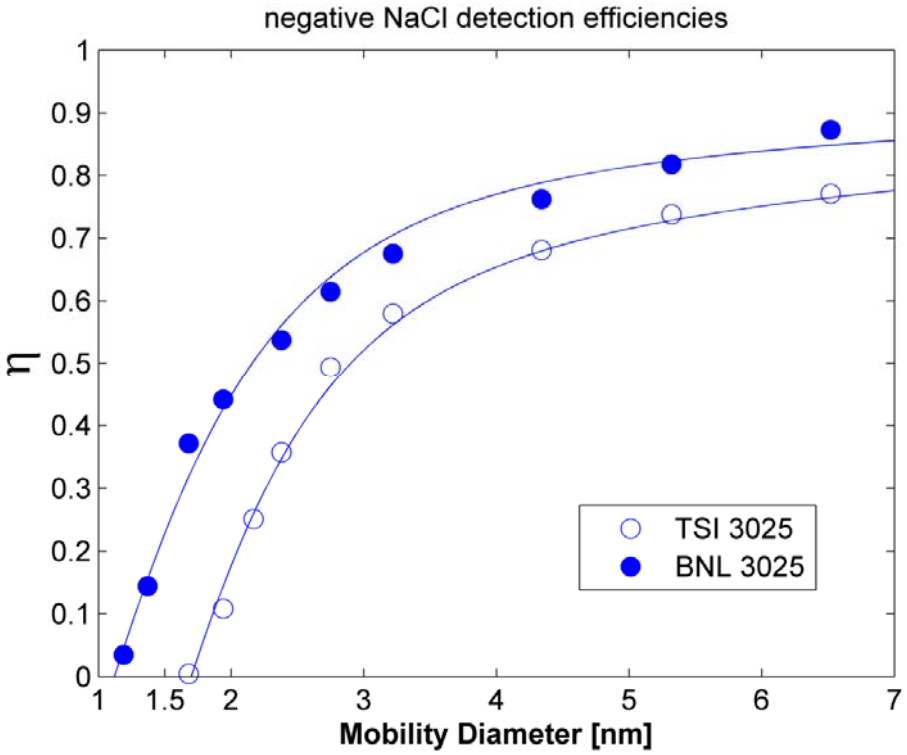

Figure 2.15 Comparison between TSI 3025 and BNL 3025.

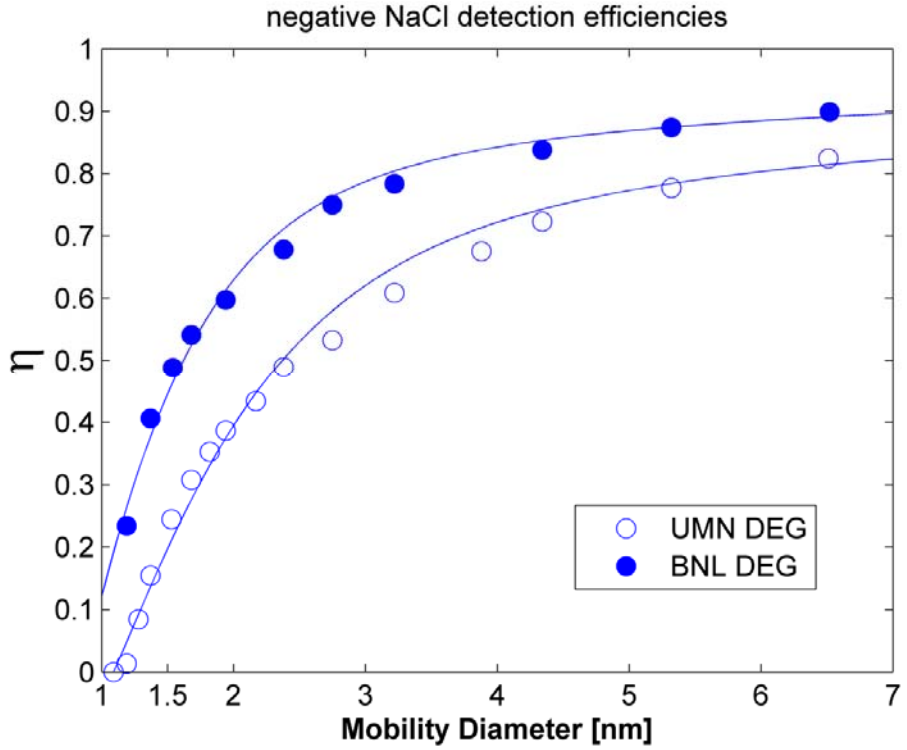

Figure 2.16 Comparison between UMN DEG and BNL DEG.

2.4 Summary

Detection efficiencies for mobility-classified sodium chloride, silver and tungsten particles, and detection efficiencies of molecular ions and ions produced by ionizing radiation in air are evaluated for six different CPCs in the size range from 1 nm to 7 nm. Fitting results for these CPCs are provided for reference. Evaluating all the instruments with the same setup, we showed that charge states and particle composition can both influence CPC performance, and that this influence can be significant below 3 nm. In most applications, the composition of sampled particles is not known. Because detection efficiencies depend on particle composition, this inevitably introduces measurement uncertainties. This study shows that although CPCs for detecting 1 nm particles have been developed recently, uncertainties remain about how to accurately measure the concentration of such particles if their composition is unknown.

Chapter 3: Time and Size Resolved Growth Rates for 1-5 nm Freshly Nucleated Particles in Atlanta*

3.1 Introduction

Atmospheric nucleation has been found to be closely related to the formation of cloud condensation nuclei (Spracklen et al. 2008b, Adams and Seinfeld 2003, Zhang et al. 2010b), and therefore can lead to large uncertainties in global climate modeling (IPCC 2007). Atmospheric measurements have been carried out all over the world during the last few decades (Kulmala et al. 2004c). Observed fast nucleation rates during these measurements, however, cannot be explained by classical theories (Doyle 1961, Nair and Vohra 1975). On the other hand, the rapid growth rates (GR) of freshly nucleated atmospheric particles, often up to ten times (or more) the rate that can be explained by sulfuric acid condensation alone (Weber et al. 1997), have never been well understood either. Defining the growth enhancement factor Γ as the ratio of the actual GR to contribution of sulfuric acid condensation to growth rates (GR_{SA}), previous researches

* Aspects of the results described in this chapter (including some text and figures) have been published in Jiang et al. (2011b), Jiang et al (2011c) and Kuang et al. (2012b).

showed that the average values of Γ were around 5~10 and can be as high as 20~50 (Sihto et al. 2006, Riipinen et al. 2007, Iida et al. 2008, Stolzenburg et al. 2005, Nieminen et al. 2009). These high values of Γ are likely due to organic compounds, which could account for up to 95% percent of the growth (O'Dowd et al. 2002a, Smith et al. 2008, Makela et al. 2001, Riipinen et al. 2012). Limited by instrumentation, most GRs obtained previously are for particles larger than 3 nm. Also, currently-available instrumentation can measure the composition of particles down to 10 nm, but not smaller than that. Therefore, there is presently no method available for explicitly identifying the compounds that lead to the high Γ values for sub 10 nm particles.

Efforts to develop CPCs for even smaller particles, first 3 nm (Stolzenburg and McMurry 1991), then sub 3 nm (Hering et al. 2005, Gamero-Castano and de la Mora 2000, Kim et al. 2003), and more recently 1 nm (Iida et al, 2009), were motivated by the desire to gain a more fundamental understanding of the earliest steps in particle formation and growth. Based on Iida's work, several different types of CPCs using DEG as the working fluid have been developed for 1 nm particle detection (Vanhanen et al. 2011, Jiang et al. 2011b, Kuang et al. 2012a). By careful inter-comparison between a newly developed 1 nm CPC and a traditional 3 nm CPC, Sipila and coworkers (Sipila et al. 2010) showed that the ability to detect freshly nucleated particles in the 1 nm range adds significantly to what can be learned about mechanisms of nucleation and growth.

In this work, the application of a diethylene glycol CPC, first developed by Iida and coworkers (Iida et al. 2009), in the scanning mobility particle spectrometer (SMPS) for 1 nm particle detection in the atmosphere is described. We refer to this instrument system as the DEG SMPS. Field measurements with the DEG SMPS were carried out during the 2009 Nucleation and Cloud Condensation Nuclei (NCCN) campaign at the Jefferson St. site in Atlanta, Georgia (Solomon et al. 2003). Atmospheric particle size distributions from 5 nm down to about 1 nm were obtained. Using the complete particle size distribution, a new method of calculating GRs of freshly nucleated particles was developed. While previously GR was estimated by averaging over particle size and time (Hirsikko et al. 2005, Stolzenburg et al. 2005, Manninen et al. 2009, Yli-Juuti et al. 2011), the new method described in this chapter for the first time decouples the time and size dependence of GR. GR of freshly nucleated particles represents all the gas-to-particle conversion processes that contribute to growth, thus contains important information about nucleation. De-coupling the time and size effects on particle growth allows new insights into chemical processes that contribute to growth.

3.2 Field measurements and observations

3.2.1 DEG SMPS

Figure 3.1 illustrates a schematic diagram of the DEG SMPS used in NCCN campaign. Atmospheric aerosol was sampled at 20 lpm including a transport flow of 13 lpm to reduce the inlet losses. The sampling flow of 7 lpm was extracted along the axis to reduce diffusion losses, which have a greater effect near the walls for laminar flow. Large particles were removed by an impactor with 10 μm cutoff size to prevent their accumulation inside the system. Sampled particles then entered an aerosol charger based on the design of Chen and Pui (Chen 1999). The sheath air used in the original design was eliminated to maximize concentrations of charged particles. Instead, a higher sampling flow rate (7 lpm) was used to reduce particle losses inside the charger. The diameter of the cylindrical charger housing was increased from 3.8 to 6.0 cm and the ion production region was redesigned to securely hold six 0.5 mCi Po-210 radioactive ionizers (NRD LLC, Model 1U400). The larger housing and higher radioactivity compensate for the higher flow rate that we used. This charger can be used as either a unipolar or bipolar charger by turning on and off the voltage applied to the ion production region. Due to the large uncertainty in the charging fraction and electrostatic loss of particles when operated in the unipolar charging mode, only results obtained in the bipolar charging mode are discussed in this chapter. After the charger, sampled particles were classified using a TSI 3085 nano differential mobility analyzer (nanoDMA) (Chen et al. 1998). A bypass flow of 5 lpm was used to reduce particle losses at the nanoDMA inlet. The nanoDMA was operated in a closed-loop for sheath and excess flows (15 lpm). The aerosol inlet flow rate was equal to the aerosol outlet flow rate (2 lpm). Negatively

charged particles were selected in the nanoDMA by applying positive voltage to the central electrode.

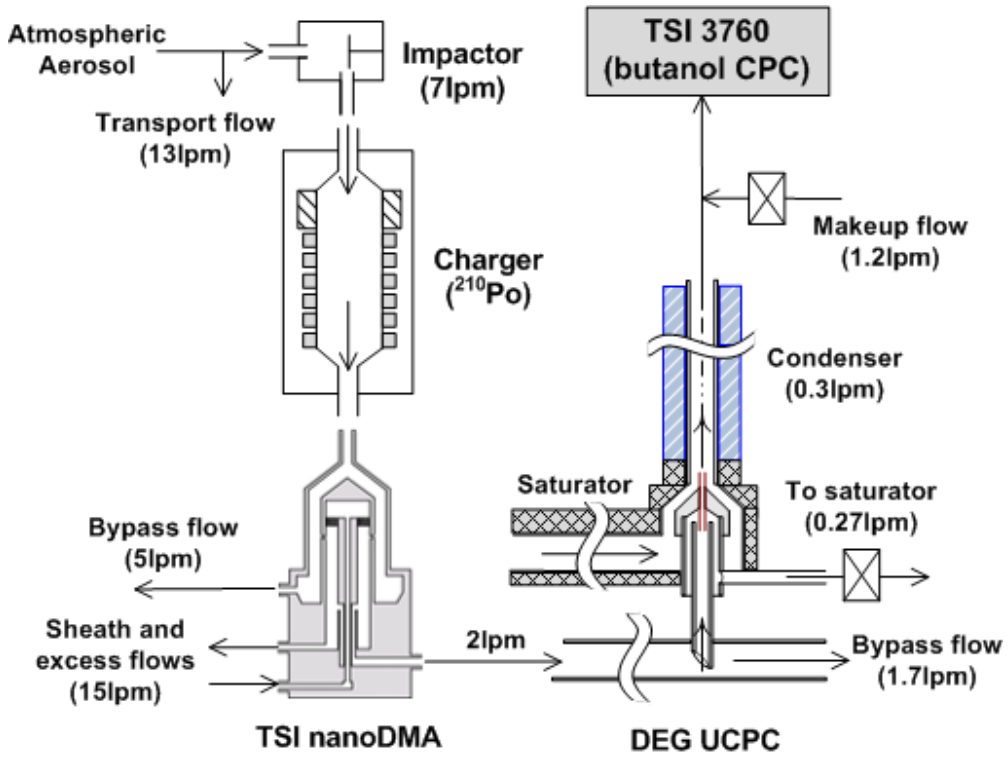

Figure 3.1 Schematic of the scanning mobility particle spectrometer system using the DEG CPC and a booster butanol CPC (the DEG SMPS).

Classified particles were then sent into the detector consisting of the DEG CPC and a TSI 3760 butanol CPC. The designs of the saturator/condenser for the DEG CPC are the same as those used in the TSI 3025 CPC (Stolzenburg and McMurry 1991), as is the flow control scheme with bypass, capillary, and condenser flow rates of 1.7, 0.03, and 0.3 lpm, respectively. The capillary flow rate was calibrated using the procedure given by Stolzenburg (Stolzenburg 1988). The saturator and condenser temperatures are monitored

using thermocouples. The DEG CPC was used to grow particles by heterogeneous condensation of DEG. The saturation vapor pressure of DEG within the CPC condenser is about a factor of 100 lower than that of butanol. Consequently, the final droplet sizes after the DEG CPC are correspondingly smaller than those achieved using a butanol CPC and cannot be efficiently detected using light scattering. Therefore, the laser detection unit was removed, and a conventional TSI 3760 butanol CPC with a 50% cutoff size at 15 nm, was used as a "booster" after the DEG CPC to further grow particles and to detect them individually using light scattering (Iida et al. 2009).

3.2.2 DEG Data inversion

Procedures for inverting DEG SMPS data to obtain number size distributions are similar to those used for other types of SMPS systems. Multiple charging effects are negligible for the particle size range measured by the DEG SMPS, i.e. 1–10 nm. The method proposed by Knutson (Knutson 1976) and refined by Stolzenburg and McMurry (Stolzenburg and McMurry 2008) was used for inverting the DEG SMPS data. Nearly identical results were obtained when a more complex linear inversion method was used (Hagen and Alofs 1983).

Similar to Equation (27) in Stolzenburg and McMurry's work, the unknown size distribution function is given by

$$(1)\quad \left.\frac{dN}{d\ln D_p}\right|_{D_p*} = \frac{N \cdot a*}{\frac{Q_a}{Q_s}\cdot\beta\cdot(1+\delta)\cdot f_c(D_p*)\cdot\eta_{cpc}(D_p*)\cdot\eta_{pene}(D_p*)}$$

where N is the measured aerosol concentration downstream of the DEG CPC; D_p is the particle diameter; D_p* is the diameter of a particle with electrical mobility equal to nanoDMA transfer function centroid electrical mobility; Z_p is the particle electrical mobility; $a*$ has a value between 1 to 2, given by

$$(2)\quad a* = (-d\ln Z_p / d\ln D_p)\Big|_{D_p*}$$

β and δ are given by

$$(3)\quad \beta = (Q_s + Q_a)/(Q_m + Q_c)$$

$$(4)\quad \delta = (Q_s - Q_a)/(Q_s + Q_a)$$

Q_a is the aerosol inlet flow rate; Q_s is the aerosol outlet flow rate; Q_c is the nanoDMA sheath flow rate; Q_m is the nanoDMA excess flow rate; $f_c(D_p^*)$ is the fraction of charged particles; $\eta_{cpc}(D_p^*)$ is the CPC activation efficiency of particles with a diameter of D_p^*; and $\eta_{pene}(D_p^*)$ is the product of particle penetration efficiencies through the sampling lines, the nanoDMA, and the DEG CPC.

DEG CPC activation efficiencies were evaluated experimentally as described in Chapter 2. CPC performance was evaluated at different saturator and condenser temperatures. Since in the SMPS system, the DEG CPC was operated downstream of the charger, it must be operated so as to avoid detection of air ions. Figure 3.2 shows the DEG CPC activation efficiencies for positively charged tetra-heptyl ammonium ions (1.47 nm

mobility diameter). The activation efficiency for $N^+[C_7H_{15}]_4$ increased from ～0.5% to ～33.6% as the saturator-condenser temperature difference increased from 39.3 ℃ to 45.8 ℃. The temperature difference between the saturator and the condenser determines the vapor saturation ratio inside the condenser and therefore affects the activation efficiency. Larger temperature differences lead to higher saturation ratios and higher activation efficiencies. The self-nucleation rate of the working fluid also increases with increasing saturation ratio. When the self-nucleation rate is too high, "background particles" occur in the CPC. As shown in Figure 3.2, the concentration of self-nucleated particles increases significantly when the temperature difference exceeds ~44.5 ℃. To avoid the potential interference between homogeneously nucleated particles and sampled particles, we prefer to operate CPCs under conditions without self-nucleation of the working fluid, e.g., one background count per five minutes (～0.007 particles/cm^3) is the criterion used in previous studies by our laboratory (Stolzenburg and McMurry 1991, Iida et al. 2009). To stretch the capability of CPCs in detecting sub-2 nm particles, however, some studies have operated them with homogenous nucleation occurring inside the condenser (Sipila et al. 2009, Mordas et al. 2008b). While some success was achieved in measuring well controlled laboratory aerosol systems, caution should be taken when measuring unknown aerosols (e.g., atmospheric aerosol). In this study, we used the same criterion, i.e., the background concentration is less than ~0.007 particles/cm^3, and operated the DEG CPC at conditions without self-nucleation of the working fluid. A temperature difference of 39 ℃ was used. Also, when analyzing data we assumed that the activation efficiencies of freshly nucleated atmospheric particles were the same as for

sodium chloride particles. This assumption, which is a possible source of systematic error, was made since we have not yet devised a method to calibrate the DEG CPC with freshly nucleated atmospheric particles. The activation efficiency curve for negatively charged NaCl particles used in analyzing the NCCN data is shown in Figure 3.3.

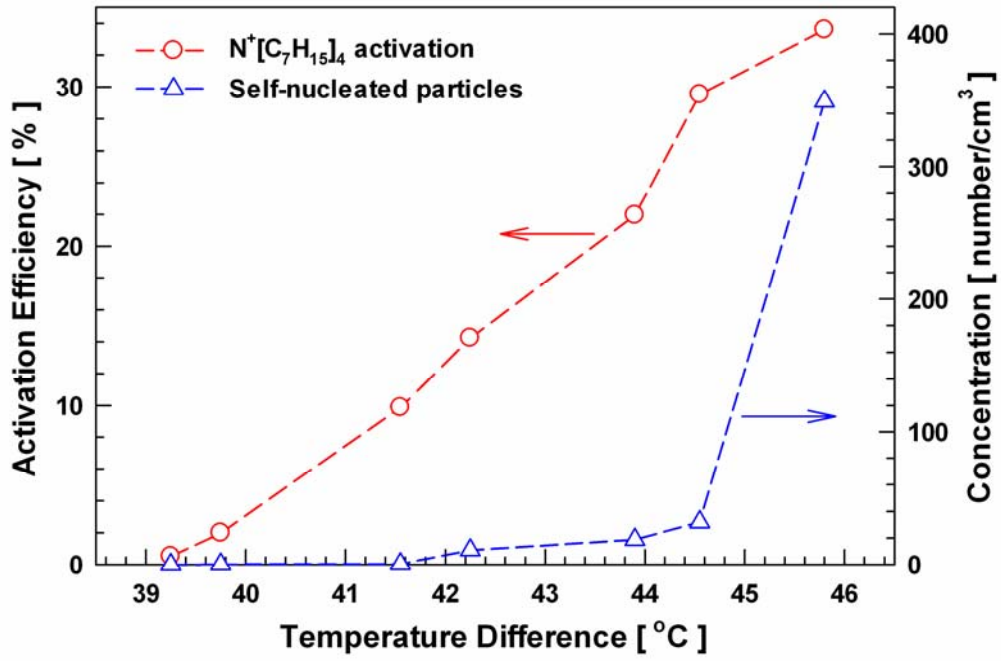

Figure 3.2 DEG CPC activation efficiencies of positively charged 1.47 nm tetraheptyl ammonium ions and the number concentrations of the self-nucleated particles as a function of the saturator-condenser temperature difference. When estimating activation efficiencies, the contribution of self-nucleated particles is excluded. The temperature difference of 39 ℃ is used during this study.

Figure 3.4 shows the size-dependent penetration efficiencies, bipolar charging efficiencies, and the nanoDMA transfer function with a fixed voltage for 1.47 nm particles. The transport efficiencies in the sampling lines were evaluated theoretically by

assuming all the losses are due to laminar flow diffusion losses. It was assumed that bipolar charging rates given by Fuchs' stationary-state theory (Fuchs 1963) can be extrapolated down to 1 nm. The TSI 3085 nanoDMA transfer functions and penetrations for sub-2 nm particles were estimated based on Jiang's work (Jiang et al. 2011a). Measured nanoDMA transfer functions agree very well with the diffusive transfer function theory (Stolzenburg 1988). The DMA inlet and outlet losses were also calculated using the laminar diffusional deposition model for cylindrical tubes (Reineking 1986). The effective lengths used for the inlet and outlet regions are 2.24 and 1.40 m, respectively. CPC penetration efficiencies are determined by diffusional losses to the walls of the inner inlet tube and the capillary.

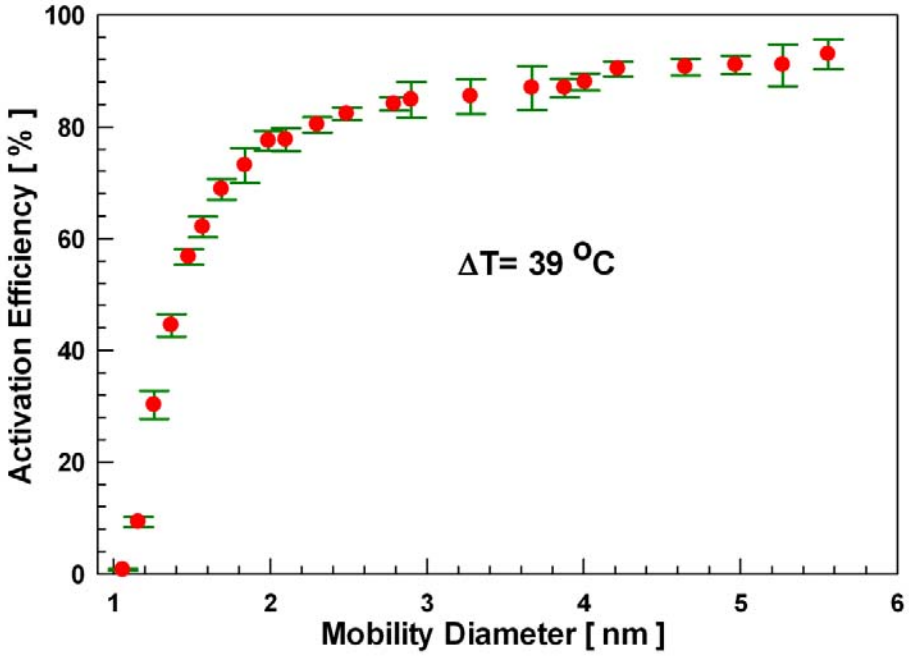

Figure 3.3 DEG CPC activation efficiencies of 1 to 6 nm sodium chloride particles carrying a single negative charge.

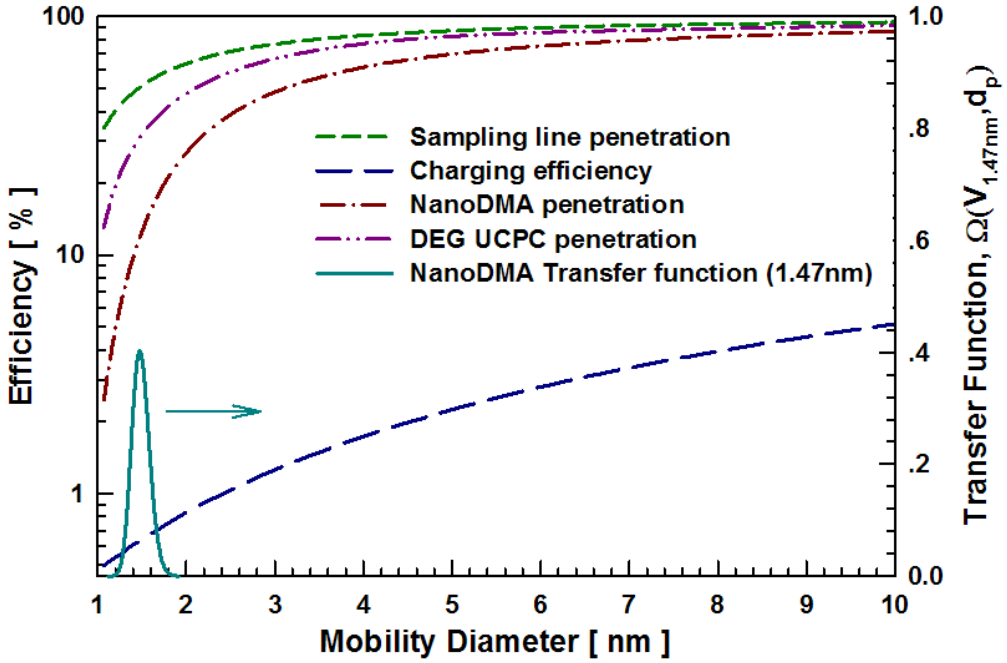

Figure 3.4 Size-dependent particle transport efficiencies in the sampling lines, bipolar charging efficiencies (fractions of negatively charged particles carrying a single charge), nanoDMA penetration efficiencies, DEG CPC penetration efficiencies, and the transfer function of the nanoDMA with a fixed DMA voltage for 1.47 nm particles.

3.2.3 Cluster CIMS measurement

The Cluster CIMS (50-900 amu) was used during the NCCN field campaign to measure the concentrations of electrically neutral sulfuric acid vapor and clusters that contained from two to four sulfuric acid molecules (monomer, dimer, trimer, and tetramer). A detailed description of this instrument and the data inversion process has been discussed

by Zhao and co-workers (Zhao et al. 2010, Chen et al. 2012). In order to convert the sulfuric acid cluster concentrations into number distributions, we assume that their density equals the bulk density (1.84 g/cm^3) of sulfuric acid, although the results shown are not very sensitive to this value. Eq. (5) is used to calculate the size distribution of sulfuric acid clusters containing k sulfuric molecules:

(5)

$$\left.\frac{dN}{d\log D_{p\,geometric}}\right|_k = \frac{N_k}{\Delta\log D_{p\,geometric}} = \frac{N_k}{\log\left(\frac{6(k+1/2)m_{H_2SO_4}}{\pi\rho}\right)^{1/3} - \log\left(\frac{6(k-1/2)m_{H_2SO_4}}{\pi\rho}\right)^{1/3}}$$

where N_k is the number concentration of cluster k, ρ is the cluster density, $m_{H_2SO_4}$ is the mass of the sulfuric acid monomer, and $D_{p\,geometric}$ is the geometric diameter of the geometric diameter. The relation between geometric diameter and mobility diameter (Equation 6) has been discussed previously (Tammet 1995, Ku and de la Mora 2009, Larriba et al. 2011).

(6) $D_{p,geometric} = D_{p,mass} = D_{p,mobility} - 0.3nm$

3.2.4 Nucleation events during NCCN

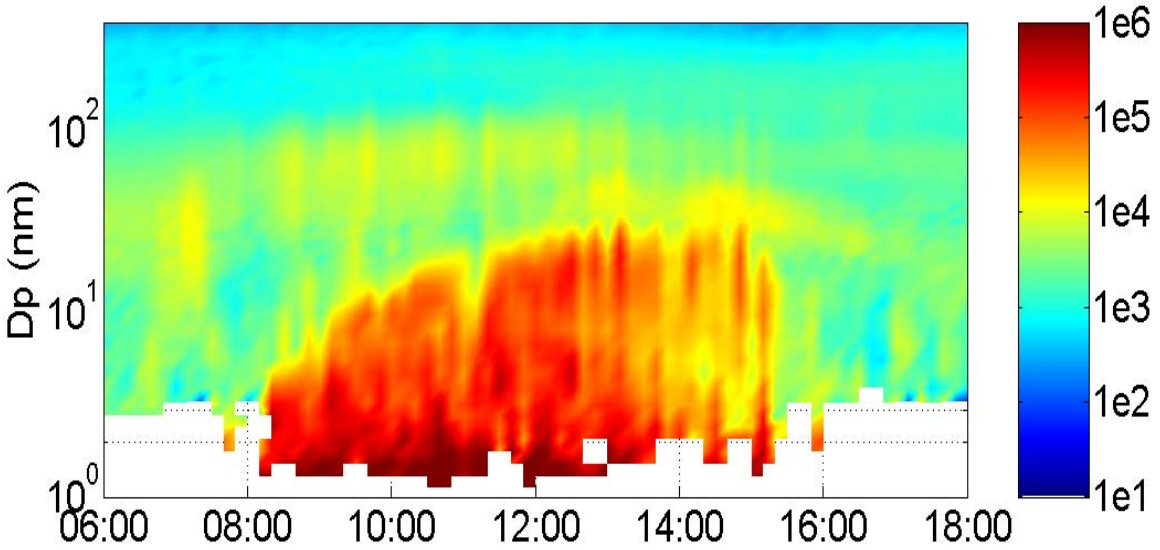

Figure 3.5 Composite contour plot of particle number size distributions measured by the PSD (top, 9–200 nm) and by the DEG SMPS (bottom, 1–9 nm) during atmospheric nucleation events on Aug 23, 2009. The color indicates the values of the size distribution function ($dN/dlog_{10}(D_p)$, number/cm^3).

Figure 3.5 shows a composite contour plot of particle number distribution data ($dN/dlog_{10}D_p$, number/cm^3) from the DEG SMPS and the PSD obtained during a typical nucleation event in Atlanta on August 23, 2009. SO_2 concentrations of up to 30 ppbv were observed on this day. Freshly nucleated particles down to 1 nm were measured by the DEG SMPS. As shown in Figure 3.5, very few sub-2 nm particles were detected before and after the nucleation event, while the concentrations of 1–2 nm particles increased dramatically during the event.

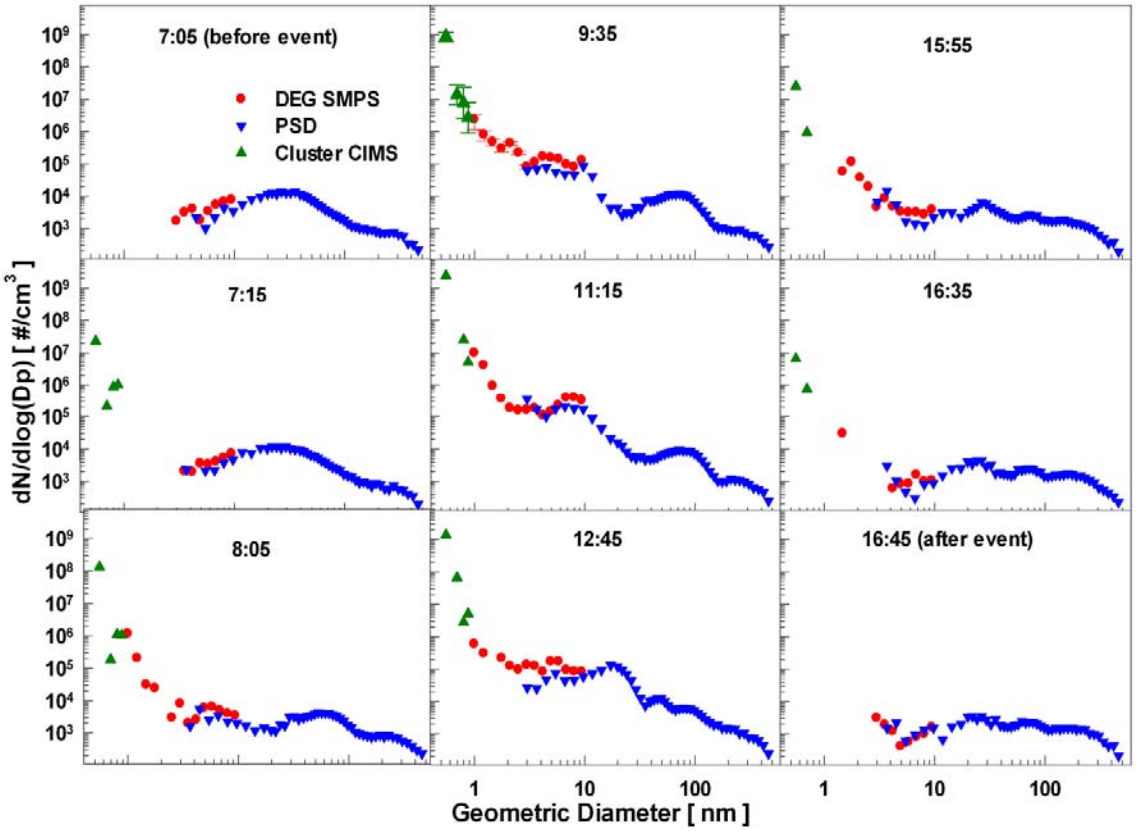

Figure 3.6 Aerosol size distribution measured with three instrument systems during nucleation events in Atlanta, GA on August 23, 2009. The estimated uncertainties shown for 9:35 on August 23 apply to all data. Times shown are local standard time.

Figure 3.6 shows nine number distributions measured during nucleation on August 23. Sulfuric acid vapor and clusters were first detected at 7:15. By 8:05, the DEG SMPS also detected particles down to ~1 nm. Particles from 3 nm to 500 nm were measured by a traditional particle size distribution spectrometer (PSD), which consists a regular SMPS and a nano SMPS (Woo et al. 2001). Sulfuric acid monomer, dimer, trimer, tetramer, and nanoparticles down to 1 nm were detected by both instruments throughout the nucleation

event. The smallest particles that were detected by the DEG SMPS are comparable in size to the sulfuric acid trimer and tetramer detected by the Cluster CIMS, and the distribution functions measured by the Cluster CIMS and DEG SMPS tend to follow a similar trend with size. At ~1 nm, values of the distribution functions measured by these instruments typically agree to within the estimated measurement uncertainty. The DEG SMPS and the PSD also agree well in the overlapping 3 to 10 nm range. Error bars are shown for the Cluster CIMS and DEG SMPS data measured at 9:35 on August 23. Estimated relative uncertainties for $[H_2SO_4]$, $[H_2SO_4]_2$, $[H_2SO_4]_3$, and $[H_2SO_4]_4$ are factors of ~1.3, 2, 3, and 3, respectively. Relative standard deviations of DEG SMPS data are ~10% at 3 nm and ~50% at 1 nm.

It is not obvious that the Cluster CIMS data should agree so well with the DEG SMPS data. As was discussed by Zhao et al. (2010), mass spectra measured with the Cluster CIMS include signals from many unknown high molecular weight species that are not associated with nucleation. Also, the activation efficiencies of the DEG CPC depend on composition. The fact that Cluster CIMS number distributions for identified clusters are comparable to number distributions measured by the DEG SMPS suggests that particles that undergo condensational growth in the atmosphere also undergo condensational growth in the DEG CPC and that, when interpreting Cluster CIMS data, signals produced by non-cluster species were successfully subtracted.

3.3 Steady state growth rate

Most of the nucleation events during the NCCN campaign were associated with solar radiation and sulfur dioxide (SO_2) emissions from the McDonough Steam Generating Plant, located 4.65 miles northwest from the sampling site. Depending on the wind speed and direction, the estimated transport time from the source was between 50 min to 2 hours. This type of nucleation event is also referred to as a “plume” event (Kulmala et al. 2004c, Sakurai et al. 2005). High concentrations of nanoparticles were formed photochemically and detected when the air mass was transported to the sampling site. For this type of event, instead of seeing an increase of particle number concentration at small sizes and their subsequent slow growth as appears in a “regional” event (Makela et al. 2000), very high concentrations of particles will be observed for all the size bins over a large size range (see Figure 3.5).

Previously established methods of estimating GR either by estimating the time delay between the increase of sulfuric acid concentration and the appearance of 3 nm particles (Weber et al. 1997, Nieminen et al. 2009), or by tracking the increase of the particle mode (Stolzenburg et al. 2005, Hirsikko et al. 2005), are thus not applicable to plume events, since for measurement carried out at a fixed sampling site under more-or-less constant atmospheric conditions, no time delay or modal growth can be identified. In other words, plume samples consist of a "snapshot" in time of the aerosol distribution function as it is nucleating and growing. A new method is introduced in this section for

analyzing GR of small particles during these plume events. This analysis method utilizes the novel result that size distributions (<5 nm) for a nucleating system in the presence of an aerosol achieve pseudo steady-state shortly after the start of nucleation.

For an aerosol system that is growing through simultaneous gas uptake and coagulation, the aerosol population balance equation (Gelbard and Seinfeld 1978) can be used to describe the evolution of the number concentration between particle diameters D_{pi} and D_{pi+1}.

$$(7)\quad \left.\frac{\partial N}{\partial t}\right|_{i,i+1} = \left.\left(\frac{\partial N}{\partial t}\right)_{growth}\right|_{i,i+1} + \left.\left(\frac{\partial N}{\partial t}\right)_{coag}\right|_{i,i+1}$$

This equation states that the change of concentration of particles between diameter i and and i+1 equals the change due to two mechanisms of growth and coagulation. Assuming pseudo steady-state, the particle population balance equation (Eq. 7) can thus be simplified to,

$$(8)\quad 0 = \left.\left(\frac{\partial N}{\partial t}\right)_{growth}\right|_{i,i+1} + \left.\left(\frac{\partial N}{\partial t}\right)_{coag}\right|_{i,i+1} = GR\left.\frac{\partial N}{\partial D_p}\right|_{i,i+1} + \left.\left(\frac{\partial N}{\partial t}\right)_{coag}\right|_{i,i+1}$$

The first term on the RHS of Eq. (8) can be estimated as the nucleation flux in and out of the diameter bin between D_{pi} and D_{pi+1}. Nucleation flux equals the product of the particle size distribution and GR. With the complete particle size distribution obtained during NCCN, the second term on the RHS of Eq. (8) can also be estimated accurately. The only unknown parameters are GR in Eq. (8), and thus can be solved. A detailed description of the mathematics can be found in the appendix of this chapter.

Size and time-dependent particle growth rates due solely to the condensation of sulfuric acid, GR_{SA}, were calculated using measured sulfuric acid concentrations and assuming bulk properties for the sulfuric acid vapor (density = 1.84 g*cm^{-3}), explicitly accounting for the dimension and motion of collision partners during condensation (Lehtinen and Kulmala 2003); the effects of interaction potentials were neglected. The size-dependent growth rate enhancement Γ (defined as the ratio of GR to GR_{SA}) was then obtained, quantifying the size-dependent contribution of species other than sulfuric acid to the observed growth. In this study, size-dependent particle growth rates GR and growth rate enhancements Γ down to 1 nm geometric diameter will be presented for an event measured during NCCN (7 August 2009).

3.3.1 Size dependent growth rate

Observed size-dependent growth rates, $GR(D_p)$, down to 1 nm geometric diameter and their corresponding uncertainties for NCCN measurements on August 7 are presented in Figure 3.7. Measurement uncertainties arising from particle counting statistics were included in the calculation of $GR(D_p)$. The effects of error propagation are discussed in the appendix. Growth rates increased systematically with size, and tended to be higher during the afternoon at 13:00 (5.5±0.8 to 7.6±0.6 nm h^{-1}) than during the morning at 09:50 (2.1±1 to 6.0±0.4 nm h^{-1}). These values of the growth rate are consistent with results reported in an earlier study at this site for larger particles (Stolzenburg et al., 2005). We did not attempt to calculate growth rates for particles larger than 3 nm because

the steady-state assumption required for analyzing size distributions from intercepted plumes becomes increasingly questionable as size increases (McMurry 1983).

Previous studies have reported growth rate measurements during the initial steps of aerosol formation (Birmili et al. 2003, Kulmala et al. 2004b, Hirsikko et al. 2005, Stolzenburg et al. 2005, Iida et al. 2008, Manninen et al. 2009, Kuang et al. 2010), with some studies suggesting that diameter growth rates increase with increasing sizes for the smallest particles (Kulmala et al. 2004b, Manninen et al. 2009). While those results were obtained from size distributions of the ambient ion population rather than from the total aerosol population (neutral and charged), such as reported here, their reported growth rate size-dependence is largely substantiated by our results in this study. The results from this study de-couple for the first time the size and time-dependence of observed particle growth rates, due to the new analysis methods which obtain size-dependent growth rates at a specified time. This de-coupling allows the clear interpretation of observed size dependent growth to be an effect of the particle growth mechanism at work.

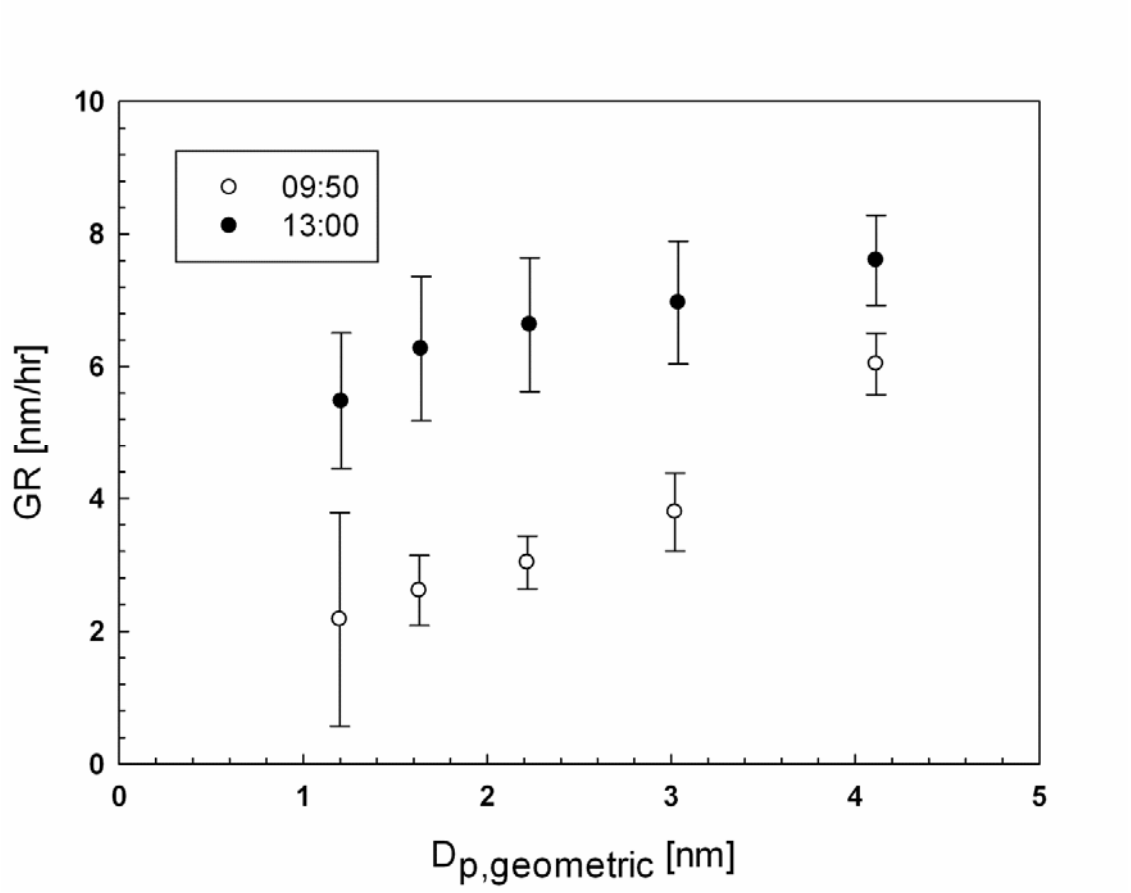

Figure 3.7 Observed growth rates and corresponding uncertainties as a function of particle geometric diameter $D_{p,geometric}$ for NPF events measured on 7 August 2009 (NCCN).

Table 3.1 lists expressions for the size dependent GR derived from predictions of theoretical aerosol growth laws (Friedlander 1977). In these equations, α is the accommodation coefficient, v_m is the molecular volume of the condensing vapor, k is the Boltzmann constant, T is the temperature, P_1 is the partial vapor pressure of the condensing vapor, P_d is the equilibrium vapor pressure of the particle with the diameter of D_p, M_i is the molecular weight, and r is the chemical reaction rate. If the Kelvin effect

is important, then P_1-P_d will be in the form of Eq. 9, where P_s is the saturation vapor over a flat surface and σ is the surface tension.

(9) $$p_1 - p_d = p_1 - p_s \exp[\frac{4\sigma v_m}{D_p kT}]$$

The size-dependence of the observed growth rates can be compared with predictions of theoretical aerosol growth laws, providing information regarding possible mechanisms for aerosol growth. The growth rates observed in Atlanta increase more or less linearly with the increasing particle size, which qualitatively agree with the prediction of the mechanism of droplet-phase reaction. On the other hand, considering vapors can condense on particles more easily when they get larger due to the Kelvin effect, observed results also agree with prediction for molecular bombardment and surface reaction mechanism, assuming multiple different effective vapors to nucleation, other than sulfuric acid, exist in the environment. These result also qualitatively agrees with the nano-kohler theory (Kulmala et al. 2004a). Nano-kohler theory assumes that particle growth is enhanced by curvature-corrected condensation of organic species. And organic and inorganic compounds contribute together for this process. It further assumes that gaseous sulfuric acid condense into particle with ammonia. Thus, a molar ratio of these two compounds in the particle is unity.

Table 3.1 Growth Laws for Gas-to-Particle Conversion

	Mechanism	Growth Law, dD_p/dt
1.	Molecular bombardment	$\frac{2\alpha v_m (p_1 - p_d)}{(2\pi mkT)^{1/2}}$
2.	Surface reaction	$\frac{2\alpha v_m p_1}{(2\pi mkT)^{1/2}} \quad \alpha \ll 1$
3.	Droplet-phase reaction	$\frac{D_p}{3\rho_p}(\sum M_i v_i) r$

3.3.2 Size dependent growth enhancement

Size-dependent growth rate enhancements, $\Gamma(D_p)$, down to 1 nm geometric diameter and their corresponding uncertainties during the morning at 09:50 and the afternoon at 13:00 for the NPF event measured on 7 August 2009 are presented in Fig. 3.8. $\Gamma(D_p)$ can be estimated from Eq. 9, where v_s and N_s are the volume and the concentration of sulfuric acid vapor molecule and $\bar{c}$ is its mean thermal speed.

$$(9)\quad \Gamma(D_p) = \frac{GR}{GR_{SA}} = \frac{GR}{\frac{1}{2} v_s N_s \bar{c}}$$

Measurement uncertainties arising from particle counting statistics and random error in the measurement of $[H_2SO_4]$ were included when calculating the uncertainties in $\Gamma(D_p)$.

At 09:50, $\Gamma(D_p)$ increases with size, from 1.6±1 at 1.2 nm geometric diameter, where sulfuric acid condensation accounts for ~50% of the observed growth, to around 7.3±2 at 4.1 nm geometric diameter, where sulfuric acid condensation accounts for ~10% of the observed growth. During the afternoon at 13:00, a similar size-dependence for Γ was observed, albeit with lower values, ranging from 0.9±0.3 at 1.2 nm geometric diameter, where sulfuric acid condensation accounts for nearly all the observed growth, to around 2.1±0.6 at 4.1 nm geometric diameter, where sulfuric acid condensation accounts for ~40% of the observed growth. These relatively low values of Γ are consistent with earlier observations in Atlanta of sulfuric acid-dominated condensational growth (Stolzenburg et al. 2005, Kuang et al. 2010) and nanoparticles composed primarily of ammonium sulfate (Smith et al. 2005).

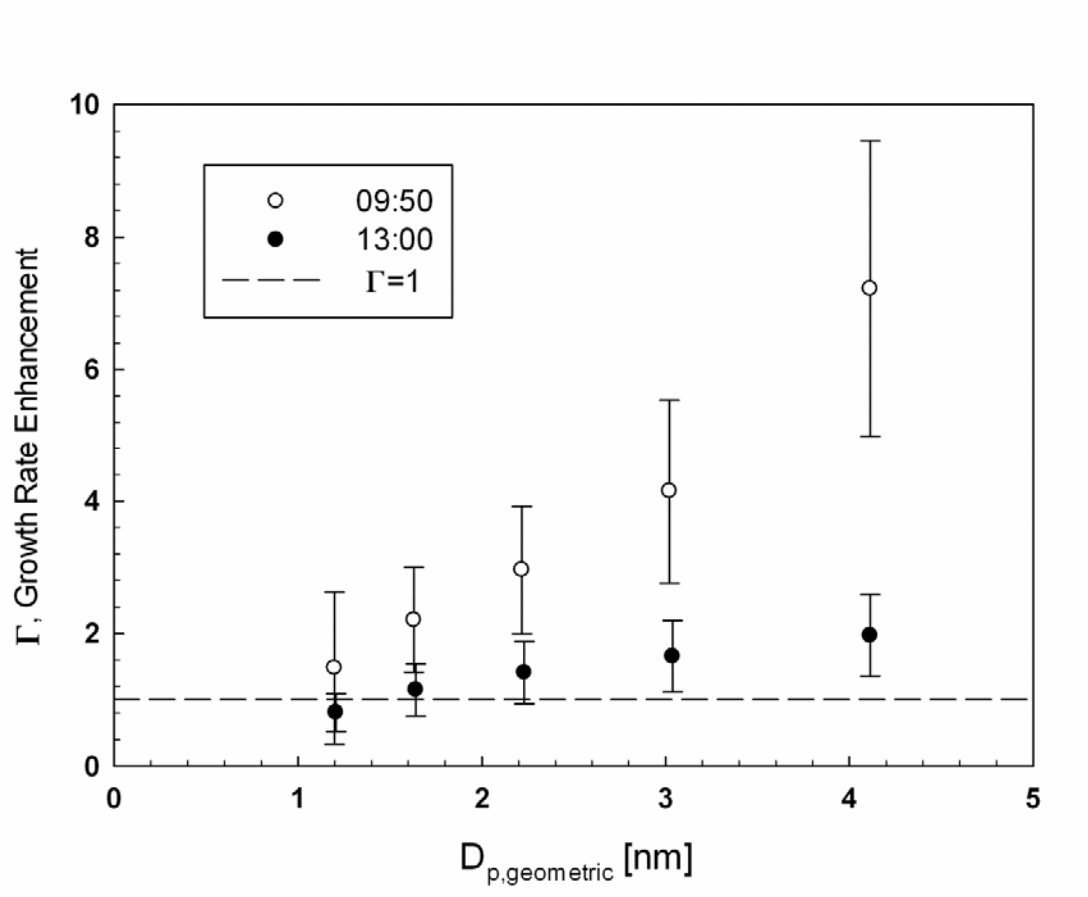

Figure 3.8 Values of the growth rate enhancement Γ and their corresponding uncertainties are plotted as a function of particle geometric diameter $D_{p,geometric}$ for the NPF event observed on 7 August 2009 (NCCN). A dotted line indicating Γ = 1 is shown for reference.

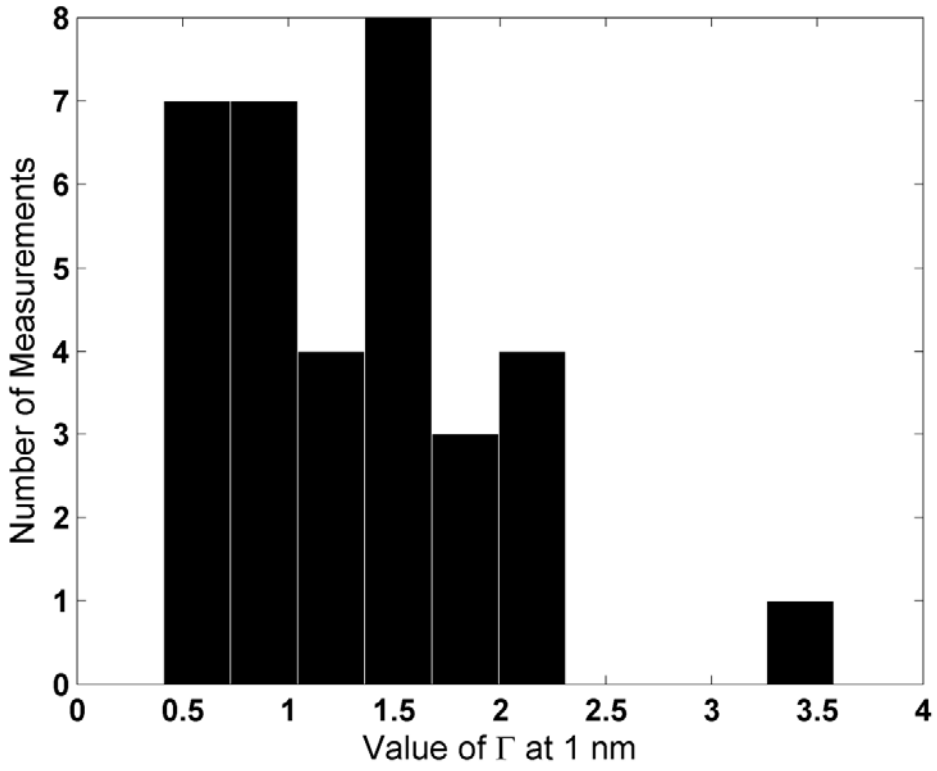

Figure 3.9 Summary of Γ values for all 34 measurements during NCCN. These measurements are from July 25, Aug 7, 12, 22, and 23.

For measurements obtained during NCCN, we were able to carry out the steady state GR calculations for altogether 34 measurements. Figure 3.9 summaries all the Γ values for these measurements at 1 nm geometric diameter. Most of these values (20 out of 34) are larger than one. Γ values are between 0.75 and 1 for 7 cases and between 0.5 and 0.75 for the remaining 7 cases. The values of Γ at the smallest particle sizes provide insights into the nucleation process, namely, upper limit estimates on the critical cluster size. It is worth noticing that $GR_{SA}(Dp)$ is determined by assuming zero evaporative flux of sulfuric acid from the particle surface leading to an upper limit estimate of $GR_{SA}(Dp)$ and,

consequently, a lower limit estimate of Γ in this study. At the size of critical clusters or smaller, evaporation competes with or even overwhelms the sulfuric acid-limited condensation flux, and values of Γ would then be substantially less than 1. Therefore, Γ values greater than unity are only expected at sizes greater than the critical cluster size. For the event at 09:50, for example, Γ = 1.9 at 1.2 nm geometric diameter, indicating that the critical cluster is formed at a smaller size, that the bottleneck to nucleation must occur below 1.2 nm geometric diameter. Our observation in Figure 3.9 that most values of Γ(1 nm) from NCCN campaign are about one implies that the critical sizes for most cases are equal to or less than 1 nm. As is discussed later in the thesis, sulfuric tetramer is about 1 nm in size. Independent analysis of CIMS data supports the argument that tetramer are formed at the sulfuric acid collision rate with trimer and do not subsequently evaporate. Detailed discussion of CIMS data from the NCCN campaign can be found in Chapter 5.

3.3 Summary

The design and performance of the DEG SMPS was described in this chapter. Particle size distributions from the NCCN campaign with this instrument are shown to be in good agreement with independent measurements of the Cluster CIMS for small particles (~1 nm) and of the PSD at larger particle sizes (6-9 nm). A new method that de-couples, for the first time, the size and time-dependence of diameter growth rates for freshly nucleated particles down to 1 nm geometric diameter was developed based on the

measurements. Data analysis methods were developed to obtain size-dependent growth rates at an instant in time for regional and plume NPF events by fitting the aerosol general dynamic equation to measured size distributions. Observed growth rates were found to increase approximately linearly with size from 1 to 3 nm geometric diameter, consistent with predictions from nano-Kohler theory, and Kelvin-limited diffusion, surface, and volume growth laws. Determining which if any of these processes is actually responsible for enhanced growth rates will require information on chemical composition of growing particles and concentrations of gas phase precursors. New instruments will need to be developed to enable such measurements. Corresponding growth rate enhancements Γ were also found to increase approximately linearly with size. Most Γ values obtained during NCCN were around one at 1 nm, indicating the critical cluster of atmospheric nucleation in Atlanta contains approximated four sulfuric acid molecules. Further measurements and analyses of freshly nucleated aerosol number size distributions will help to provide further constraints and insights into ambient nucleation and growth processes, complementing measurements of particle composition by mass spectrometry.

3.4 Supporting Information

3.4.1 Steady state particle size distribution

Previous work has shown that in a nucleating system, steady state concentrations can be achieved for small particles (<5 nm) in time periods of less than about one hour for typical atmospheric conditions (McMurry 1983). This steady state is due to the balance between formation from smaller particles by condensation and coagulation, and removal by coagulation with particles of all sizes. Figure S3.1 shows the simulation results for collision-controlled nucleation in a system that initially contains no particles and with the monomer concentration fixed at 1×10^{8} number/cm^{3}, which is in the range of sulfuric acid vapor concentrations observed in Atlanta during NCCN 2009. Concentrations initially increase rapidly because formation rates exceed coagulation loss rates due to the low particle concentrations present at the start of the nucleation event. After 30 to 60 min, however, quasi-steady state is achieved. The slow, steady decrease in concentrations with time (t) observed after this period is due to the gradual increase in coagulation losses resulting from the increasing aerosol surface area formed by gas-to-particle conversion. For free molecular kinetics, which was assumed in obtaining these illustrative results, coagulation losses vary in proportion to the pre-existing aerosol surface area, which

varies in proportion to $t^{1/5}$, a weak dependence on time (McMurry and Friedlander 1978). With pre-existing aerosols in the atmospheric environment, the quasi-steady-state concentration of the particles will be lower due to the larger scavenging loss. Thus, quasi-steady-state will be reached within shorter time. Although the time dependence for atmospheric aerosols (which fall in the transition regime) will be quantitatively different, it will be similarly weak. It is this weak time dependence that allows the establishment of a quasi-steady-state determined by the instantaneous aerosol size distribution.

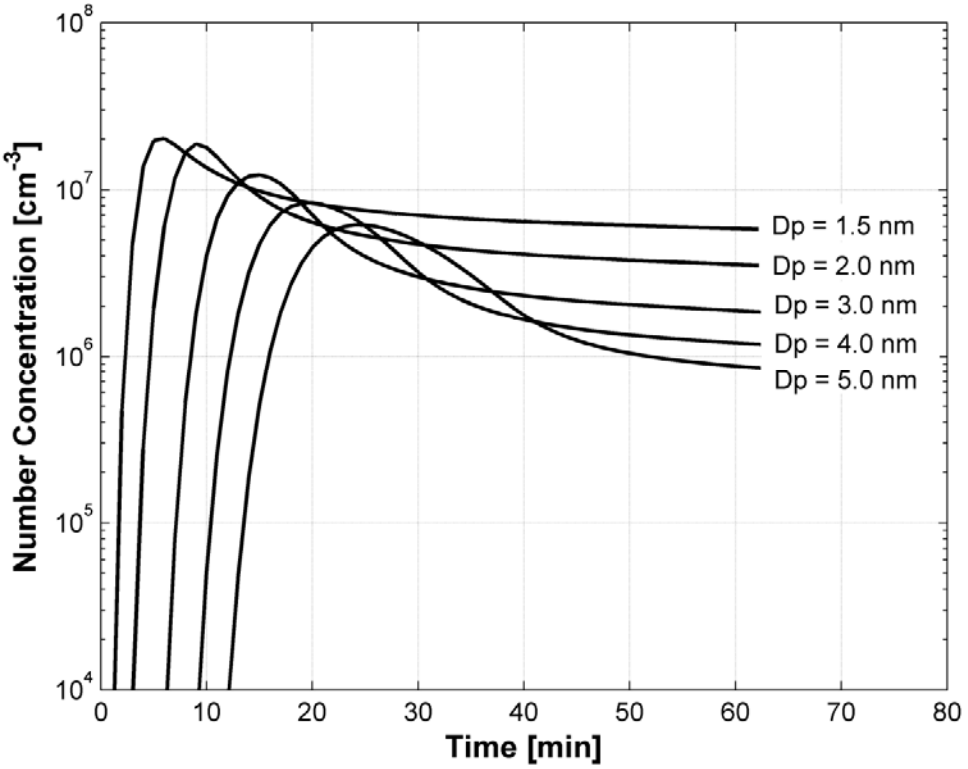

Figure S3.1 Time-dependent particle number concentrations at various particle geometric diameters D_p for collision-controlled nucleation in the free-molecular regime for a system that is initially particle free. For particles smaller than 5 nm, less than an hour is needed to reach a quasi-steady state. After

quasi-steady state is reached, the gradual decrease in number concentrations are due to the increase of aerosol surface area (a coagulation sink), and do not depend explicitly on time.

3.4.2 Model development

During atmospheric regional nucleation events, nucleation can be characterized as chemically and spatially homogeneous. For plume events, like the ones we observed during the NCCN campaign, the size of the nucleation air masses are usually large comparing with the scale of the sampling site. Thus, even though conditions can be different outside the plume, spatial variance inside the plume can still be neglected. The evolution of particles that are growing through simultaneous growth due to gas uptake and coagulation then can be described mathematically with the following population balance equation (GDE) (Gelbard and Seinfeld 1978).

(S1) $$\frac{\partial N}{\partial t}\Big|_{i,i+1} = \left(\frac{\partial N}{\partial t}\right)_{growth}\Big|_{i,i+1} + \left(\frac{\partial N}{\partial t}\right)_{coag}\Big|_{i,i+1}$$

And,

(S2) $$N\Big|_{i,i+1} = \int_{Dp_i}^{Dp_{i+1}} \frac{\partial N}{\partial Dp}\, dDp$$

The first term on the right hand side of equation (S1) is due to condensational growth and the second term is due to coagulation. Equation (S1) states that the change of concentration of particles between diameters *i* and *i*+1 is due to two mechanisms: condensational growth and coagulation.

The condensational growth term can be estimated as:

(S3) $$(\frac{\partial N}{\partial t})_{growth}\Big|_{i,i+1} = J_i - J_{i+1}$$

J is the droplet current, and is defined as,

(S4) $$J_i = \frac{\partial N}{\partial Dp_i} \bullet \frac{dDp_i}{dt}$$

Substituting equation (S4) into equation (S3), and noticing $\frac{dDp_i}{dt}$ is the particle diameter growth rate GR_i, we have,

(S5) $$(\frac{\partial N}{\partial t})_{growth}\Big|_{i,i+1} = \frac{\partial N}{\partial Dp_i} \bullet GR_i - \frac{\partial N}{\partial Dp_{i+1}} \bullet GR_{i+1}$$

The coagulation term can be estimated as:

(S6) $$(\frac{\partial N}{\partial t})_{coag}\Big|_{i,i+1} = +\frac{1}{2}\int_0^{Dp_i}\int_0^{Dp_i}\beta_{1,2}\frac{\partial N}{\partial Dp_1}\frac{\partial N}{\partial Dp_2}dDp_1 dDp_2$$

$$-\int_0^{Dp_i}\int_{Dp_i}^{Dp_{i+1}}\beta_{1,2}\frac{\partial N}{\partial Dp_1}\frac{\partial N}{\partial Dp_2}dDp_1 dDp_2$$
$$Dp_1^3+Dp_2^3>Dp_{i+1}^3$$

$$-\frac{1}{2}\int_{Dp_i}^{Dp_{i+1}}\int_{Dp_i}^{Dp_{i+1}}\beta_{1,2}\frac{\partial N}{\partial Dp_1}\frac{\partial N}{\partial Dp_2}dDp_1 dDp_2$$
$$Dp_{i+1}^3>Dp_1^3+Dp_2^3>Dp_i^3$$

$$-\int_{Dp_i}^{Dp_{i+1}}\int_{Dp_i}^{Dp_{i+1}}\beta_{1,2}\frac{\partial N}{\partial Dp_1}\frac{\partial N}{\partial Dp_2}dDp_1 dDp_2$$
$$Dp_1^3+Dp_2^3>Dp_{i+1}^3$$

With the steady state assumption,

(S7) $$\frac{\partial N}{\partial t}\Big|_{i,i+1} = 0$$

Substituting equations (S5)-(S7) into (S1), leads to,

(S8) $$0 = \frac{\partial N}{\partial Dp_i} \bullet GR_i - \frac{\partial N}{\partial Dp_{i+1}} \bullet GR_{i+1} + \left(\frac{\partial N}{\partial t}\right)_{coag}\Big|_{i,i+1}$$

Equation (S8) is solved by iteration by initially assuming $GR_i = GR_{i+1}$. This is a reasonable starting point provided that bin sizes ΔDp are small enough. So, for each size D_{pi}, we first get,

(S9) $$\overline{GR_i} = -\frac{\left(\frac{\partial N}{\partial t}\right)_{coag}\Big|_{i,i+1}}{\frac{\partial N}{\partial Dp_i} - \frac{\partial N}{\partial Dp_{i+1}}}$$

For subsequent iterations,

(S10) $$GR_i = -\frac{\left(\frac{\partial N}{\partial t}\right)_{coag}\Big|_{i,i+1}}{\frac{\partial N}{\partial Dp_i} - \frac{\partial N}{\partial Dp_{i+1}} \frac{\overline{GR_{i+1}}}{\overline{GR_i}}}$$

The change of the value after the first iteration is smaller than 3%.

For each 15 min measurement of the aerosol size distribution, a smooth curve is fitted to obtain a continuous size distribution. Number distributions were obtained by merging data from the Cluster CIMS and DEG SMPS data as shown in Figure S3.2. The fit to the measured size distribution was performed for sizes ranging from 0.8 nm geometric diameter (clusters containing 3 sulfuric acid molecules) to 5.0 nm geometric diameter.

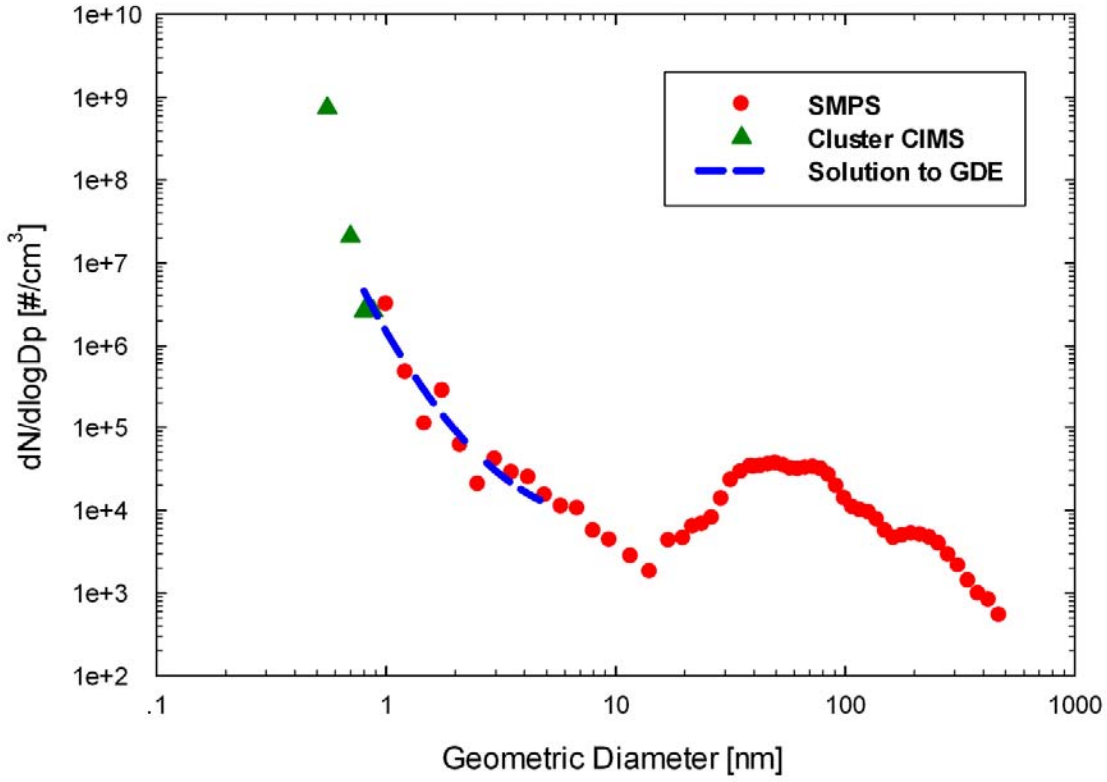

Figure S3.2 Particle size distribution on 13:00, August 7 during NCCN. Triangle data are from the Cluster CIMS, red dots are particle data from the DEG SMPS. The line is obtained by fitting the steady-state solution of the population balance equation to the measurements using size-dependent growth rates as fitting parameters.

3.4.3 Estimated uncertainties

S 3.4.3.1 Uncertainty in particle concentration N_p

Measurements were obtained for 10 discrete size bins in the size range of interest (0.8 to 6 nm), and uncertainties in GR are estimated for the mean size for each bin. The particle concentration N_p for each size bin is:

$$N_p = \frac{C}{\eta_{cpc} f_c \eta_{pene} Q_a} \quad \text{(S11)}$$

where C is the raw counts measured by DEG CPC. Other parameters are the same as defined in Eq. 1. Flow rates of the system are calibrated twice daily and should be accurate within 5% relative uncertainty. Compared with other factors, uncertainty due to variation of the flow rates can be neglected. Charged fractions, f_c, are likely a greater source of uncertainty. We assume that charging rates down to 1 nm can be calculated using Wiedensohler's approximation for Fuchs' diffusion charging theory (Wiedensohler 1988). It is possible that charging rates depend on particle composition, as occurs for chemical ionization of molecular species, but no information on this dependence is available. Lacking experimental data for particles smaller than 2 nm or a theory for evaluating the relative importance of chemical and transport effects on rates of particle charging, the effects of particle composition not considered in this work. It is possible that this approximation leads to some error. The relative uncertainty for C is $\frac{1}{\sqrt{C}}$, which can be derived by assuming that counting is a Poisson process. So, the relative error for N_p can be calculated as,

$$\frac{\Delta N}{N} = \frac{\sqrt{(\frac{\partial N}{\partial C})^2 \Delta C^2 + (\frac{\partial N}{\partial \eta_{CPC}})^2 \Delta {\eta_{CPC}}^2}}{N} = \sqrt{\frac{1}{C} + (\frac{\Delta \eta_{CPC}}{\eta_{CPC}})^2} \quad \text{(S12)}$$

S 3.4.3.2 Uncertainty in GR

For simplicity, the uncertainty of GR due to the uncertainty of D_p is neglected.

Let,

$$A = (\frac{\partial N}{\partial t})_{coag} \quad \text{and} \quad B = \frac{\partial N}{\partial Dp_i} - \frac{\partial N}{\partial Dp_{i+1}}$$

So,

(S13) $$GR_i = -\frac{A}{B}$$

For particles of interest in this analysis (i.e., particles smaller than 5nm), the first two terms on the RHS of Equation (S6) are much greater than the other terms (about four orders of magnitude larger for the bin size we use), which have relative uncertainty approximately $\frac{\Delta N}{N}$. So,

(S14) $$\frac{\Delta A}{A} \approx \frac{\Delta N}{N}$$

For B, $\frac{\partial N}{\partial Dp_i}$ and $\frac{\partial N}{\partial Dp_{i+1}}$ are highly correlated when the bin size is small. The correlation coefficient between $\frac{\partial N}{\partial Dp_i}$ and $\frac{\partial N}{\partial Dp_{i+1}}$, $\rho(\frac{\partial N}{\partial Dp_i}, \frac{\partial N}{\partial Dp_{i+1}})$, is larger than 0.997 for the data sets we use. So,

$$\text{(S15)}\quad \frac{\Delta B}{B}=\frac{\sqrt{(\Delta\frac{\partial N}{\partial Dp_i})^2+(\Delta\frac{\partial N}{\partial Dp_{i+1}})^2-2\cdot\rho(\frac{\partial N}{\partial Dp_i},\frac{\partial N}{\partial Dp_{i+1}})\cdot\Delta\frac{\partial N}{\partial Dp_i}\cdot\Delta\frac{\partial N}{\partial Dp_{i+1}}}}{B}$$

$$\approx\frac{\Delta N}{N}$$

The relative uncertainty of GR is then,

$$\text{(S16)}\quad \frac{\Delta GR}{GR}=\sqrt{(\frac{\Delta A}{A})^2+(\frac{\Delta B}{B})^2-2\cdot\rho(A,B)\cdot\frac{\Delta A\cdot\Delta B}{A\cdot B}}$$

$\rho(A,B)$ is estimated from the data of the whole day, and is found to be between 0.2 and 0.3.

S 3.4.3.3 Uncertainties in growth enhancement Γ

The growth rate enhancement Γ is defined as the ratio of the observed growth rate to the growth rate due to condensation of sulfuric acid only.

$$\text{(S17)}\quad \Gamma=\frac{GR}{GR_{SA}}\sim\frac{GR}{[H_2SO_4]}$$

The relative uncertainty in Γ is,

$$\text{(S18)}\quad \frac{\Delta\Gamma}{\Gamma}=\sqrt{(\frac{\Delta GR}{GR})^2+(\frac{\Delta[H_2SO_4]}{[H_2SO_4]})^2}$$

Sulfuric acid concentration [SA] was calculated according to the following equation (Berresheim et al. 2000):

(S19) $$[SA] = cf_m \frac{1}{kt} \ln(1 + \frac{S_{SA}}{S_{\mathrm{Re}}})$$

Propagating the uncertainties in the individual terms in Eq. (S19) yields an overall relative systematic uncertainty of ±30% for the measurement of [SA]. Detailed discussion can be find in (Kuang et al. 2012b).

Chapter 4: Chamber Study of Amine on Sulfuric Acid Particle Formation and Growth

4.1 Introduction

Recent studies have shown that atmospheric nucleation can contribute significantly to particle concentrations in the atmosphere (Spracklen et al. 2008b, Adams and Seinfeld 2003). When these particles grow larger, they can serve as cloud condensation nuclei (CCN), and influence the global radiation balance (Zhang et al. 2010b). The newly formed ultrafine aerosols may also have an adverse impact on human health (Stieb et al. 2002, Wichmann and Peters 2000). The correlation between sulfuric acid and atmospheric nucleation is well established. Weber and coworkers (1996) showed that, in the atmospheric boundary layer, the relationship between the formation rate of 3 nm particles (J_{3nm}) and sulfuric acid concentration ($[H_2SO_4]$) follows $J_{3nm} \sim [H_2SO_4]^P$, where $1 \leq P \leq 2$. The two limits (P=1 and P=2) correspond to the "activation" nucleation model (Kulmala et al. 2004a, Kulmala, Lehtinen and Laaksonen 2006) and the "kinetic" nucleation model (McMurry and Friedlander 1979, McMurry 1980) respectively. Recent

observations support this relation (Sihto et al. 2006, Riipinen et al. 2007, Kuang et al. 2008, Paasonen et al. 2009, Jokinen et al. 2012). Cases when P>2 have also occasionally been reported (Wang et al. 2011).

Sulfuric acid alone, on the other hand, cannot explain the fast nucleation rate observed in the atmosphere. The classical binary theory for nucleation of sulfuric acid and water (Doyle 1961, Vehkamaki et al. 2002) fails to explain both the observed rates of nucleation in the atmosphere and the functional dependence of nucleation rates on sulfuric acid concentration (Chen et al. 2012). Laboratory studies (Hanson and Lovejoy 2006) and recent computational work (Ortega et al. 2012) also shows that pure sulfuric acid clusters are highly unstable under typical atmospheric conditions, and that other chemical species are needed in order to form stable clusters. The effect of amines in enhancing sulfuric acid based nucleation has been discussed recently (Yu et al. 2012, Zollner et al. 2012, Ortega et al. 2012, Kirkby et al. 2011, Berndt et al. 2010, Bzdek, Ridge and Johnston 2011). Experiments have shown that amines at ppt mole fractions enhance the formation rates of particles larger than 2 nm by orders of magnitude (Zollner et al. 2012, Yu et al. 2012).

In this work, we studied the effect of amines on sulfuric acid nucleation inside a reaction chamber. Particle concentration was measured with a traditional particle size distribution system (PSD) (Woo et al. 2001) and the diethylene glycol based scanning mobility particle spectrometer (DEG SMPS) (Iida et al. 2009, Jiang et al. 2011b). One cluster

chemical ionization mass spectrometer (cluster-CIMS) (similar to the one describe by Zhao et al. 2010) was used for measuring the concentrations of sulfuric acid vapor and of molecular clusters that contained sulfuric acid. Details about the design and the calibration of this mass spectrometer can be found in the thesis of Dr. Titcombe (2012). Information about cluster-CIMS data analysis and background correction during the chamber study can also be found in the work of Chen et al. (2012). An ambient pressure portion transfer mass spectrometer (AmPMS) (Hanson et al. 2011b) was used to sample basic gas species (ammonia and amine). Compared with other recent flow tube nucleation studies (Zollner et al. 2012, Yu et al. 2012, Brus et al. 2011, Benson et al. 2011, Berndt et al. 2010), this chamber study was carried out with sulfuric acid concentrations and nucleation time scale more comparable with atmospheric nucleation. The effect of amine on particle nucleation and growth was investigated by carrying out experiments with and without the intentional addition of amines. In this chapter, discussion focuses mainly on particle measurements. Implications from cluster-CIMS measurement are discussed in the next chapter.

4.2 Experiment Setup

Figure 4.1 briefly illustrates the experimental setup for the University of Minnesota chamber study. Clean air used in this system was generated by passing compressed air through coalescing filters (R26/R08-02, Wilkerson Corp.) and a pure air generator (Aadco Instruments, model 737–12a). Its relative humidity was controlled by passing a

potion though 5% sulfuric aqueous solution, which also helped to remove the possible ammonia residue in the clean air. The ammonia residue in the dry portion of clean air was removed by passing it through a filter impregnated with sulfuric acid. (These parts were included in the "humidifier" part in Figure 4.1.) The clean air and reactants (ozone and sulfur dioxide gases) were sent into the chamber from the top. The reaction chamber used in this study was a 1000 L Teflon bag. The temperature of the bag was controlled with a constant-temperature circulating bath. Two Ultra Violet lamps were installed on two sides of the stainless steel enclosure that held that bag. The sampling port was at the bottom of the chamber. Nucleated particles were measured with PSD and DEG SMPS every 5 minutes. The Cluster-CIMS and AmPMS sampled clusters and basic gaseous compounds. A more detailed description of this setup can be found in the PhD. thesis of Dr. Titcombe (2012).

Before each day of experiments the bag was cleaned by flushing with clean air and bathing with ozone and UV radiation over night. Checked with PSD and DEG SMPS, the particle concentration inside the chamber was ensured to be negligible (lower than 1 count in 5 min sampling time) before each experiment. Background particle concentrations were also checked in the "dark condition" (chamber filled with reactants, UV lights off). No observable new particle formation was found in this case. During a typical experiment, the chamber was first filled with clean air. Ozone and sulfur dioxide were added when the bag was near capacity. UV lights were then turned on to initiate the reactions that lead to nucleation. With water vapor present, OH radicals can be produced

by O_3 photolysis. These radicals can then react with SO_2 to form gas phase sulfuric acid (Seinfeld and Pandis 2006). Typical experimental run time, to about half deflation of the Teflon bag, was 45 minutes. Dimethyl amine was intentionally added to the chamber during some experiments. However, various amines were always detected in the chamber at levels of at least tens of pptv (protonated m/z 32+46+60+74+88). Matsunaga and Ziemann (2010) found that fluorinated ethylene propylene Teflon reactors store secondary organic aerosol reaction products that are released back to the chamber when it is filled with clean air. A similar process likely occurs with amines. Total concentrations of amines for all the experiments range from 0.8 to 31 ppbv. At the higher concentration, dimethyl amine was the dominant amine. The term "amine concentration" used in following sections refers to the total concentration for all types of amines detected in the chamber.

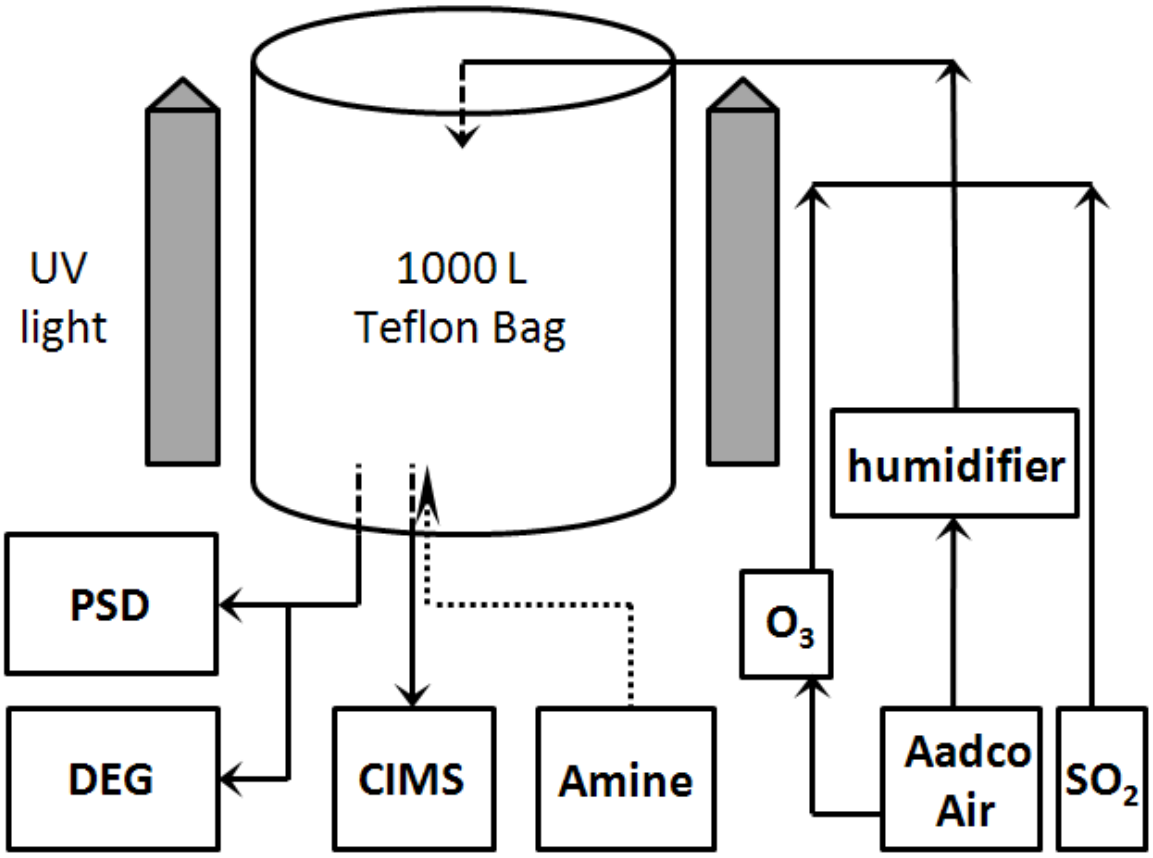

Figure 4.1 Schematic of the nucleation reaction chamber system. Amines were added through the Cluster-CIMS and AmPMS sampling inlet at the beginning of each experiment before UV lights were turned on. Part of the Aadco air was sent through 5% sulfuric acid solution to add water vapor (humidifier, details are not shown here).

4.3 Results and discussion

4.3.1 Particle size distribution in amine and non-amine experiments

During the reaction chamber study, 24 experiments were carried out. Dimethyl amine was intentionally added in 6 of these experiments (referred to as amine experiments). Amine concentrations were between 5×10^{10} and 8×10^{11} cm^{-3} for these experiments. For the other 18 experiments, amine concentrations were between 2×10^{10} and 5×10^{10} cm^{-3} even though no amine was added (referred to as non-amine experiments). Figures 4.2(a) and 4.2(b) show typical particle size distributions measured by the DEG SMPS and Cluster-CIMS during a non-amine experiment and an amine experiment. The time range on the figure for the non-amine experiment is from 9 min to 30 min after UV lights were turned on. Particle concentrations between 1 nm and 5 nm became very low after 30 minutes. For the amine experiment, size distributions are plotted for the duration of the experiment. Particle size distributions at a given time are determined by the initial size distribution, the concentration of the nucleating species, the particle formation and growth rates, and losses of vapor and clusters to the surfaces of preexisting aerosols and the chamber wall. Both experiments were started from a clean chamber background, thus the initial state and the surface area of the existing aerosols were similar. Steady state sulfuric acid concentrations in these two experiments were similar (3.16×10^{8} cm^{-3} for the non-amine experiment and 3.16×10^{8} for the amine experiment). Thus, the particle size distributions during these two experiments reflected the particle formation and growth rates. That is, the higher steady state values of particle size distributions during

the amine experiment indicates that particles formed in this case are formed more efficiently and grow faster.

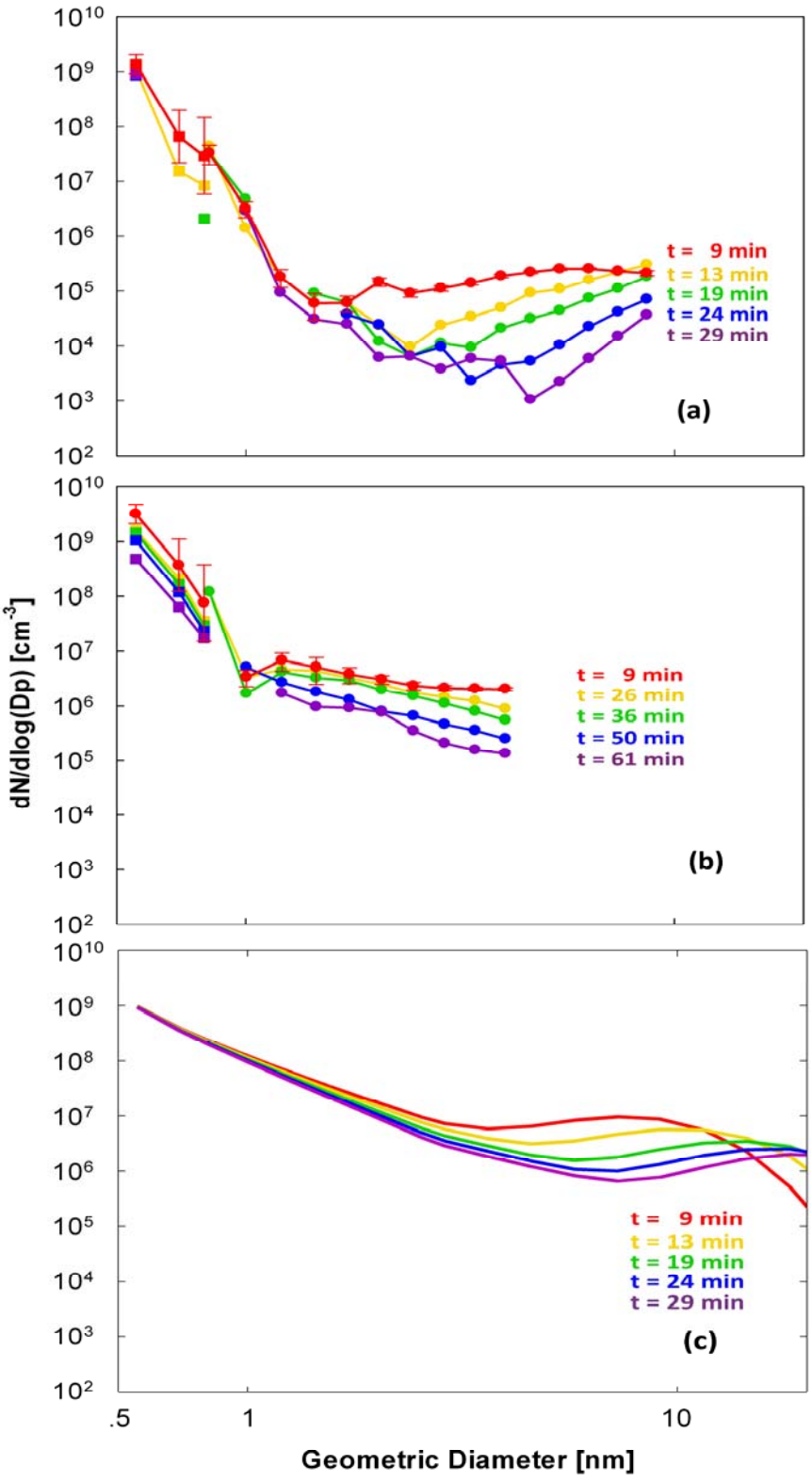
dN/dlog(Dp) [cm-3]
Geometric Diameter [nm]
t = 9 min
t = 13 min
t = 19 min
t = 24 min
t = 29 min
(a)
t = 9 min
t = 26 min
t = 36 min
t = 50 min
t = 61 min
(b)
t = 9 min
t = 13 min
t = 19 min
t = 24 min
t = 29 min
(c)
.5
1
10

Figure 4.2 Particle size distributions in (a) a non-amine experiment; (b) an amine experiment; and (c) a collision-limited simulation. Particle concentrations became too low to be detected after 30 minutes in the non-amine experiment, while sub-5 nm size distribution did not change much throughout the amine experiment.

Particle size distributions in both cases are compared with the simulation result predicted from a collision-limited nucleation model (McMurry 1983) (Figure 4.2(c)). These calculations assume that that sulfuric acid is leads to nucleation and growth, and that the process is collision-limited. In other words, hard-sphere collision rate constants are used to determine cluster formation rates, and the evaporation of sulfuric acid from those clusters is neglected. The dynamics of particle formation is described by the following equations (Gelbard and Seinfeld 1979, McMurry 1983).

(1) $\frac{\partial N_1}{\partial t} = R - N_1 \cdot \sum_{i=1}^{\infty} \beta_{1,i} \cdot N_i - \beta_{1W} \cdot N_1$

(2) $\frac{\partial N_k}{\partial t} = \beta_{1,k} \cdot N_1 \cdot N_{k-1} + \frac{1}{2} \sum_{i=2}^{k-2} \beta_{i,k-i} \cdot N_i \cdot N_{k-i} - N_k \cdot \sum_{i=1}^{\infty} \beta_{i,k} \cdot N_i - \beta_{kW} \cdot N_k$

where R is the formation rate of the sulfuric acid monomer. The value of R is assumed to be constant during the experiment and is so chosen that the steady-state concentration of sulfuric monomer is the same as the value observed during chamber experiments (3×10^8 cm^{-3}). The symbol N_k stands for the concentration of the particles containing k sulfuric molecules. $\beta_{i,j}$ is the coagulation frequency function between particles containing only i and j sulfuric molecules (Friedlander 1977), though $\beta_{i,j}$ can be slightly different in reality due to water and basic gas molecules attached.

The loss of size-k clusters to the chamber walls is quantified by the first order rate constant β_{kW}. The values of β_{kW} used in this work were calculated based on the work of Okuyama et al. (1986) (Eq. (13) in the original paper).

$$(3)\ \beta_{kW} = (\frac{S_T}{V_T})(\frac{D}{\delta}) + \frac{u_t}{H}$$

In this equation, S_T and V_T are the total inner surface area and the total volume of the reaction chamber. Their values are estimated to be 3.8 m^2 and 1 m^3 respectively. Coefficient D (cm^2s^{-1}) is the particle diffusion coefficient, H is the height of the chamber (1.2 m), and δ (cm) is the boundary layer thickness. The value of δ can be experimentally determined. In this work, the approximated Eq. (4) developed by Okuyama et al. (1986) is used to estimated its value. The setting velocity, u_t, can be estimated by Eq. (5).

$$(4)\ \delta = 2.884D^{1/3}$$

$$(5)\ u_t = \frac{Cm(\rho_p - \rho_f)D_p{}^2 g}{18\mu}$$

where Cm is Cunningham's correction factor, ρ_p is the particle density, D_p is the particle diameter, g is the acceleration of gravity, ρ_f is the density of the gas, and μ is the viscosity of air. Wall loss estimated in this way agrees with the experimental results from McMurry and Radar (1985) within a factor of two. Wall losses in this study were small compared with other loss terms.

Qualitative similarities can be observed in these figures. For the non-amine experiment and collision-limited simulation, particle size distributions monotonically drop from

smallest size (around 0.6 nm) until a local minimum is reached. Different from the collision-limited simulation, the minima in the non-amine experiment (Figure 4.2a) occurred at smaller particle sizes. Particle concentrations at the local minima were also lower in the non-amine experiment. Values of the particle size distribution in the amine experiment (Figure 4.2b) are higher than in the non-amine experiment, and are close to the ones shown in Figure 4.2(c). In the collision-limited model, no growth enhancement is assumed (i.e., contributions of species other than sulfuric acid to particle growth rates are not included). The fact that steady-state particle size distributions observed in the experiments are lower than modeled results indicates that particle formation rates in the chamber study are below the collision-controlled rates. We infer, therefore, that sulfuric acid evaporation must occur at small cluster sizes in these experiments.

4.3.2 Growth enhancement factors for chamber experiments

The particle growth rate enhancement factor (Γ), defined as the actual growth rate divided by the growth rate due to collision-limited sulfuric acid vapor condensation (Weber et al. 1997, Kuang et al. 2012b), reflects the relative importance of sulfuric acid in particle growth. Γ values larger than one indicate that particle growth is enhanced by species other than sulfuric acid. Γ values will be smaller than one when particles are not stable and evaporation occurs. Calculations similar to those described in Chapter 3 were carried out for chamber experiments. Results at 1.1 nm are summarized in Figure 4.3. Steady-state growth rates were calculated for 15 out of the 24 experiments (4 of them

were amine experiments). For the remaining experiments, particle concentrations measured with the DEG SMPS were not high enough to allow calculations of growth rates after steady state number distributions were reached. Γ values were smaller than 0.5 at 1.1 nm for all non-amine experiments (in 6 experiments Γ was below 0.2) and between 0.6 and 1 for all amine experiments. This difference clearly indicates that these 1.1 nm particles formed in the presence of high amine concentrations are much less volatile. Amines likely react with the sulfuric acid-containing clusters, thereby stabilizing them (i.e., decreasing the sulfuric acid evaporation rates from the clusters) (Ortega et al. 2012, Chen et al. 2012). At a given sulfuric acid concentration, higher concentrations of small, stable clusters will lead to higher particle formation rates (derivation can be found in the following chapter). Thus, results from this study are qualitatively consistent with observations from recent flow tube experiments (Yu et al. 2012, Zollner et al. 2012) which showed that amines enhance rates at which particles nucleate in the presence of sulfuric acid vapor.

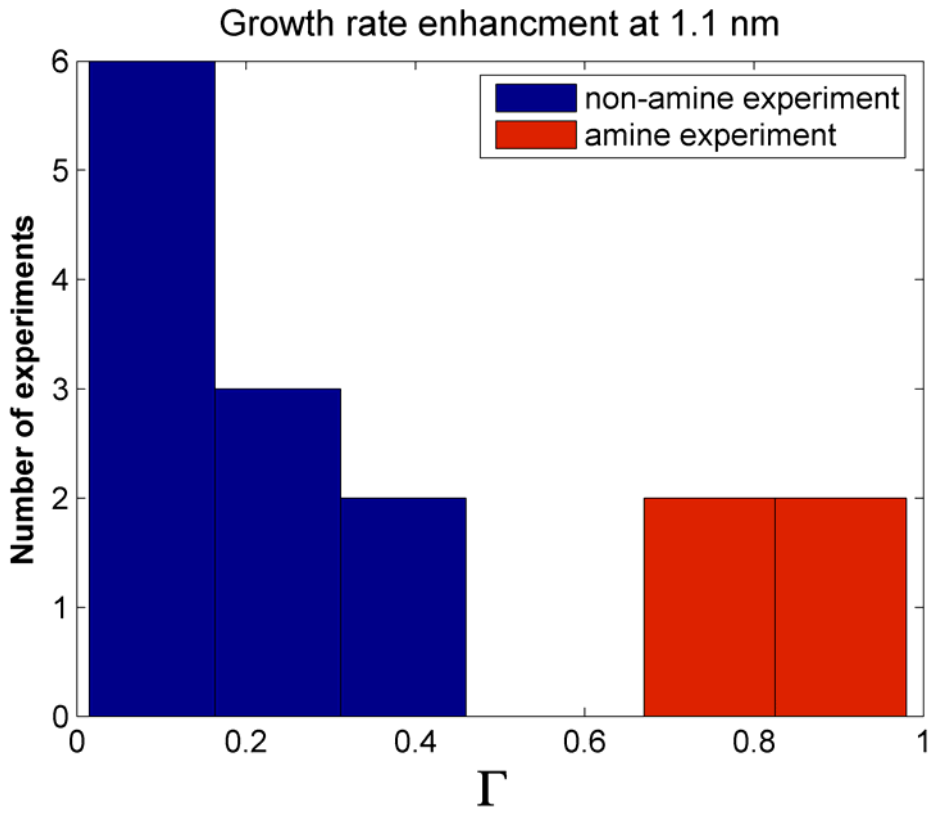

Figure 4.3 Growth rate enhancement factor Γ at 1.1 nm.

Examples of Γ as a function of particle size are presented in Figure 4.4. From bottom to top, results from a non-amine experiment and two amine experiments (medium and high amine concentrations) are compared with Γ values from a typical case obtained during Atlanta 2009 NCCN field campaign (solid line in Figure 4.4). In the non-amine experiment (amine concentration about 10^{10} cm^{-3}), Γ starts from about 0.05 at 1 nm and reaches about 0.6 at 3.5 nm. Γ values are from 0.5 to 0.6 and from 0.6 to 1 in the amine experiments with medium (7×10^{10}) and high (3×10^{11}) concentrations of amine respectively. In all cases, Γ values increase as particle diameter increases. However, different from observations in the field, Γ values never exceed 1.5 for all chamber

experiments even at particle sizes as large as 3 nm. It has been shown that oxidation products of volatile organic compounds constitute up to 90% of the submicron aerosol mass and can drive the new particle formation process as observed in many rural and urban areas (Smith et al. 2005, Smith et al. 2010). It seems that, though amines help to stabilize the newly formed sulfuric acid clusters at small sizes, they do not contribute significantly to their subsequent growth. This result qualitatively agrees with previous modeling results, which showed the uptake of basic gases, including ammonia and amines typically explains only a small fraction of the particle growth (Weber et al. 1998).

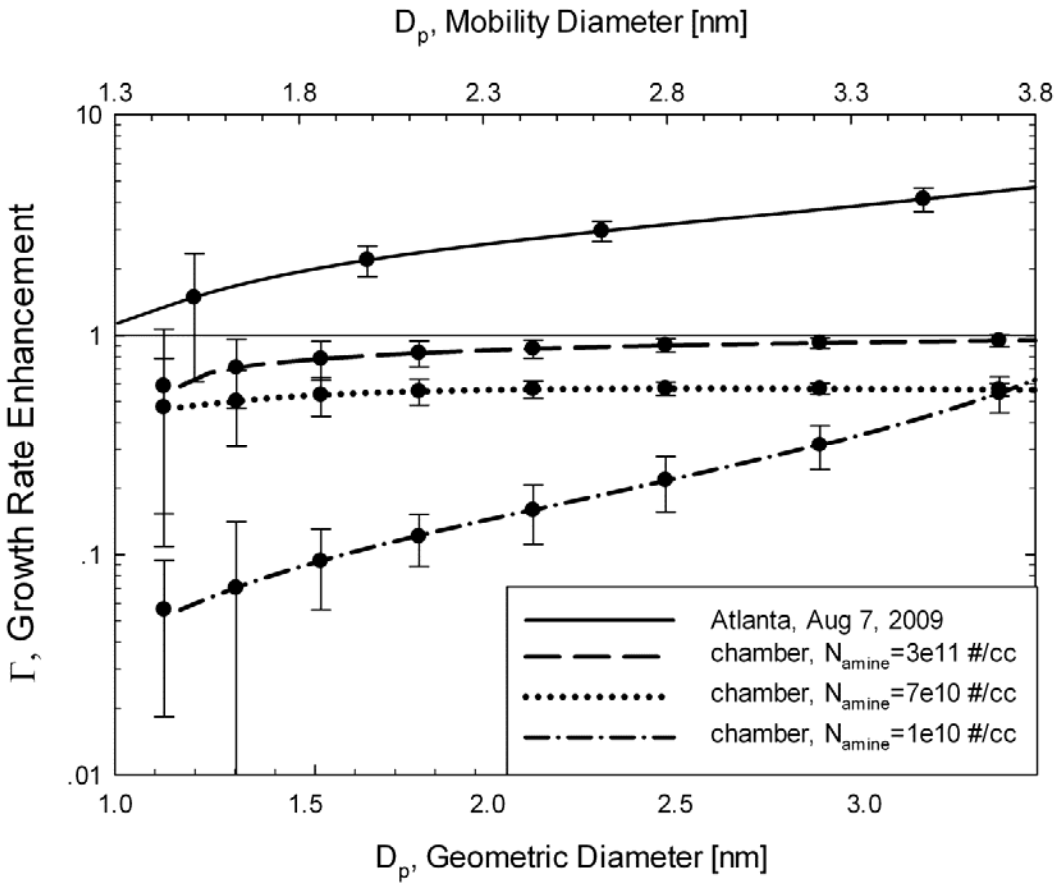

Figure 4.4 Growth rate enhancement factor Γ as a function of particle diameter.

4.4 Summary

This chapter discussed results from laboratory chamber experiments aimed at studying the early steps in the formation and growth of particles from vapors including sulfuric acid, amines and water. The analysis focused on measurements carried out with the Cluster CIMS and the DEG SMPS, the first time measurements of neutral molecular clusters and size distributions down to 1 nm have been reported for laboratory chamber experiments. The analysis in this chapter focused on the effect of amine concentrations on size-resolved concentrations and growth rates of particles in the 1 to 3 nm size range. Comparison between the results from these chamber experiments and numerical simulation shows that particles are formed in the chamber at less than the collision limited rates. Steady-state growth rate calculations carried out using the approach described in Chapter 3 are shown for 15 experiments from the chamber. Growth rate enhancement factors, Γ, are significantly larger in experiments with high amine concentrations than in experiments with low amine concentrations. As was observed for ambient observations in Atlanta, Γ values increase as particle size increases indicating that large particle stability increases with increasing size. However, Γ values never exceed 1.5 during all chamber experiments. These results support previous laboratory observations and theoretical calculations that amines can enhance nucleation rates for a given concentration of sulfuric acid vapor. The difference between chamber and field Γ

values implies that amines cannot explain the high values of Γ (i.e., contributions of species other than sulfuric acid to growth rates) that have been observed in the atmosphere. The contribution of other chemical species to particle growth, most likely various organic compounds, is high in areas where a large growth rate enhancement factor Γ was observed.

4.5 Supporting information

4.5.1 Sulfuric concentration decay rates inside the chamber

The change of sulfuric acid monomer concentration inside the chamber, as described by equation (S1), is determined by its formation rate, scavenging rate by other particles, the losses to the chamber walls, and evaporation from particles. The last term in equation (S1) accounts for the evaporation, where E_i is the evaporation rate constant of the particles containing i sulfuric acid monomers.

$$\text{(S1)}\ \frac{\partial N_1}{\partial t} = R - N_1 \cdot \sum_{i=1}^{\infty} \beta_{1,i} \cdot N_i - \beta_{1W} \cdot N_1 + \sum_{i=2}^{\infty} E_i \cdot N_i$$

After the UV lights are turned off, OH radical production will stop. Residual OH radicals will be consumed within seconds (Kovacs and Brune 2001). The decay rate of sulfuric acid monomer in this case can then be described by equation (S2).

$$\text{(S2)}\ \frac{\partial N_1}{\partial t} = -N_1 \cdot \sum_{i=1}^{\infty} \beta_{1,i} \cdot N_i - \beta_{1W} \cdot N_1 + \sum_{i=2}^{\infty} E_i \cdot N_i$$

If all the particles formed in the chamber are all stable, that is, if E_i equals zero, sulfuric acid monomer will decay at a faster rate than when particles evaporate. This rate is defined as "theoretical decay rate (R_T)" and can be calculated from the particle size distribution, as shown by Equation S3:

(S3) $$R_T = \frac{\partial N_1}{\partial t} = -N_1 \cdot \sum_{i=1}^{\infty} \beta_{1,i} \cdot N_i - \beta_{1W} \cdot N_1$$

Comparing the theoretical decay rate and the actual decay rate (R_E) after the UV lights were turned off provides an independent way of estimating the relative importance of particle evaporation inside the system.

Sulfuric acid monomer decay tests were carried out during four "non-amine" chamber experiments (on July 14, July 15, and two experiments on July 16). UV lights were turned off after about 45 minutes. Sulfuric acid monomer concentrations were continuously monitored by the cluster-CIMS (Figure S4.1). The actual decay rates are estimated by equation (S4), where Δt is the time period between UV lights off and the end of the experiment and ΔN stands for the change in sulfuric acid monomer concentration during the same period.

(S4) $$R_E \approx \frac{\Delta N}{\Delta t}$$

R_E and R_T values in these four experiments are summarized in table S4.1. Theoretical decays are always several orders of magnitude larger than the actual decay rates. Small actual decay rates indicate that the sulfuric acid clusters are unstable. Evaporation rates of these clusters should be fairly high in order to explain the difference between R_E and R_T. Results of these decay tests are consistent with the growth rate enhancement factor calculation, showing small clusters formed in the chamber are unstable.

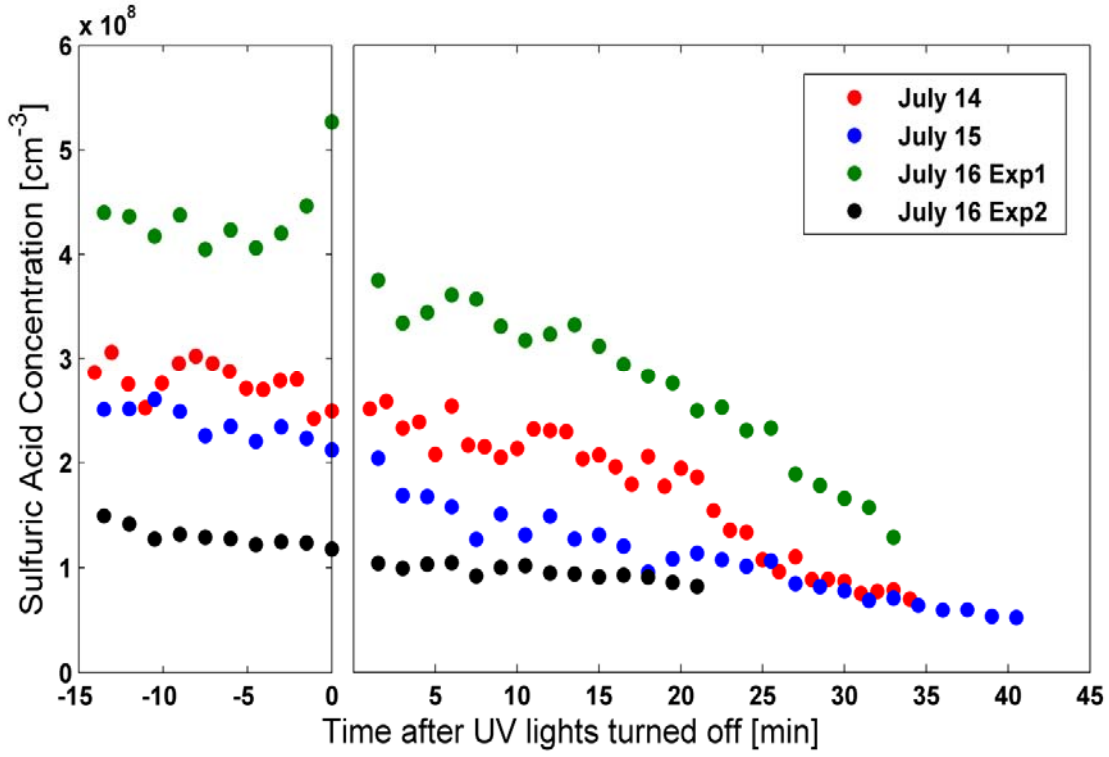

Figure S4.1 Sulfuric acid decay rates during four experiments after UV lights turned off.

Table S4.1. Comparison between observed and calculated sulfuric acid decay rates.

Experiments	estimated decay rate (R_E $cm^{-3}s^{-1}$)	theoretical decay rate (R_T $cm^{-3}s^{-1}$)
7.14	8.63×10^{4}	3.14×10^{7}
7.15	6.67×10^{4}	3.01×10^{7}
7.16 exp1	2.21×10^{5}	1.74×10^{8}
7.16 exp2	2.97×10^{4}	5.97×10^{6}

4.5.2 Modal growth rate of particles formed inside the chamber

Model growth rates for particles measured in the chamber experiments were calculated using an approach similar to that described by Stolzenburg (2005). Both gas-to-particle conversion and coagulation contribute to observed particle growth rates. This analysis identifies contributions of coagulation and gas-to-particle conversion to growth. Growth rates due to gas-to-particle conversion during an experiment are assumed to be constant, independent of size and time. Lognormal size distributions are used to fit the nucleation mode.

Particle coagulation can affect the model mean diameter in two ways. Coagulation of particles within the freshly nucleated mode will lead to an increase the modal diameter. When the modal concentration is high, this effect can be significant. In this study, the effect is quantified analytically with the method described by Lee et al (1990) assuming that particles are in the free molecule regime. Extramodal coagulation with large, preexisting aerosols would also increase the observed modal diameter growth rates. However, since preexisting aerosol concentrations can be neglected in this chamber study, this effect is not important.

Figure S4.2 shows the modal growth rates due to sulfuric acid condensation for aerosols with number modal sizes ranging from 10 to 40 nm (depending on the experiment).

These results apply to all chamber experiments; contributions of coagulation to modal growth rates have been subtracted to obtain these results. The dashed line is the collision-limited sulfuric acid condensation growth rate. Particle modal growth rate on average is about 1.8 times larger. Therefore, the growth rate enhancement factor Γ for these large particles during chamber experiments is about 1.8. Noticing that Γ is smaller than 1 for particles around 1 nm in these experiments, the growth of larger particles are clearly enhanced by other chemical species to some extent. Also, consistent with the previous conclusion that amines only contribute a small fraction of particle growth, no clear difference between amine and non-amine experiments is observed on modal growth rate.

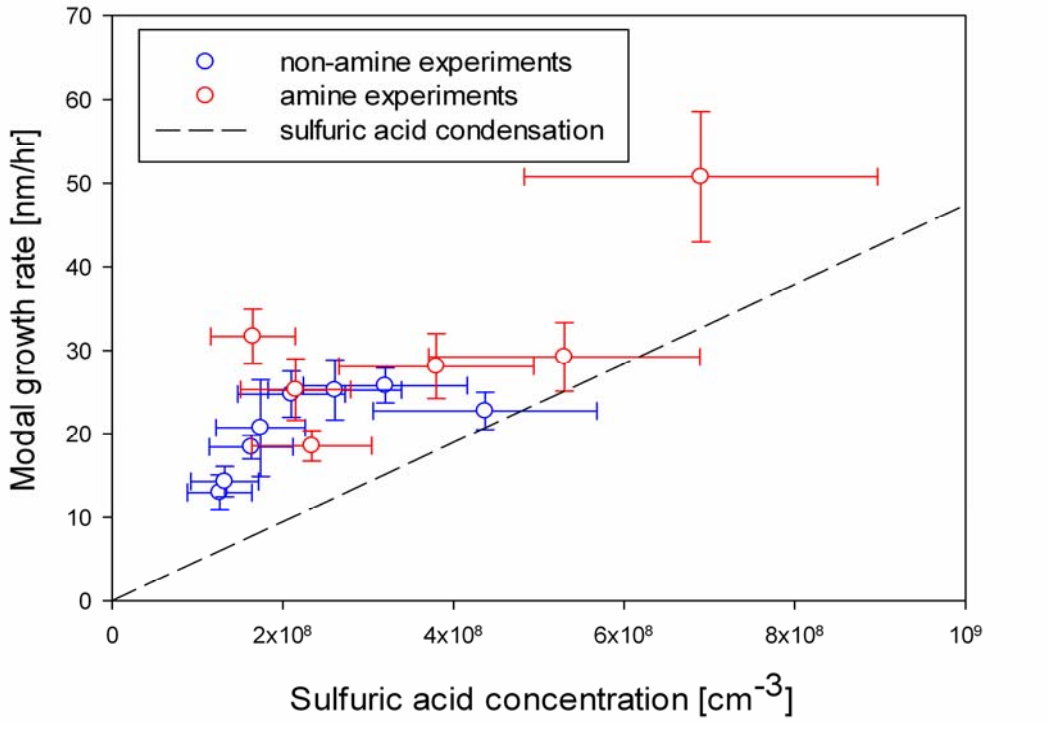

Figure S4.2 Particle modal growth rate as a function of sulfuric acid monomer concentration during chamber experiments.

Chapter 5: An Acid-Base Chemical Reaction Model for Nucleation Rates in the Polluted Atmospheric Boundary Layer*

5.1 Introduction

Atmospheric nucleation happens frequently in the troposphere boundary layer (Kulmala et al. 2004c). Previous work suggests that stable clusters formed from gas phase chemicals are smaller than 3 nm (Kulmala, Pirjola and Makela 2000, Kulmala et al. 2007b, Kuang et al. 2012b). After these clusters are formed, they can grow at typical rates of 1-10 nm/h (Weber et al. 1997, Dal Maso et al. 2005, Iida et al. 2008, Kuang et al. 2012b) due to the condensation of sulfuric acid and organic species (Weber et al. 1996, Stolzenburg et al. 2005, Hirsikko et al. 2005, Kuang et al. 2010, Spracklen, Bonn and Carslaw 2008a, Laaksonen et al. 2008, Smith et al. 2008). Field studies and numerical simulations have shown that when these particles grow larger, they can contribute

* Aspects of the results described in this chapter (including some text and figures) have been published in Chen et al. (2012).

significantly to concentrations of cloud condensation nuclei (Lihavainen et al. 2003, Laaksonen et al. 2005, Kerminen et al. 2005, Spracklen et al. 2008b, Pierce and Adams 2009, Pierce and Adams 2007), and ultimately alter the Earth's radiation balance (Leaitch et al. 2010, Ghan et al. 2001). Unlike the long-term effects of greenhouse gases, which have been quite well quantified, the influence of aerosols on climate change is still highly uncertain (IPCC 2007, Liao et al. 2009, Kazil et al. 2010, Gong et al. 2011). Our imperfect understanding of the atmospheric nucleation mechanism contributes to these uncertainties.

Figure 5.1 summarizes results for the dependence of boundary layer nucleation rates on the concentration of sulfuric acid vapor, "$[H_2SO_4]$", measured by the University of Minnesota-National Center for Atmospheric Research (NCAR) research team over the past two decades (Kuang et al. 2008). Also included are data from the University of Helsinki group (Sihto et al. 2006, Riipinen et al. 2007). The considerable scatter in the measurements of the nucleation rate J at a given value of $[H_2SO_4]$ may be due to factors including dependencies on other nucleation precursor gases, temperature, and relative humidity (RH), as well as uncertainties introduced when J is deduced from measurements. Significantly, Figure 5.1 shows that for all of these studies nucleation rates range from 1×10^{-2} to 5×10^{-6} times the sulfuric acid vapor collision rate, $0.5k_{11}[H_2SO_4]^2$, where k_{11} is the hard-sphere collision rate constant for sulfuric acid vapor (Weber et al. 1996).

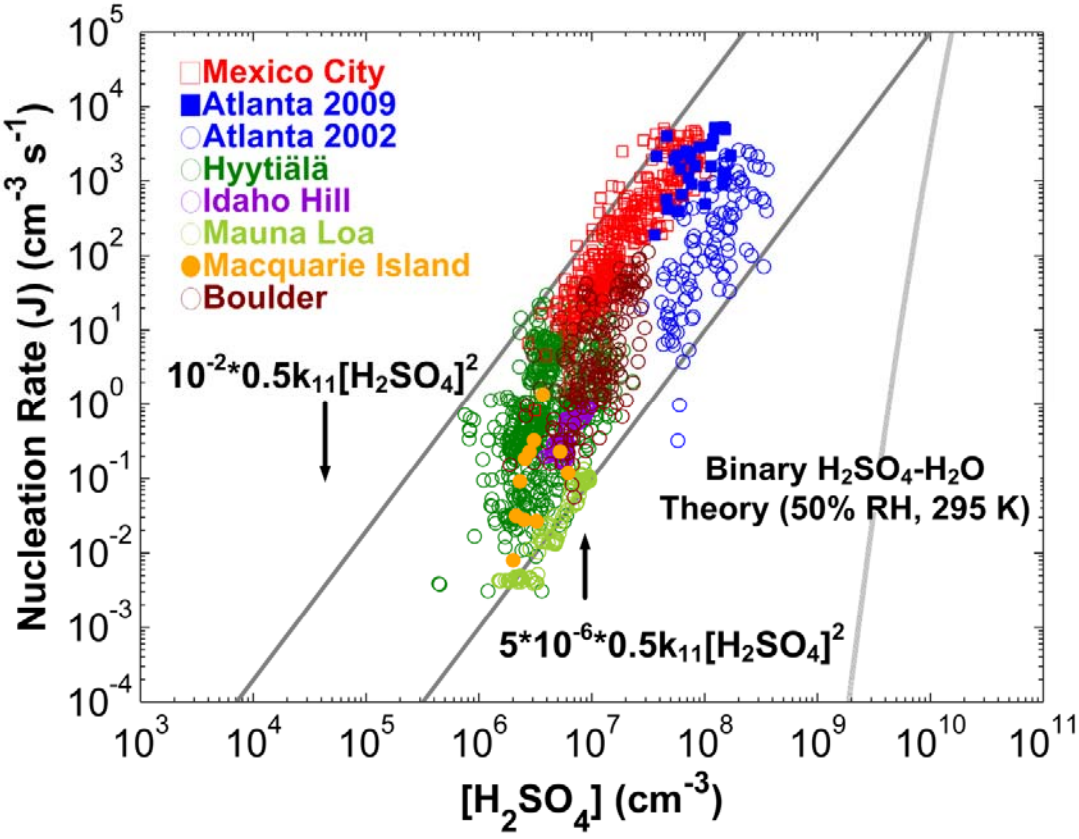

Figure 5.1 Dependence of nucleation rates ($J = J_{1\ nm}$) in the atmospheric boundary layer on $[H_2SO_4]$. The solid diagonal lines, which provide bounds for atmospheric observations, show that nucleation rates range from 10^{-2} to 5×10^{-6} times the sulfuric acid vapor collision rate.

Mechanisms, including classical binary homogeneous nucleation (BHN – H_2O/H_2SO_4) (Doyle 1961, Vehkamaki et al. 2002) and classical ternary homogeneous nucleation (THN - $H_2O/H_2SO_4/NH_3$) (Merikanto et al. 2007), have been proposed to explain and predict the production of freshly nucleated atmospheric particles. In classical multi-component homogeneous nucleation, the rate of nucleation of stable clusters can be described generally by

(1) $$J = C\exp(-\frac{\Delta G^*}{kT})$$

where C is a kinetic pre-factor and ΔG^* is the Gibbs free energy change to form a critical cluster from a multi-component vapor (Korhonen et al. 1999). For the multi-component system described here, ΔG^* would be defined in a multi-component free energy space. Multi-component classical nucleation models have been used widely by atmospheric modelers to predict the impact of nucleation on indirect and direct climatic effects of aerosols (Merikanto et al. 2009, Pierce and Adams 2009, Wang and Penner 2009, Spracklen et al. 2010, Zhang et al. 2010a). Both theories, however, fail to reproduce the observed rates of atmospheric nucleation as illustrated in Figure 5.1. BHN under-predicts observed nucleation rates by over 10 orders of magnitude over the range of ambient [H_2SO_4] (10^6 to 3×10^8 cm^{-3}), and predicts a stronger functional dependence of J on [H_2SO_4] compared to that of ambient observations. At reasonable values of temperature (295 K), RH, and [NH_3] (1 - 1000 ppt) corresponding to the ambient measurements in Figure 5.1, THN does not predict any nucleation at all over the range of ambient [H_2SO_4] shown. While current multi-component classical nucleation theories reasonably explain laboratory experiments, they perform poorly for ambient observations in the boundary layer, either predicting no nucleation at all, or predicting rates that underestimate observations by orders of magnitude.

A promising alternative approach, which treats cluster formation as a sequence of reactions between acidic and basic gases, has recently been described by several groups. Vehkamäki and coworkers (McGrath et al. 2012, Ortega et al. 2012) have used

computational chemistry to model the formation and growth of clusters from basic gases and sulfuric acid. Consistent with laboratory experiments (Kirkby et al. 2011, Benson et al. 2011, Yu et al. 2012, Zollner et al. 2012), this work provides evidence that both ammonia and amines enhance ternary nucleation, and that for equal concentrations the amines have the greater effect. Dawson et al. (2012) also described a simplified mechanism for nucleation of methanesulfonic acid, amines, and water that explicitly accounts for the sequence of reactions that leads to stable particle formation. This study, which includes both experimental and computational results, shows that all three reactants play a significant role in nucleation.

In this chapter, we describe a new approach for modeling atmospheric nucleation in the polluted boundary layer based on the measurement of the complete particle size distribution down to one molecule. Data from both field and laboratory chamber experiments were used to develop the model. Since this work aims to explain nucleation rates observed in the polluted boundary layer atmospheres of Atlanta and Mexico City, where estimated nucleation rates (~1-10^3 $cm^{-3} \cdot s^{-1}$) (Iida et al. 2006) were often much greater than typical ion production rates (~2-30 $cm^{-3} \cdot s^{-1}$) (Bazilevskaya et al. 2008), it focuses only on nucleation involving condensation and evaporation of neutral molecules. A semi-empirical expression for nucleation rates was derived from this work.

5.2 Experiments and instrumentation

The nucleation model is based on measurements from Atlanta (2009) (Jiang et al. 2011c), and chamber studies carried out in University of Minnesota (2010) (Titcombe 2012). Data used to support the model includes concentrations of neutral molecular clusters containing 2, 3, and 4 sulfuric acid molecules, particle number distributions down to about 1 nm geometric diameter, and precursor gas concentrations (sulfuric acid vapor, amines and ammonia). Clusters and sulfuric acid vapor were measured with the Cluster Chemical Ionization Mass Spectrometer (Cluster CIMS) (Eisele and Tanner 1993, Chen et al. 2012, Zhao et al. 2010). Data from two Cluster CIMS instruments were used in this study. The NCAR Cluster CIMS, described by Zhao et al. (2010), operated at a higher sampling rate (0.21 lpm) and was designed for field observations. The University of Minnesota Cluster CIMS (0.083 lpm) was designed for chamber experiments and had a lower sensitivity (Titcombe 2012). A scanning mobility particle spectrometer (SMPS) (Wang and Flagan 1990) operated with a diethylene glycol condensation particle counter (DEG CPC) (Iida et al. 2009) allowed measurements of aerosol number distributions down to 1 nm (Jiang et al. 2011b). This system was referred to as the DEG SMPS. Jiang et al. (2011c) showed that number distributions measured in Atlanta by the DEG SMPS and the Cluster CIMS were in reasonable agreement (typically a factor of 2-5) in the ~1 nm size range where they overlap. As was shown in Chapter 4, similar results were found in the chamber experiments. For the chamber experiments and in Atlanta (NCCN, 2009), the ambient pressure proton transfer mass spectrometry (AmPMS)

(Hanson et al. 2011a) was used for amines. A quantum cascade laser (QCL) infrared absorption spectrometer was used for ammonia during the Mexico City 2006 intensive. The citric acid denuder difference method utilizing chemiluminescence detection was used for ammonia during measurements in Atlanta (Saylor et al. 2010). It is likely that other trace gases contribute to particle nucleation and growth, and they will also need to be measured to allow these processes to be fully understood. (Further details about the particle instruments can be found in Chapter 3. New information about the Cluster CIMS can be found in the supporting information of Chen et al. (2012).)

While Cluster CIMS measurements provide insights into nucleation processes, this information is incomplete and involves uncertainties that are difficult to quantify. Evidence suggests that the most highly neutralized clusters do not undergo chemical ionization by the nitrate ion and are therefore invisible to the Cluster CIMS. Furthermore, following chemical ionization clusters undergo chemical alterations that mask their true chemical identity. These uncertainties and limitations place constraints on information that we have been able to obtain regarding the chemical processes responsible for nucleation. Nevertheless, the data provide clues about those processes that we have exploited in this work.

5.3 Model development

The terms “monomer (A_1)”, “dimer (A_2)”, “trimer (A_3)”, and “tetramer (A_4)” used in this chapter refer to clusters that contain, respectively, one, two, three, and four sulfuric acid molecules. These clusters may also contain some water and alkaline species before ionization and sampling. However, during the process of chemical ionization and sampling, dissociation occurs and leads to the loss of water and alkaline ligands (Hanson and Eisele 2002). We assume that A_1, A_2, A_3, and A_4 correspond respectively to the species detected at masses 160, 195, 293, and 391 by the Cluster CIMS after ionization and background correction (Chen et al. 2012). These masses correspond to $HSO_4^- HNO_3$, $HSO_4^- H_2SO_4$, $HSO_4^-(H_2SO_4)_2$, and $HSO_4^-(H_2SO_4)_3$.

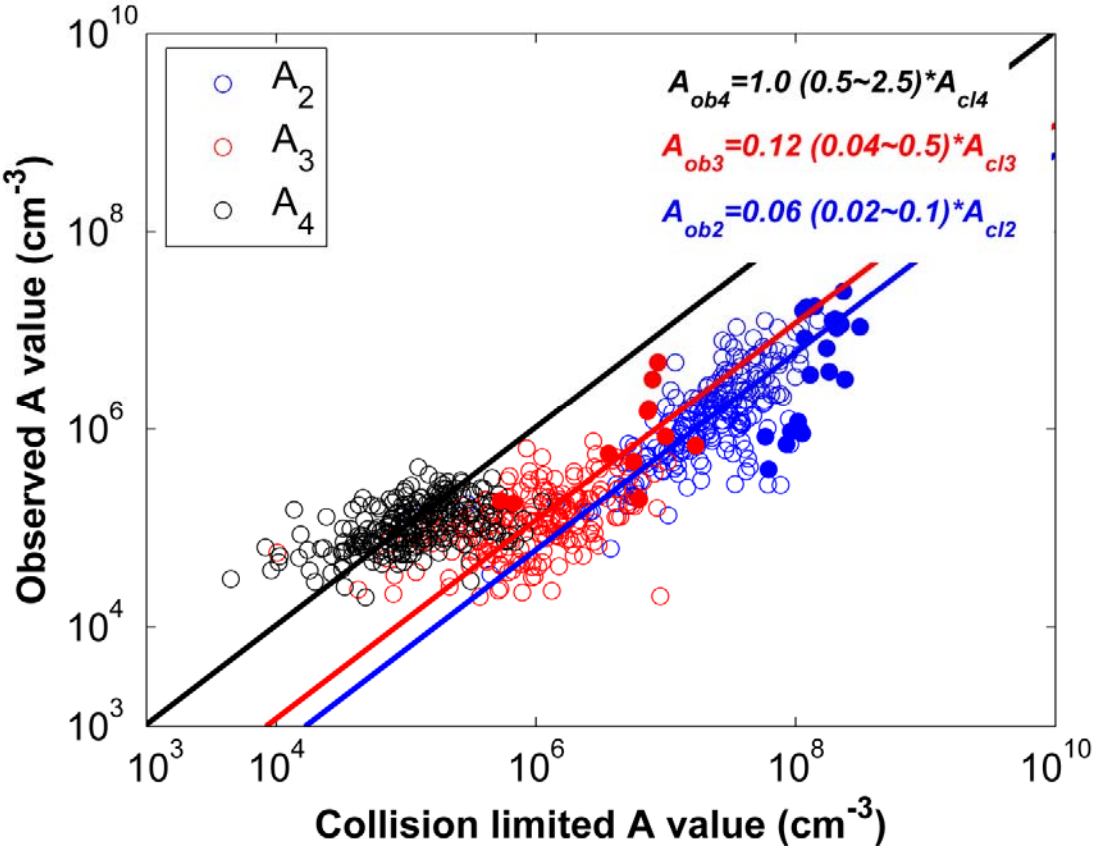

Figure 5.2 Observed dimer, trimer, and tetramer concentrations versus collision-limited values. Data obtained during 2009 field observations in Atlanta are shown with open symbols, and solid symbols are used for results from laboratory chamber experiments. Tetramer was below the detection limit in the chamber. The diagonal lines are best log–log fits with fit parameter ranges in parentheses.

Figure 5.2 plots concentrations of dimer, trimer, and tetramer measured with the Cluster CIMS versus values calculated assuming that clusters are formed at the collision-limited rates. For example, the collision-limited tetramer concentration equals the steady-state tetramer concentration that would occur if measured monomer and trimer were to react at the collision rate and evaporation did not occur (McMurry 1980). The steady state values

of collision-limited concentrations of dimer, trimer, and tetramer can be calculated by equations (2) – (4).

$$(2)\ [A_2] = \frac{k_{11} \cdot [A_1] \cdot [A_1]}{\kappa''_2}$$

$$(3)\ [A_3] = \frac{k_{21} \cdot [A_1] \cdot [A_2]}{\kappa''_3}$$

$$(4)\ [A_4] = \frac{k_{31} \cdot [A_1] \cdot [A_3] + 0.5 \cdot k_{22} \cdot [A_2] \cdot [A_2]}{\kappa''_4}$$

$$(5)\ \kappa''_i = \sum_{j=1}^{\infty} k_{ji} \cdot [A_j] \approx k_{i1} \cdot [A_1] + \frac{\bar{c}}{4} A_{Fuchs}$$

In these equations, k_{ij} is coagulation frequency function between clusters containing i and j sulfuric acid molecules (Seinfeld and Pandis 2006), and κ''_i stands for all the terms that will lead to decrease of the concentration of A_i due to coagulation (i.e., the collisional losses of A_i with sulfuric acid vapor or particles of all sizes).

Figure 5.2 shows that observed sulfuric acid tetramer concentrations are approximately equal to the collision-limited values, while dimer and trimer concentrations during both field and laboratory studies are significantly lower than the collision limited values (6% and 12% respectively). These results suggest that the evaporation of sulfuric acid from dimer and trimer are the bottlenecks to atmospheric nucleation for these studies.

Figure 5.3 shows that the concentration ratio of steady-state dimer to monomer ($[A_2]/[A_1]$) in the chamber experiments increases as total amine concentrations (protonated m/z 32+46+60+74+88) increase. Note that in the chamber, ammonia concentration is only about 1% of the amine concentration. Therefore, the stabilization effect of ammonia is not considered for the chamber data. The observed increase in dimer concentrations is due to stabilization of dimer by the base (Ortega et al. 2012). In order to describe this effect, two types of dimer are introduced to the model. More volatile (MV) dimer, A_{2MV}, is formed when two monomers collide with each other. Since "monomer", as defined in this section, may contain alkaline species, MV dimer is not necessarily pure sulfuric acid dimer. Nevertheless, A_{2MV} is unstable to some extent, and evaporates with a first order rate constant of E_{2MV}. In the presence of basic gaseous compounds such as amines, the more volatile dimer A_{2MV} will be converted into less volatile (LV) dimer A_{2LV}. The overall concentration of dimer (m/z 195) corresponds to the total concentration of A_{2MV} and A_{2LV}. Thus, when the concentrations of amines increase, more A_{2MV} will converted to A_{2LV}, which makes the A_2 species more stable and results a higher ratio of $[A_2]/[A_1]$.

This process can be described by the following equations. The MV dimer is assumed to be in equilibrium with the monomer:

(6) $A_1 + A_1 \underset{E_{2MV}}{\overset{k_{11}}{\rightleftharpoons}} A_{2MV}$

Once formed, the MV dimer reacts with amine at the collision rate k'_{21} to form A_{2LV}:

(7) $A_{2MV} + B \xrightarrow{k_{21}^{'}} A_{2LV}$

where B is the concentration of amines. The concentration of the MV dimer is then described by the following rate equation:

(8) $$\frac{d[A_{2MV}]}{dt} = \frac{1}{2} k_{11} \cdot [A_1] \cdot [A_1] - E_{2MV} \cdot [A_{2MV}] - k_{21}^{'} \cdot [A_{2MV}] \cdot [B] - [A_{2MV}] \cdot \kappa_2^{'}$$

where κ_2' is the first-order loss rate of A_{2MV} to larger clusters and particles, which is assumed to be collision limited and is evaluated from measured size distributions using the following expression:

(9) $$\kappa_2^{'} = \kappa_2 - k_{21} \cdot [A_1]$$

(10) $$\kappa_2 = k_{21} \cdot [A_1] + k_{22}^{'} \cdot [A_{2MV}] + k_{22} \cdot [A_{2LV}] + \sum_{i=3}^{\infty} k_{2i} \cdot [A_i] \approx k_{21} \cdot [A_1] + \frac{\bar{c}}{4} A_{Fuchs}$$

The steady state concentration of A_{2MV} is then,

(11) $$[A_{2MV}] = \frac{1}{E_{2MV} + k_{21}^{'} \cdot [B] + \kappa_2^{'}} \cdot \frac{1}{2} k_{11} \cdot [A_1] \cdot [A_1]$$

Assuming that A_{2LV}, is nonvolatile, its concentration is governed by:

(12) $$\frac{d[A_{2LV}]}{dt} = k_{21}^{'} \cdot [A_{2MV}] \cdot [B] - [A_{2LV}] \cdot \kappa_2 + E_3 \cdot [A_3]$$

Under typical conditions, $E_3 \cdot [A_3] \ll k_{21}^{'} \cdot [A_{2MV}] \cdot [B]$, so the steady-state concentration of A_{2LV} can be approximated as,

(13) $$[A_{2LV}] \approx \frac{k_{21}^{'} \cdot [B]}{\kappa_2} \cdot [A_{2MV}] = \frac{k_{21}^{'} \cdot [B]}{\kappa_2} \cdot \frac{1}{E_{2MV} + k_{21}^{'} \cdot [B] + \kappa_2^{'}} \cdot \frac{1}{2} k_{11} \cdot [A_1] \cdot [A_1]$$

Because the Cluster CIMS detects both A_{2MV} and A_{2LV}, at m/z=195 (i.e., because the amines are lost following chemical ionization), the observed dimer concentration is then:

(14) $$[A_2] = [A_{2MV}] + [A_{2LV}] \approx [A_{2LV}] = \frac{k_{21}^{'} \cdot [B]}{\kappa_2} \cdot \frac{1}{E_{2MV} + k_{21}^{'} \cdot [B] + \kappa_2^{'}} \cdot \frac{1}{2} k_{11} \cdot [A_1] \cdot [A_1]$$

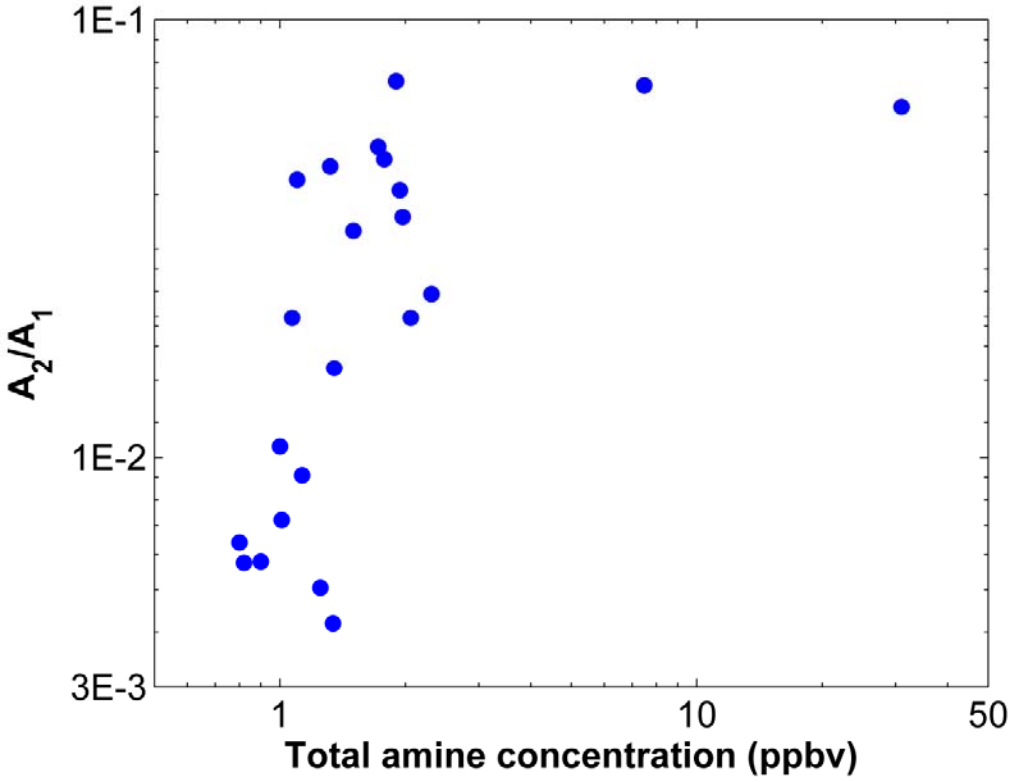

Figure 5.3 Ratio of steady-state dimer to monomer concentrations (m/z 195/160) as a function of total amine concentration in chamber experiments.

The coefficient E_{2MV} was determined by fitting equation (14) to the observed dimer concentration. Figure 5.4 compares measured dimer concentrations with values calculated from Eq. 14 using the best fit E_{2MV} value of 400 s^{-1} (range from 100 – 1000 s^{-1}). Different from the chamber experiments, in which amines are the dominant basic species, ammonia concentrations in Atlanta were about 100 times higher than amines. If it is assumed that amines are the only basic species that stabilize dimer in Atlanta, then concentrations of dimer predicted by the model with E_{2MV} = 400 s^{-1} are about an order of magnitude below the concentrations of A_2 that were observed (green symbols in Figure

5.4). However, when ammonia is assumed to have the same effect in stabilizing sulfuric acid cluster as does amine (i.e. *B*=[ammonia]+[amine]), modeled results agree with observations in Atlanta (red symbols in Figure 5.4).

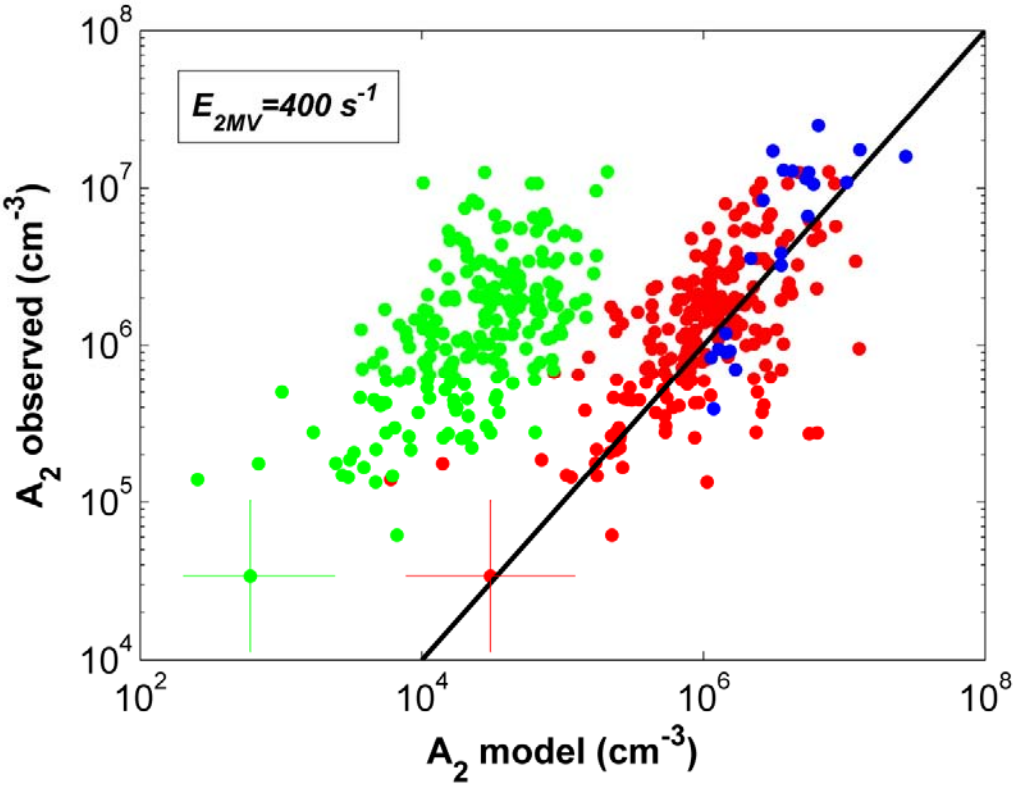

Figure 5.4 Comparison of measured (vertical axes) and modeled (horizontal axes) concentrations of dimer. Symbols shown in blue are from the chamber experiments. Other data (red, green) are from Atlanta (2009). For the red symbols, it was assumed that [B] = ammonia + amines, whereas for the green symbols [B] = total amines; ammonia concentrations were about 10 times higher than total amines. The crosses, centered on randomly selected data points, apply to all data points and show estimated uncertainties in measured and modeled cluster concentrations.

A similar method can be used to determine the evaporation coefficient of trimer. The population balance for trimer, assuming its evaporation coefficient is E_3, can be described by equation (15). Because our measurements provide no explicit evidence for different types of trimer (e.g., MV and LV), we assume as an approximation that all trimer are equally volatile.

$$(15)\ \frac{d[A_3]}{dt} = k_{21} \cdot [A_1] \cdot [A_{2LV}] - [A_3] \cdot \kappa_3 - E_3 \cdot [A_3]$$

$$(16)\ \kappa_3 \approx k_{31} \cdot [A_1] + \frac{\bar{c}}{4} A_{Fuchs}$$

The steady state concentration of trimer is then,

$$(17)\ [A_3] = \frac{k_{21} \cdot [A_1] \cdot [A_{2LV}]}{\kappa_3 + E_3}$$

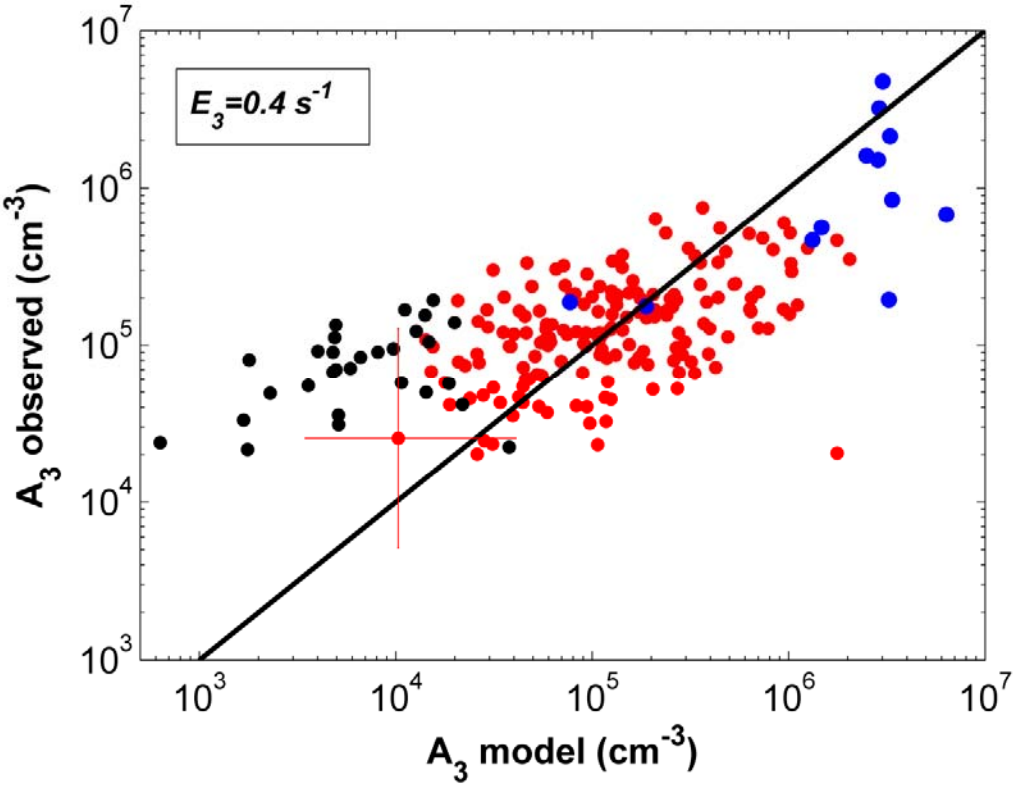

Figure 5.5 Comparison of measured (vertical axes) and modeled (horizontal axes) concentrations of trimer. Symbols shown in blue are from the chamber experiments. Other data (red and black symbols) are from Atlanta (2009). The black symbols were obtained when monomer concentrations were below 3×10^7 cm^{-3}. The 1:1 correlations are indicated by the diagonal black line. The cross, centered on a randomly selected data point, applies to all data points and shows estimated uncertainties in measured and modeled cluster concentrations.

Figure 5.5 compares the modeled and observed trimer concentration with the best fit E_3 of 0.4 s^{-1} (range from 0.1 to 0.7 s^{-1}). The data shown in black in Figure 5.5 were all measured when monomer concentrations were below 3×10^7 molecules cm^{-3}. Those data were not used when evaluating E_3 because of the possibility that the higher relative

contributions of background led to overestimates of cluster concentrations (Jokinen et al. 2012). Including those results would not have led to a significant difference in the value of E_3.

Several studies have been carried out previously in order to quantify the evaporation rate of sulfuric acid clusters. Hanson and Lovejoy (2006) measured equilibrium constants for sulfuric acid monomer and dimer at low temperatures. An evaporation rate constant of E2 = 1×10^5 s^{-1} is obtained by extrapolating their data to 300 K. Ortega et al. (2012) found E2 = 1.5×10^4 s^{-1} using quantum chemical computations. Both of these values are significantly greater that our empirically determined value of E_{2MV} = 400 s^{-1}. However, E_{2MV} exceeds computed values of sulfuric acid evaporation rates from dimer that contain 1, 2, 3 or 4 molecules of dimethyl amine (2.45 x 10^{-5} s^{-1}, 5.88 x 10^{-17} s^{-1}, 3.41 x 10^{-18} s^{-1}, 4.27 x 10^{-20} s^{-1}, respectively) (Ortega et al. 2012). Therefore, E_{2MV} is an overall effective evaporation rate that is not unreasonable, given the wide range of evaporation rates from dimer that have been reported previously. Similarly, $E_3 = 0.4 \pm 0.3$ s^{-1} is significantly less than the value of 2.0 x 10^5 s^{-1} obtained from quantum calculations for pure sulfuric acid trimer, but is within range of values of sulfuric acid evaporation rates from trimer that contain 1, 2, 3 or 4 molecules of dimethyl amine (3.7 s^{-1}, 90.8 s^{-1}, 1.44 x 10^{-10} s^{-1}, 7.17 x 10^{-15} s^{-1}, respectively) (Ortega et al. 2012).

Since the Cluster CIMS data (as shown in Figure 5.2) suggest that evaporation does not occur for tetramer or larger clusters, we define the nucleation rate as the rate at which tetramer is produced:

$$
\begin{aligned}
J_4 &= k_{31} \cdot [A_1] \cdot [A_3] \\
&= \left\{ \frac{k'_{21} \cdot [B]}{E_{2MV} + k'_{21} \cdot [B] + \kappa'_2} \cdot \frac{k_{21} \cdot [A_1]}{\kappa_2} \cdot \frac{k_{31} \cdot [A_1]}{\kappa_3 + E_3} \right\} \cdot \frac{1}{2} k_{11} \cdot [A_1] \cdot [A_1] \\
&= P \cdot \frac{1}{2} k_{11} \cdot A_1 \cdot A_1
\end{aligned}
\tag{18}
$$

where the prefactor P is less than 1. For very high monomer concentrations ($[A_1] > 10^9$ cm^{-3}), P is insensitive to $[A_1]$ because $k_{21}[A_1]$ and $k_{31}[A_1]$ dominate the values of κ_2 and κ_3. At low monomer concentrations, P increases with $[A_1]$.

The complete reaction pathway described in this model is illustrated in Figure 5.6. Monomers collide with each other and form unstable MV type dimer, which evaporates at a rate of 400 s^{-1}. Basic gases including ammonia and amines stabilize MV dimers, converting them into LV dimers. Trimer, with evaporation coefficient of 0.4 s^{-1}, is formed through collision between monomer and dimer. When basic gas concentrations are higher than 1×10^6 (basic gas concentrations in Mexico City and Atlanta are much higher in most cases during nucleation events), the steady state concentration of MV dimer is orders of magnitude smaller than LV dimer. Thus the formation of trimer can be approximated as a process between only monomer and LV dimer. Sulfuric acid clusters of tetramer and larger are stable. Thus the nucleation rate equals the formation rate of

tetramer (equation 18). Predicted nucleation rates from this model depend on concentrations of sulfuric acid, basic gases, and pre-existing aerosols.

The fact that the formation of tetramer is collision limited also agrees with the previous work on growth rates for particles in the 1 nm size range as described in Chapter 3 and by Kuang et al. (Kuang et al. 2012b), who showed that sulfuric acid monomer uptake is approximately collision controlled for particles as small as 1 nm. A spherical 1-nm ammonium sulfate particle (density assumed equal to bulk density, 1769 kg/m^3), would contain about four ammonium sulfate molecules, so this result supports the argument that monomer uptake by tetramer could be collision controlled. A detailed discussion of growth rates for particles in the 1 nm size range for measurements carried out in Atlanta is also found in Chapter 3.

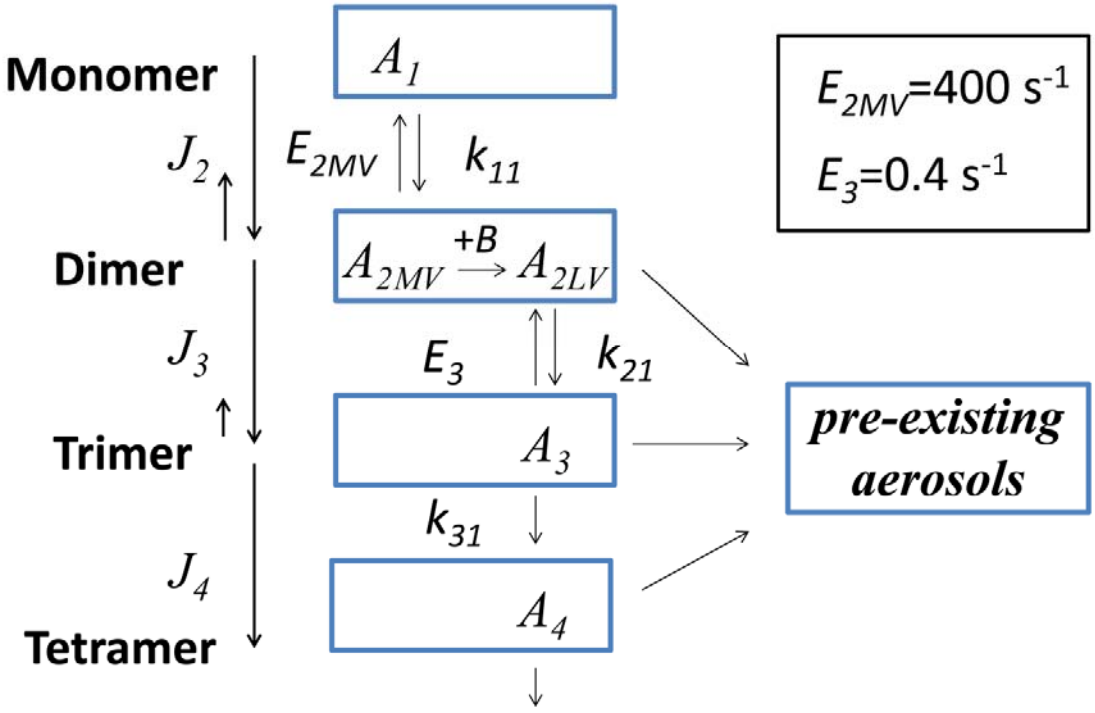

Figure 5.6 Conceptual acid–base reaction model for nucleation. Measured monomer concentrations are an input to the model and are determined by chemical-formation and condensation-loss rates. Rows represent the number of sulfuric acid molecules per cluster. Dimer (row 2) includes MV and LV clusters. Trimer includes a single type of cluster that is volatile to some extent. Clusters larger than trimer are not volatile.

5.4 Comparison of observed and predicted nucleation rates

Figure 5.7 compares the modeled nucleation rates with observed rates in Mexico City and Atlanta. The methods of estimating the observed nucleation rates can be found in the work of Kuang and coworkers (Kuang 2009, Kuang et al. 2012b). (A brief description of

the methods is summarized in the appendix.) For Mexico City, model predictions mostly agree with the observed values to within a factor of 10. Modeled and measured nucleation rates for Atlanta are also within a factor of 10 for all but 5 of the 31 measurements. However, the model predicts a greater variability in nucleation rates than was observed in Atlanta, with modeled rates exceeding measurements by up to a factor of 100. Measurements that were carried out on August 22, 2009, are circled. Those measurements account for most of the days where modeled nucleation rates were high. The available data do not explain the reasons for the discrepancy. However, the measured and modeled nucleation rates for August 22 can be reconciled if evaporation of sulfuric acid from the tetramer is included in the model, using evaporation rate constants of E_{2MV} = 400 s^{-1}, E_3 = 1 s^{-1}, and E_4 = 0.3 s^{-1} (Figure 5.8). This result suggests that on August 22, concentrations of an important stabilizing compound were lower than for other days. This result also implies that in cleaner environments, where concentrations of stabilizing compounds are lower than in Atlanta or Mexico City, it might be necessary to alter the model to include evaporation from clusters larger than trimer. This would lead to the inclusion of additional terms in the prefactor P, similar to those for dimer and trimer evaporation shown above.

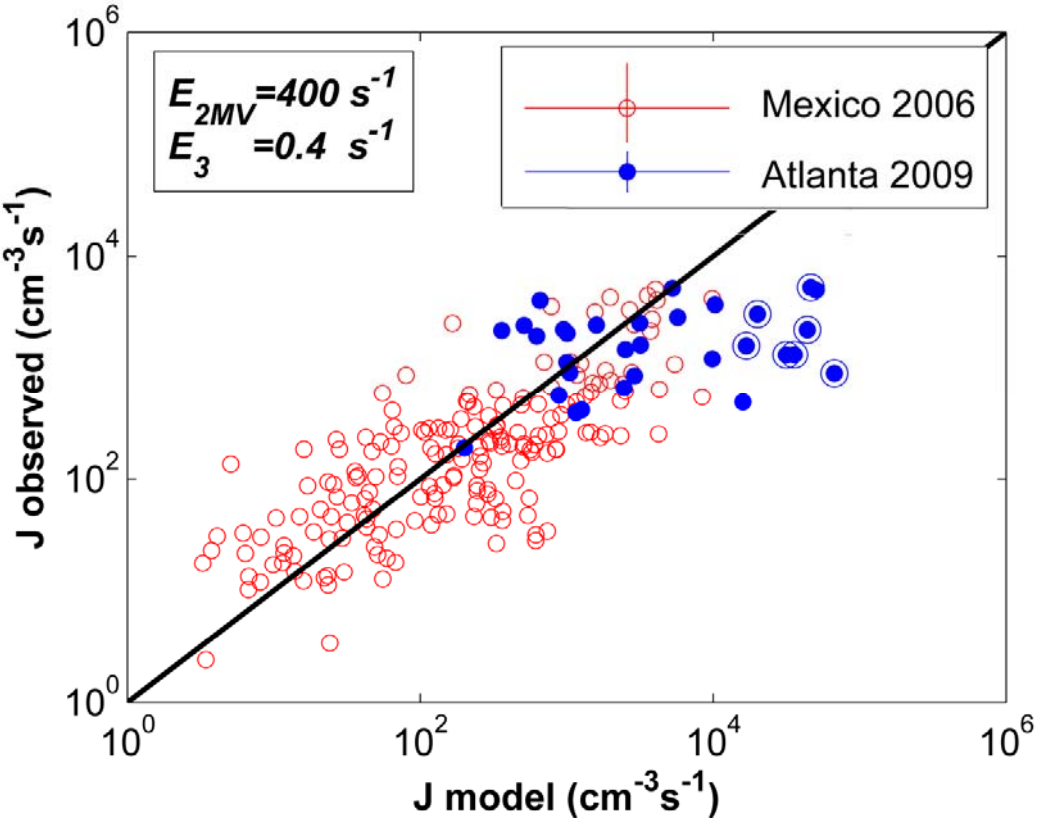

Figure 5.7 Comparison of observed and calculated (Eq. 18) atmospheric nucleation rates. The red symbols are from Mexico City (2006). The blue symbols are from Atlanta (2009). The 1:1 correlation is indicated by the diagonal black line. The error bars shown in the legend apply to all data points. The seven circled blue symbols are from measurements on August 22, 2009.

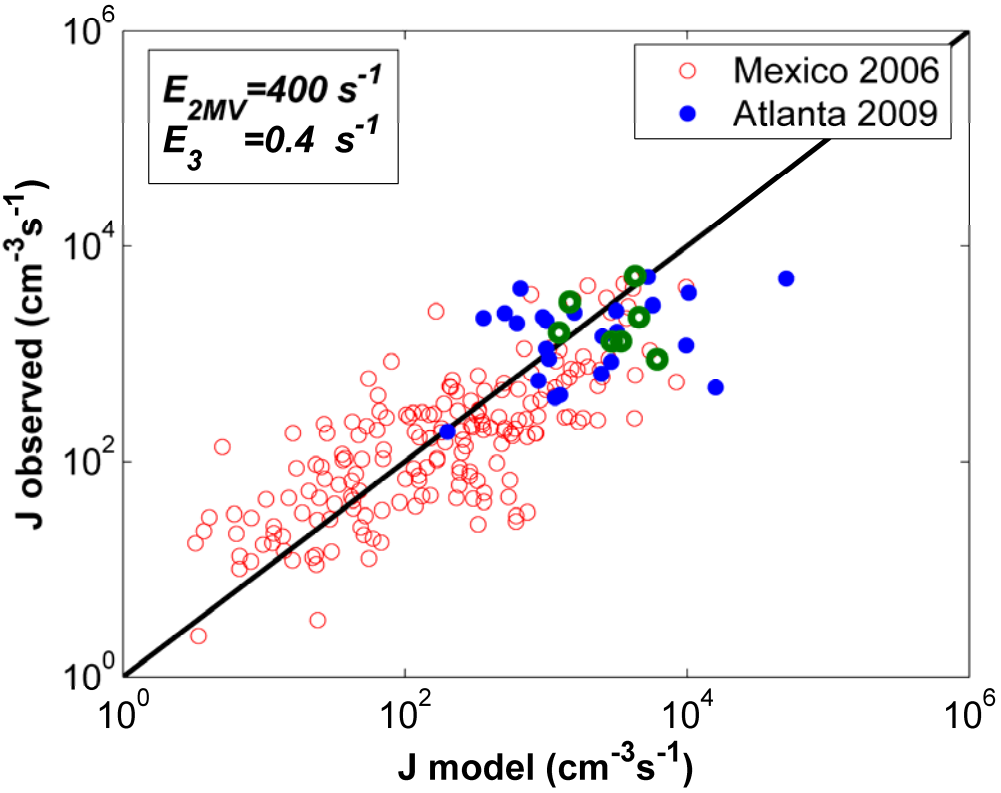

Figure 5.8 Comparison of observed and calculated (Eq. 18) atmospheric nucleation rates. The seven green symbols are from measurements on August 22, 2009. Evaporation coefficients of $E_{2MV} = 400\ s^{-1}$, $E_3 = 1\ s^{-1}$, and $E_4 = 0.3\ s^{-1}$ are used to calculated J_{model} for these data points. The remaining data points are the same as shown in Figure 5.7.

5.5 Summary

A new conceptual model for atmospheric nucleation is proposed. This model is based on new measurements of neutral molecular clusters carried out in laboratory chamber experiments and in the urban Atlanta atmosphere. The process of nucleation is described

as a series of chemical reactions between sulfuric acid containing clusters and basic gaseous compounds. Evaporation rates of the unstable clusters are determined by fitting steady state expression of cluster concentration to neutral clusters concentrations obtained by the Cluster CIMS. This model predicts nucleation rates observed in Mexico City and Atlanta to within a factor of 10. This is a significant improvement over classical theory models, which differ from measurements by factors of 10^{10} or more. This model also shows that basic gaseous compounds play an important role in stabilizing clusters in the atmosphere.

Uncertainties in this model largely come from determining the evaporation coefficients with the data. Uncertainties that affect measurements of clusters include the unknown dependence of chemical ionization on cluster composition, changes in chemical composition following chemical ionization, and breakup of clusters following sampling into the low pressure region of the mass spectrometer. In addition, the relationship between ion concentrations at the inlet to the mass spectrometer and the signal from the mass spectrometer are only approximately known. A detailed discussion of the uncertainty in Cluster CIMS measurement and the correction for background noise and ion induced nucleation can be found in the supporting information of Chen et al. (2012). For the nanoparticle size distributions, uncertainties include dependencies of charging rates and condensational activation on particle composition. It is encouraging that for the size range where they overlap, measurements of number distributions obtained with the independently calibrated Cluster CIMS and the DEG SMPS are in "reasonable"

agreement (usually within a factor of 2 to 5). Though this model explicitly accounts for the roles of amines and ammonia on nucleation, the fact that the data from August 22 in Atlanta deviates from the model prediction indicates that there may be other chemical species also playing important roles in this process. A more complete understanding of chemical processes that affect nucleation rates will require more detailed investigations on the chemical kinetics of reactions between molecular clusters and various basic gaseous compounds (and mixtures thereof). The development of improved instrumentation, which would enable more accurate and complete measurements of cluster composition, would also be beneficial.

5.6 Supporting information

S 5.6.1 Methods of calculating "observed nucleation rates"

In a system where particle sizes are changing as a result of vapor uptake, the particle flux past any size can in general be expressed as:

$$\text{(S1)}\quad J_{D_p} = \left.\frac{\partial N}{\partial D_p}\right|_{D_p} \cdot \left.\frac{dD_p}{dt}\right|_{D_p}$$

where the first term on the right hand side is the particle number distribution and the second term is the net particle diameter growth rate. We define the nucleation rate as equal to the tetramer formation rate, since our measurements imply that sulfuric acid does not evaporate from tetramer at a significant rate. Since tetrameter is approximately 1 nm in diameter, the nucleation rate, *J*, can therefore be expressed as:

$$\text{(S2)}\quad J = J_{1nm} = \left.\frac{\partial N}{\partial D_p}\right|_{1nm} \cdot \left.\frac{dD_p}{dt}\right|_{1nm}$$

With the complete particle size distribution as in Atlanta 2009, both terms can be calculated (see Chapter 3). Thus, "observed nucleation rate" from Atlanta 2009 in Figure 5.7 is estimated directly from equation (S2).

In Mexico City, the smallest particles detected were about 3 nm. (The DEG SMPS had not been developed when this study was carried out.) Therefore, the nucleation rate at 1 nm was approximated by extrapolation from the particle formation rate at 3 nm (J_{3nm}). Assuming steady state size distributions between 1 nm and 3 nm and incorporating the probability that a particle would grow from 1 nm to 3 nm by vapor condensation before being scavenged by large existing particles, the relationship between J_{3nm} and J_{1nm} is (Weber et al. 1997):

$$\text{(S3)} \quad J_{1nm}(t) = J_{3nm}(t+\Delta t)\cdot \exp[\frac{1}{2}\cdot\frac{A_{Fuchs}}{GR_{1-3}}\cdot\sqrt{\frac{48k_BT}{\pi^2\rho}}\cdot(\frac{1}{1nm}-\frac{1}{3nm})]$$

where A_{Fuchs} is the surface area of the existing large particles, k_B is the Boltzmann constant, T is the temperature and Δt is the time it takes for 1 nm particle to grow to 3 nm, and the exponential term is the probability that a 1 nm particle will grow to 3 nm before it is lost by coagulation with large pre-existing particles.

The nucleation rate at 3 nm, J_{3nm}, can be approximated as described by Weber et al. (1996):

(S4) $$J_{3nm} \approx \frac{\Delta N_{3-6}}{\Delta D_p} \cdot GR_{1-3}$$

where $\Delta N_{3\text{-}6}$ is the measured concentration of particles in the 3 to 6 nm diameter range, ΔD_p is 6 nm-3 nm=3 nm, and $GR_{1\text{-}3}$ is the average growth rate of particles in the 1-3 nm range. $GR_{1\text{-}3}$ can be estimated from the time delay between the observed rise in the concentration of sulfuric acid and the observed rise in concentration of particles equal to and larger than 3 nm (Weber et al. 1997, Sihto et al. 2006).

Nucleation rates calculated as outlined above are based on particle size distributions and time delays, and are independent from the nucleation rates predicted from the model derived in this chapter.

Chapter 6: Future Work

Recent developments in aerosol instrumentation have led to significant advancements in our understanding of atmospheric nucleation. Condensation particle counters that use diethylene glycol as the condensing vapor (DEG CPCs) have lowered the particle detection limit to about 1 nm (Iida et al. 2009, Jiang et al. 2011b, Vanhanen et al. 2011). Newly developed chemical ionization mass spectrometers (Zhao et al. 2011, Jokinen et al. 2012) are able to detect neutral clusters containing two, three or four sulfuric acid molecules with high resolution and sensitivity. Some examples of measurements made by these instruments are discussed in previous chapters. These important measurements enabled direct measurements of the earliest stages of particle formation from neutral gaseous precursors, from which a semi-empirical nucleation model was developed. Nevertheless, major uncertainties remain that limit our ability to quantify the chemical processes responsible for nucleation. To reduce these uncertainties and deepen the understanding of the atmospheric nucleation mechanism, additional research is needed. I identified three problems regarding the uncertainties that I consider to be most significant, in the areas of both measurement and model development. They include: (1) CPC

detection efficiencies for atmospheric particles; (2) charging mechanism for particles around 1 nm; and (3) validation and further development of the nucleation model.

6.1 Detection efficiency of atmospheric particles

As was shown in Chapter 2, modern condensation particle counters (CPCs) can detect particles down to 1 nm. Nevertheless, detection efficiencies for particles smaller than 3 nm are highly sensitive to particle composition. Figure 6.1 shows detection efficiencies for silver and sodium chloride particles with the University of Minnesota diethylene glycol CPC (UMN DEG CPC) in the size range between 1 and 3 nm. The difference in detection efficiencies increases rapidly when particle diameter decreases. At 1.5 nm, the detection efficiency of sodium chloride particles is about 25%, while it's very close to 0 for silver particles.

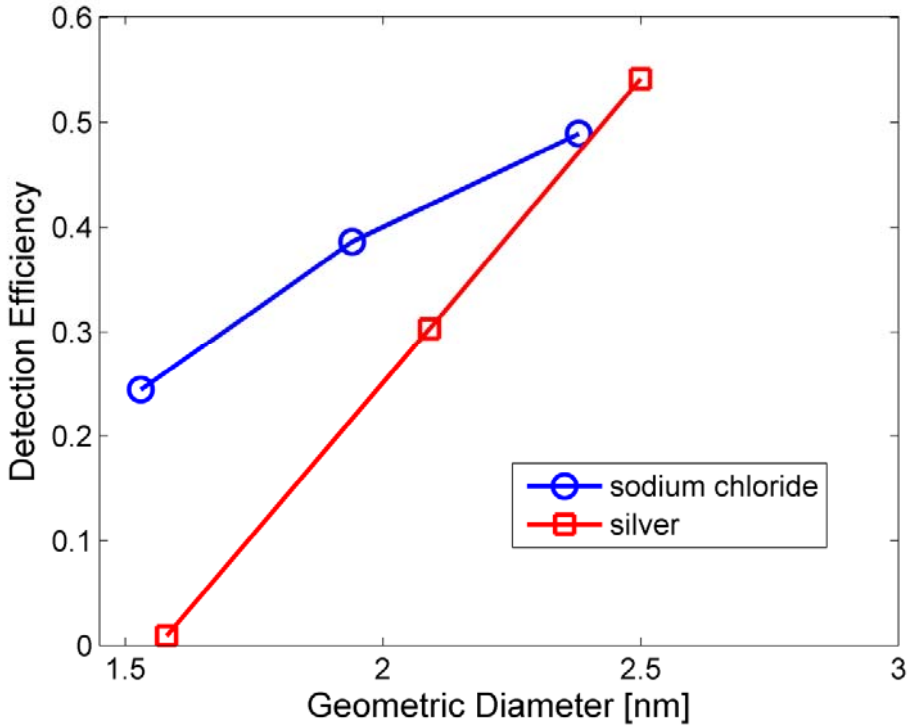

Figure 6.1 Detection efficiency of UMN DEG of negative sodium chloride and silver particles with 1 to 3 nm size range.

Studies of CPC performance for particles with different compositions have been reported. However, detection efficiencies of actual freshly nucleated atmospheric particles have never been measured. We have assumed that sub-3 nm atmospheric particles are detected with the same efficiencies as sodium chloride particles of the same size (see Chapter 3). Recent work has shown that the formation and growth of freshly nucleated atmospheric particles are mainly due to sulfuric acid and some basic species (Kuang et al. 2012b, Chen et al. 2012) leading to the formation of inorganic salts. We hypothesized that condensation of DEG on those salts might be similar to condensation of DEG on sodium

chloride, although we have no proof of this. Laboratory studies aimed at quantifying the DEG CPC detection for particles similar in composition to freshly nucleated atmospheric particles would reduce uncertainties in inverted atmospheric size distributions.

Several methods can be used to provide a stable source for laboratory-generated sulfuric acid-containing particles. These methods include using a sulfuric acid liquid saturator (for example, see Ball et al. (1999)) or using ultra violet lights to initiate photolysis reactions and produce sulfuric acid from ozone, sulfur dioxide, and water (for example, see Kirkby et al. (2011) or Chen et al. (2012)). Once sulfuric acid particles are formed, a setup similar to that introduced in Chapter 2 (Figure 2.1) can be used for CPC calibration.

6.2 Charging mechanism for particles around 1 nm

Charging is an important process for aerosol science since it is critical for almost all electrical aerosol measurements. Several different theories of diffusion charging have been developed previously (Hidy and Brock 1970, Liu 1976, Davison and Gentry 1984). Among them, Fuchs' theory, based on calculated steady state ion fluxes towards a sphere (Fuchs 1963, Hoppel and Frick 1986), is the most widely used. Experiments aimed at verifying these theories have been carried out for particles down to 5 nm (Kousaka et al. 1983, Hussin et al. 1983, Adachi, Kousaka and Okuyama 1985, Wiedensohler and Fissan 1991). More limited studies have been done for particles larger than 2 nm (Reischl et al. 1996, Alonso et al. 1997). These experimental results can be fit to Fuchs' theory

reasonably well. Since the collision rate, instead of the charging rate, is the quantity that is explicitly calculated in Fuchs' theory, the underlying assumption is that the charge is transferred from ion clusters to particles at each collision. Recent work (Premnath, Oberreit and Hogan 2011) on charge transfer between amino acid particles and trimethylamine vapor shows that the backward charge transfer rate (from particle to ion), a function of both particle diameter and composition, can be significant for particle sizes approaching 0.5 nm. This is the size where the diffusional transport and chemical properties both can affect charging rates and, therefore, charged fractions. While transport rates can be calculated with reasonable confidence, the effects of particle chemistry are more difficult to assess, in part because the chemical makeup of the nucleated clusters is now known with certainty.

For atmospheric measurements with DEG CPCs, particles around 1 nm (the critical size for nucleation) are of particular interest. Charged fractions must be known accurately to ensure an accurate inversion from direct measurements of mobility classified number concentrations to particle size distributions. The experiment setup shown in Figure 6.2 is proposed to address this question. This will not only help us to obtain actual atmospheric particle size distribution, but will also enrich our knowledge on the charging process for particles in the 1 nm size range.

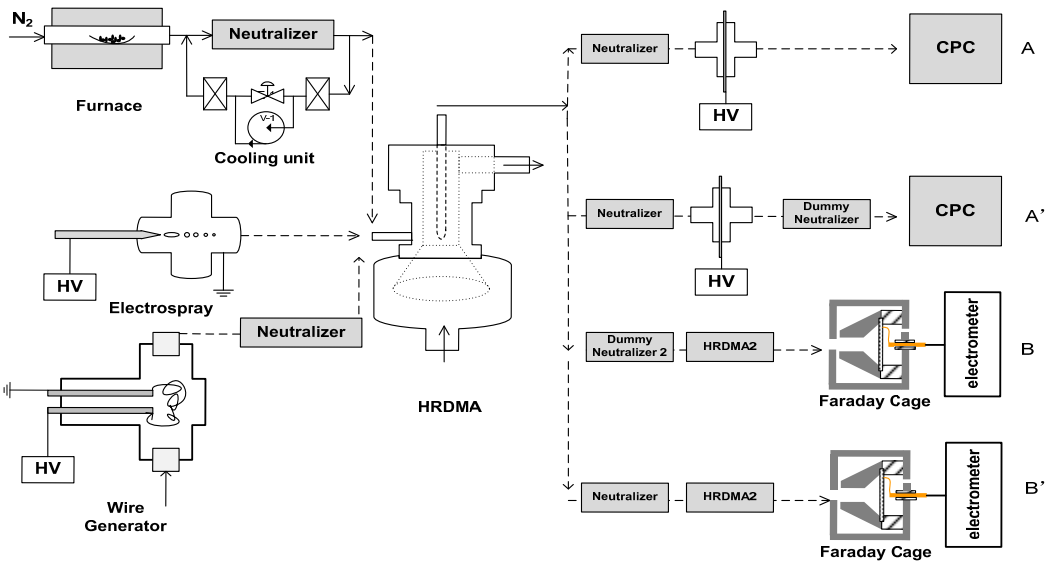

Figure 6.2 Experiment setup for charging efficiencies of particles of different composition. Dummy neutralizers are the neutralizer housing without the radiative material. Dummy neutralizer in line A' is used to measure the diffusional loss in the housing. The dummy neutralizer in line B is used to ensure the same diffusional loss as in line B'.

Particles of different compositions can be generated by various methods, such as the tube furnace, electrospray, and the wire generator shown in Figure 6.2. They can be used to generate metal and salt particles, and molecular ions (see Chapter 2). To study the atmospheric related particles, reaction chamber or flow tube (as described in section 6.1) can also used as a particle source in this setup (not shown in Figure 6.2). These particles will then be sent into the high resolution differential mobility analyzer (HRDMA), where they are classified according to their electrical mobility. After that, they will be sent to the UCPC (A and A') and the Faraday cage electrometer (FCE) (B and B').

The neutralizer in the line of FCE B' ensures all the particles coming from the first HRDMA are returned to a steady-state charge distribution. Since there is no radioactive material in the dummy neutralizer in line B, FCE B measures the total ion concentration coming out from the first HRDMA. The fraction of the charged particles then can be determined by the signal of FCE B (N_B) and signal of FCE B' ($N_{B'}$).

(1) $$\eta_{in} = \frac{N_{B'}}{N_B}$$

where η_{in} stands for the intrinsic charged fraction. The diffusion loss inside the neutralizer is not considered. Lines A and A' independently measure the diffusion loss at different flow rates. The extrinsic charging fraction, the concentration of positively or negatively charged particles coming out of the neutralizer divided by the total concentration of particles going into the neutralizer, can be estimated by Eq. (2).

(2) $$\eta_{ex}(Q) = \frac{N_{A'}(Q)}{N_A(Q)} \cdot \frac{N_{B'}}{N_B}$$

For measurements within the size range of 1 to 2 nm, there are usually two major difficulties. One is the signal strength of the electrometer. The other is the diffusion deterioration of the DMA transfer function. Particle generation needs to be optimized to ensure a stable particle source that produces high concentratons and the setup needs to be designed to minimize diffusion losses within the sampling tubing. The HRDMAs (R>30) used in this study can ensure mono-dispersed particles are obtained around 1 nm. Charged fractions will be measured as a function of particle diameter as well as particle composition. Also, by comparing measurement B with measurement B', one can check if

mass transfer occurs together with ion transfer during ion-particle collision. If it does occur, a shift of the concentration peak location versus voltage of the DMA will be observed.

6.3 Validation and further development of the nucleation model

In chapter 5, a semi-empirical nucleation model was developed based on observations in the laboratory and in the field. This model predicts nucleation rates as a function of sulfuric acid concentration, basic gas concentrations (ammonia and amines) and concentration of pre-existing particles. Nucleation rates predicted by this model are in reasonable agreement with atmospheric observations. Limited by current measurement techniques, several assumptions are made for this model. Future validation of these assumptions is necessary.

6.3.1 Effect of ammonia and amines in stabilizing sulfuric acid clusters

In our nucleation model, the sulfuric acid evaporation rate constants are assumed to be independent of the type of base that is reacting with the sulfuric acid-containing clusters. In other words, E_{2MV} and E_3 are assumed to be equal for clusters that contain ammonia and amines (see Figure 5.4 in Chapter 5). However, flow tube experiments reported by Zollner et al. (2012) showed that in a sulfuric-water system, 2 pptv ammonia enhanced

nucleation rates by a factor of 800, while 3 pptv methyl amine could enhance nucleation more than 20000 times. Qualitatively similar results were also reported by Yu et al. (2012) and Ortega et al. (2012) through laboratory experiments and simulation respectively, showing that amines are significantly more effective in enhancing nucleation rates than ammonia in controlled laboratory environments. It is likely, therefore, that cluster stability is affected by the base that reacts with sulfuric acid. We found that nucleation rates predicted by our model are equal to rates observed in Atlanta and Mexico City if it is assumed that all basic gases have the same effect. It seems quite likely that the model will need to be modified to specifically account for differing stabilizing effects of different bases. To decouple the effects of ammonia and different types of amines in a more detailed model, experiments specifically designed to investigate the stabilizing effects of different bases are needed.

6.3.2 Formation of sulfuric acid trimer and tetramer

In the current model, the effect of basic gases in forming dimer is explicitly taken into account: the more volatile type (MV) dimer is formed by monomer collisions. Less volatile (LV) dimer are formed when the MV dimer react with a basic gas. Experiments must be carried out to determine whether or not the evaporation rate constant E_{2MV} differs for different basic compounds. Furthermore, limited by the sensitivity of the current mass spectrometer, we were not able to obtain enough high quality trimer data to determine whether or not trimer includes MV and LV types. Instead, an empirical constant E_3 =

0.4 s^{-1}, which is independent of basic gas composition, applies to all trimer. Probably because the basic gas concentration is very high and does not vary over a wide range in Atlanta and Mexico City, this constant works reasonably well except for several cases (August 22, Atlanta, see Figure 5.8 in Chapter 5). A better model requires more detailed understanding of the effect of different basic gaseous compounds on trimer formation and stability.

The formation and stability of the sulfuric acid tetramer are affected by similar uncertainties. The assumption that tetramer formation is collision controlled agrees with the majority of the field data. However, the UMN chamber study (see Chapter 4) clearly indicated that tetramer formed in non-amine experiments was unstable, even though those experiments were carried out using dimethyl amine concentrations that greatly exceed concentrations of amines in "clean environment experiments". It is possible that other chemical species, besides amines and ammonia that were measured in our work, also participated in forming tetramer. If so, future work is needed to identify these species.

Bibliography

Adachi, M., Y. Kousaka & K. Okuyama (1985) Unipolar and Bipolar Diffusion Charging of Ultrafine Aerosol-Particles. *Journal of Aerosol Science,* 16**,** 109-123.

Adams, P. J. & J. H. Seinfeld (2003) Disproportionate impact of particulate emissions on global cloud condensation nuclei concentrations. *Geophys. Res. Lett.,* 30**,** 1239.

Aitken, J. A. (1911) On some nuclei of cloudy condensation. *Transactions of the Royal Society of Edinburgh,* XXXIX**,** 15-25.

Alonso, M., Y. Kousaka, T. Nomura, N. Hashimoto & T. Hashimoto (1997) Bipolar charging and neutralization of nanometer-sized aerosol particles. *Journal of Aerosol Science,* 28**,** 1479-1490.

Andreae, M. O. & D. Rosenfeld (2008) Aerosol-cloud-precipitation interactions. Part 1. The nature and sources of cloud-active aerosols. *Earth-Science Reviews,* 89**,** 13-41.

Ball, S. M., D. R. Hanson, F. L. Eisele & P. H. McMurry (1999) Laboratory studies of particle nucleation: Initial results for H2SO4, H2O, and NH3 vapors. *Journal of Geophysical Research-Atmospheres,* 104**,** 23709-23718.

Bazilevskaya, G. A., I. G. Usoskin, E. O. Fluckiger, R. G. Harrison, L. Desorgher, R. Butikofer, M. B. Krainev, V. S. Makhmutov, Y. I. Stozhkov, A. K. Svirzhevskaya, N. S. Svirzhevsky & G. A. Kovaltsov (2008) Cosmic ray induced ion production in the atmosphere. *Space Science Reviews,* 137**,** 149-173.

Benson, D. R., J. H. Yu, A. Markovich & S. H. Lee (2011) Ternary homogeneous nucleation of H(2)SO(4), NH(3), and H(2)O under conditions relevant to the lower troposphere. *Atmospheric Chemistry and Physics,* 11**,** 4755-4766.

Berndt, T., F. Stratmann, M. Sipila, J. Vanhanen, T. Petaja, J. Mikkila, A. Gruner, G. Spindler, R. L. Mauldin, J. Curtius, M. Kulmala & J. Heintzenberg (2010) Laboratory study on new particle formation from the reaction OH + SO2: influence of experimental conditions, H2O vapour, NH3 and the amine tert-butylamine on the overall process. *Atmospheric Chemistry and Physics,* 10**,** 7101-7116.

Berresheim, H., T. Elste, C. Plass-Dulmer, F. L. Eisele & D. J. Tanner (2000) Chemical ionization mass spectrometer for long-term measurements of atmospheric OH and H2SO4. *International Journal of Mass Spectrometry,* 202**,** 91-109.

Birmili, W., H. Berresheim, C. Plass-Dulmer, T. Elste, S. Gilge, A. Wiedensohler & U. Uhrner (2003) The Hohenpeissenberg aerosol formation experiment (HAFEX): a long-term study including size-resolved aerosol, H2SO4, OH, and monoterpenes measurements. *Atmospheric Chemistry and Physics,* 3**,** 361-376.

Boy, M., T. Karl, A. Turnipseed, R. L. Mauldin, E. Kosciuch, J. Greenberg, J. Rathbone, J. Smith, A. Held, K. Barsanti, B. Wehner, S. Bauer, A. Wiedensohler, B. Bonn, M. Kulmala & A. Guenther (2008) New particle formation in the front range of the colorado rocky mountains. *Atmospheric Chemistry and Physics,* 8**,** 1577-1590.

Boy, M., M. Kulmala, T. M. Ruuskanen, M. Pihlatie, A. Reissell, P. P. Aalto, P. Keronen, M. Dal Maso, H. Hellen, H. Hakola, R. Jansson, M. Hanke & F. Arnold (2005) Sulphuric acid closure and contribution to nucleation mode particle growth. *Atmospheric Chemistry and Physics,* 5**,** 863-878.

Brus, D., K. Neitola, A. P. Hyvarinen, T. Petaja, J. Vanhanen, M. Sipila, P. Paasonen, M. Kulmala & H. Lihavainen (2011) Homogenous nucleation of sulfuric acid and water at close to atmospherically relevant conditions. *Atmospheric Chemistry and Physics,* 11**,** 5277-5287.

Bzdek, B. R., D. P. Ridge & M. V. Johnston (2011) Amine reactivity with charged sulfuric acid clusters. *Atmospheric Chemistry and Physics,* 11**,** 8735-8743.

Chen, D. R., D. Y. H. Pui, D. Hummes, H. Fissan, F. R. Quant & G. J. Sem (1998) Design and evaluation of a nanometer aerosol differential mobility analyzer (Nano-DMA). *Journal of Aerosol Science,* 29**,** 497-509.

Chen, D. R. a. P., D. Y. H. (1999) A high efficiency, high throughput unipolar aerosol charger for nanoparticles. *Journal of nanoparticle research,* 1**,** 115-126.

Chen, M., M. Titcombe, J. Jiang, C. Jen, C. Kuang, M. Fischer, F. Eisele, J. Ilja Siepmann, D. R. Hanson, J. Zhao & P. McMurry (2012) Acid-base chemical reaction model for nucleation rates in the polluted atmospheric boundary layer. *Proceedings of the National Academy of Sciences of the United States of America*.

Dal Maso, M., M. Kulmala, I. Riipinen, R. Wagner, T. Hussein, P. P. Aalto & K. E. J. Lehtinen (2005) Formation and growth of fresh atmospheric aerosols: eight years of aerosol size distribution data from SMEAR II, Hyytiala, Finland. *Boreal Environment Research,* 10**,** 323-336.

Davison, S. W. & J. W. Gentry (1984) Modeling of Ion Mass Effects on the Diffusion Charging Process. *Journal of Aerosol Science,* 15**,** 262-270.

Dawson, M. L., M. E. Varner, V. Perraud, M. J. Ezell, R. B. Gerber & B. J. Finlayson-Pitts (2012) Simplified mechanism for new particle formation from methanesulfonic acid, amines, and water via experiments and ab initio calculations. *Proceedings of the National Academy of Sciences,* 109**,** 18719-18724.

Doyle, G. J. (1961) Self-Nucleation in the Sulfuric Acid-Water System. *The Journal of Chemical Physics,* 35**,** 795-799.

Eisele, F. L. & D. J. Tanner (1993) Measurement of the gas phase concentration of H_2SO_4 and methane sulfonic acid and estimates of H_2SO_4 production and loss in the atmosphere. *J. Geophys. Res.,* 98**,** 9001-9010.

Fiedler, V., M. Dal Maso, M. Boy, H. Aufmhoff, J. Hoffmann, T. Schuck, W. Birmili, M. Hanke, J. Uecker, F. Arnold & M. Kulmala (2005) The contribution of sulphuric acid to atmospheric particle formation and growth: a comparison between boundary layers in Northern and Central Europe. *Atmospheric Chemistry and Physics,* 5**,** 1773-1785.

Flagan, R. C. (1998) History of electrical aerosol measurements. *Aerosol Science and Technology,* 28**,** 301-380.
Fletcher, N. H. (1958) Size Effect in Heterogeneous Nucleation. *Journal of Chemical Physics,* 29**,** 3.
Friedlander, S. K. 1977. *Smoke, dust, and haze : fundamentals of aerosol behavior*. New York: Wiley.
Fuchs, N. A. (1963) ON THE STATIONARY CHARGE DISTRIBUTION ON AEROSOL PARTICLES IN A BIPOLAR IONIC ATMOSPHERE.
Gamero-Castaño, M. & J. F. de la Mora (2000) A CONDENSATION NUCLEUS COUNTER (CNC) SENSITIVE TO SINGLY CHARGED SUB-NANOMETER PARTICLES. *Journal of Aerosol Science,* 31**,** 757-772.
Gamero-Castano, M. & J. F. de la Mora (2000) A condensation nucleus counter (CNC) sensitive to singly charged sub-nanometer particles. *Journal of Aerosol Science,* 31**,** 757-772.
Gelbard, F. & J. H. Seinfeld (1978) Numerical-Solution of Dynamic Equation for Particulate Systems. *Journal of Computational Physics,* 28**,** 357-375.
Gelbard, F. & J. H. Seinfeld (1979) General Dynamic Equation for Aerosols - Theory and Application to Aerosol Formation and Growth. *Journal of Colloid and Interface Science,* 68**,** 363-382.
Ghan, S. J., R. C. Easter, E. G. Chapman, H. Abdul-Razzak, Y. Zhang, L. R. Leung, N. S. Laulainen, R. D. Saylor & R. A. Zaveri (2001) A physically based estimate of radiative forcing by anthropogenic sulfate aerosol. *Journal of Geophysical Research-Atmospheres,* 106**,** 5279-5293.
Gong, W., C. Stroud & L. Zhang (2011) Cloud Processing of Gases and Aerosols in Air Quality Modeling. *Atmosphere* 2**,** 567-616.
Gormley, P. G. (1948) Diffusion from a stream flowing through a cylindrical tube. *Proceedings of the Royal Irish Academy.,* Section C**,** 52(1948):163.
Hagen, D. E. & D. J. Alofs (1983) Linear Inversion Method to Obtain Aerosol Size Distributions from Measurements with a Differential Mobility Analyzer. *Aerosol Science and Technology,* 2**,** 465-475.
Hanson, D. R. & F. L. Eisele (2002) Measurement of prenucleation molecular clusters in the NH3, H2SO4, H2O system. *Journal of Geophysical Research-Atmospheres,* 107.
Hanson, D. R. & E. R. Lovejoy (2006) Measurement of the thermodynamics of the hydrated dimer and trimer of sulfuric acid. *Journal of Physical Chemistry A,* 110**,** 9525-9528.
Hanson, D. R., P. H. McMurry, J. Jiang, R. Stickel, D. Tanner & L. G. Huey (2011a) Ambient Pressure Proton Transfer Mass Spectrometry: Initial Detection of Ammonia and Amines. *Environmental Science & Technology,* 45**,** 8881-8888.
Hanson, D. R., P. H. McMurry, J. Jiang, D. Tanner & L. G. Huey (2011b) Ambient Pressure Proton Transfer Mass Spectrometry: Detection of Amines and Ammonia. *Environmental Science & Technology,* 45**,** 8881-8888.

Hering, S. V., M. R. Stolzenburg, F. R. Quant, D. R. Oberreit & P. B. Keady (2005) A laminar-flow, water-based condensation particle counter (WCPC). *Aerosol Science and Technology,* 39**,** 659-672.

Hidy, G. M. & J. R. Brock. 1970. *The dynamics of aerocolloidal systems*. Oxford ; New York: Pergamon Press.

Hirsikko, A., L. Laakso, U. Horrak, P. P. Aalto, V. M. Kerminen & M. Kulmala (2005) Annual and size dependent variation of growth rates and ion concentrations in boreal forest. *Boreal Environment Research,* 10**,** 357-369.

Hoppel, W. A. & G. M. Frick (1986) Ion Aerosol Attachment Coefficients and the Steady-State Charge-Distribution on Aerosols in a Bipolar Ion Environment. *Aerosol Science and Technology,* 5**,** 1-21.

Hussin, A., H. G. Scheibel, K. H. Becker & J. Porstendorfer (1983) Bipolar Diffusion Charging of Aerosol-Particles .1. Experimental Results within the Diameter Range 4-30-Nm. *Journal of Aerosol Science,* 14**,** 671-677.

Iida, K., M. Stolzenburg, P. McMurry, M. J. Dunn, J. N. Smith, F. Eisele & P. Keady (2006) Contribution of ion-induced nucleation to new particle formation: Methodology and its application to atmospheric observations in Boulder, Colorado. *Journal of Geophysical Research-Atmospheres,* 111**,** -.

Iida, K., M. R. Stolzenburg & P. H. McMurry (2009) Effect of Working Fluid on Sub-2 nm Particle Detection with a Laminar Flow Ultrafine Condensation Particle Counter. *Aerosol Science and Technology,* 43**,** 81-96.

Iida, K., M. R. Stolzenburg, P. H. McMurry & J. N. Smith (2008) Estimating nanoparticle growth rates from size-dependent charged fractions: Analysis of new particle formation events in Mexico City. *Journal of Geophysical Research-Atmospheres,* 113**,** -.

IPCC. 2007. *Climate Change 2007: IPCC Fourth Assessment Report (AR4)*. Cambridge: Cambridge University Press.

Jiang, J., M. Attoui, M. Heim, N. A. Brunelli, P. H. McMurry, G. Kasper, R. C. Flagan, K. Giapis & G. Mouret (2011a) Transfer Functions and Penetrations of Five Differential Mobility Analyzers for Sub-2 nm Particle Classification. *Aerosol Science & Technology,* 45**,** 480-492.

Jiang, J., M. Chen, C. Kuang, M. Attoui & P. McMurry (2011b) Electrical Mobility Spectrometer Using a Diethylene Glycol Condensation Particle Counter for Measurement of Aerosol Size Distributions Down to 1 nm. *Aerosol Science and Technology,* 45**,** 510-521.

Jiang, J., J. Zhao, M. Chen, F. L. Eisele, J. Scheckman, B. J. Williams, C. Kuang & P. H. McMurry (2011c) First Measurements of Neutral Atmospheric Cluster and 1–2 nm Particle Number Size Distributions During Nucleation Events. *Aerosol Science and Technology,* 45**,** 2 - 5.

Jokinen, T., M. Sipilä, H. Junninen, M. Ehn, G. Lönn, J. Hakala, T. Petäjä, R. L. Mauldin Iii, M. Kulmala & D. R. Worsnop (2012) Atmospheric sulphuric acid and neutral cluster measurements using CI-APi-TOF. *Atmos. Chem. Phys.,* 12**,** 4117-4125.

Kazil, J., P. Stier, K. Zhang, J. Quaas, S. Kinne, D. O'Donnell, S. Rast, M. Esch, S. Ferrachat, U. Lohmann & J. Feichter (2010) Aerosol nucleation and its role for

clouds and Earth's radiative forcing in the aerosol-climate model ECHAM5-HAM. *Atmospheric Chemistry and Physics,* 10**,** 10733-10752.
Kerminen, V. M., H. Lihavainen, M. Komppula, Y. Viisanen & M. Kulmala (2005) Direct observational evidence linking atmospheric aerosol formation and cloud droplet activation. *Geophysical Research Letters,* 32**,** -.
Kerminen, V. M., L. Pirjola & M. Kulmala (2001) How significantly does coagulational scavenging limit atmospheric particle production? *Journal of Geophysical Research-Atmospheres,* 106**,** 24119-24125.
Kesten, J., A. Reineking & J. Porstendorfer (1991) Calibration of a Tsi-Model-3025 Ultrafine Condensation Particle Counter. *Aerosol Science and Technology,* 15**,** 107-111.
Kim, C. S., K. Okuyama & J. F. de la Mora (2003) Performance evaluation of an improved particle size magnifier (PSM) for single nanoparticle detection. *Aerosol Science and Technology,* 37**,** 791-803.
Kirkby, J., J. Curtius, J. Almeida, E. Dunne, J. Duplissy, S. Ehrhart, A. Franchin, S. Gagne, L. Ickes, A. Kurten, A. Kupc, A. Metzger, F. Riccobono, L. Rondo, S. Schobesberger, G. Tsagkogeorgas, D. Wimmer, A. Amorim, F. Bianchi, M. Breitenlechner, A. David, J. Dommen, A. Downard, M. Ehn, R. C. Flagan, S. Haider, A. Hansel, D. Hauser, W. Jud, H. Junninen, F. Kreissl, A. Kvashin, A. Laaksonen, K. Lehtipalo, J. Lima, E. R. Lovejoy, V. Makhmutov, S. Mathot, J. Mikkila, P. Minginette, S. Mogo, T. Nieminen, A. Onnela, P. Pereira, T. Petaja, R. Schnitzhofer, J. H. Seinfeld, M. Sipila, Y. Stozhkov, F. Stratmann, A. Tome, J. Vanhanen, Y. Viisanen, A. Vrtala, P. E. Wagner, H. Walther, E. Weingartner, H. Wex, P. M. Winkler, K. S. Carslaw, D. R. Worsnop, U. Baltensperger & M. Kulmala (2011) Role of sulphuric acid, ammonia and galactic cosmic rays in atmospheric aerosol nucleation. *Nature,* 476**,** 429-433.
Knutson, E. O. 1976. Extended Electric Mobility Method for Measuring Aerosol Particle Size and Concentration. In *Fine Particles: Aerosol Generation, Measurement, Sampling, and Analysis,,* ed. B. Y. H. Liu, 739-762. New York: Academic Press.
Korhonen, P., M. Kulmala, A. Laaksonen, Y. Viisanen, R. McGraw & J. H. Seinfeld (1999) Ternary nucleation of H2SO4, NH3, and H2O in the atmosphere. *Journal of Geophysical Research-Atmospheres,* 104**,** 26349-26353.
Kousaka, Y., M. Adachi, K. Okuyama, N. Kitada & T. Motouchi (1983) Bipolar Charging of Ultrafine Aerosol-Particles. *Aerosol Science and Technology,* 2**,** 421-427.
Kovacs, T. A. & W. H. Brune (2001) Total OH loss rate measurement. *Journal of Atmospheric Chemistry,* 39**,** 105-122.
Ku, B. K. & J. F. de la Mora (2009) Relation between Electrical Mobility, Mass, and Size for Nanodrops 1-6.5 nm in Diameter in Air. *Aerosol Science and Technology,* 43**,** 241-249.
Kuang, C. 2009. Atmospheric nucleation: measurements, mechanisms and dynamics University of Minnesota.

Kuang, C., M. Chen, P. H. McMurry & J. Wang (2012a) Modification of Laminar Flow Ultrafine Condensation Particle Counters for the Enhanced Detection of 1 nm Condensation Nuclei. *Aerosol Science and Technology,* 46**,** 309-315.

Kuang, C., M. Chen, J. Zhao, J. Smith, P. H. McMurry & J. Wang (2012b) Size and time-resolved growth rate measurements of 1 to 5 nm freshly formed atmospheric nuclei. *Atmos. Chem. Phys.,* 12**,** 3573-3589.

Kuang, C., P. H. McMurry, A. V. McCormick & F. L. Eisele (2008) Dependence of nucleation rates on sulfuric acid vapor concentration in diverse atmospheric locations. *Journal of Geophysical Research-Atmospheres,* 113.

Kuang, C., I. Riipinen, S. L. Sihto, M. Kulmala, A. V. McCormick & P. H. McMurry (2010) An improved criterion for new particle formation in diverse atmospheric environments. *Atmospheric Chemistry and Physics,* 10**,** 8469-8480.

Kulmala, M., V. M. Kerminen, T. Anttila, A. Laaksonen & C. D. O'Dowd (2004a) Organic aerosol formation via sulphate cluster activation. *Journal of Geophysical Research-Atmospheres,* 109.

Kulmala, M., L. Laakso, K. E. J. Lehtinen, I. Riipinen, M. Dal Maso, T. Anttila, V. M. Kerminen, U. Horrak, M. Vana & H. Tammet (2004b) Initial steps of aerosol growth. *Atmospheric Chemistry and Physics,* 4**,** 2553-2560.

Kulmala, M., K. E. J. Lehtinen & A. Laaksonen (2006) Cluster activation theory as an explanation of the linear dependence between formation rate of 3nm particles and sulphuric acid concentration. *Atmospheric Chemistry and Physics,* 6**,** 787-793.

Kulmala, M., G. Mordas, T. Petaja, T. Gronholm, P. P. Aalto, H. Vehkamaki, A. I. Hienola, E. Herrmann, M. Sipila, I. Riipinen, H. E. Manninen, K. Hameri, F. Stratmann, M. Bilde, P. M. Winkler, W. Birmili & P. E. Wagner (2007a) The condensation particle counter battery (CPCB): A new tool to investigate the activation properties of nanoparticles. *Journal of Aerosol Science,* 38**,** 289-304.

Kulmala, M., U. Pirjola & J. M. Makela (2000) Stable sulphate clusters as a source of new atmospheric particles. *Nature,* 404**,** 66-69.

Kulmala, M., I. Riipinen, M. Sipila, H. E. Manninen, T. Petaja, H. Junninen, M. Dal Maso, G. Mordas, A. Mirme, M. Vana, A. Hirsikko, L. Laakso, R. M. Harrison, I. Hanson, C. Leung, K. E. J. Lehtinen & V. M. Kerminen (2007b) Toward direct measurement of atmospheric nucleation. *Science,* 318**,** 89-92.

Kulmala, M., A. Toivonen, J. M. Makela & A. Laaksonen (1998) Analysis of the growth of nucleation mode particles observed in Boreal forest. *Tellus Series B-Chemical and Physical Meteorology,* 50**,** 449-462.

Kulmala, M., H. Vehkamaki, T. Petaja, M. Dal Maso, A. Lauri, V. M. Kerminen, W. Birmili & P. H. McMurry (2004c) Formation and growth rates of ultrafine atmospheric particles: a review of observations. *Journal of Aerosol Science,* 35**,** 143-176.

Laakso, L., T. Anttila, K. E. J. Lehtinen, P. P. Aalto, M. Kulmala, U. Horrak, J. Paatero, M. Hanke & F. Arnold (2004) Kinetic nucleation and ions in boreal forest particle formation events. *Atmospheric Chemistry and Physics,* 4**,** 2353-2366.

Laaksonen, A., A. Hamed, J. Joutsensaari, L. Hiltunen, F. Cavalli, W. Junkermann, A. Asmi, S. Fuzzi & M. C. Facchini (2005) Cloud condensation nucleus production

from nucleation events at a highly polluted region. *Geophysical Research Letters,* 32**,** -.

Laaksonen, A., M. Kulmala, C. D. O'Dowd, J. Joutsensaari, P. Vaattovaara, S. Mikkonen, K. E. J. Lehtinen, L. Sogacheva, M. Dal Maso, P. Aalto, T. Petaja, A. Sogachev, Y. J. Yoon, H. Lihavainen, D. Nilsson, M. C. Facchini, F. Cavalli, S. Fuzzi, T. Hoffmann, F. Arnold, M. Hanke, K. Sellegri, B. Umann, W. Junkermann, H. Coe, J. D. Allan, M. R. Alfarra, D. R. Worsnop, M. L. Riekkola, T. Hyotylainen & Y. Viisanen (2008) The role of VOC oxidation products in continental new particle formation. *Atmospheric Chemistry and Physics,* 8**,** 2657-2665.

Larriba, C., C. J. Hogan, M. Attoui, R. Borrajo, J. F. Garcia & J. F. de la Mora (2011) The Mobility-Volume Relationship below 3.0 nm Examined by Tandem Mobility-Mass Measurement. *Aerosol Science and Technology,* 45**,** 453-467.

Leaitch, W. R., U. Lohmann, L. M. Russell, T. Garrett, N. C. Shantz, D. Toom-Sauntry, J. W. Strapp, K. L. Hayden, J. Marshall, M. Wolde, D. R. Worsnop & J. T. Jayne (2010) Cloud albedo increase from carbonaceous aerosol. *Atmospheric Chemistry and Physics,* 10**,** 7669-7684.

Lee, K. W., L. A. Curtis & H. Chen (1990) An Analytic Solution to Free-Molecule Aerosol Coagulation. *Aerosol Science and Technology,* 12**,** 457-462.

Lehtinen, K. E. J. & M. Kulmala (2003) A model for particle formation and growth in the atmosphere with molecular resolution in size. *Atmospheric Chemistry and Physics,* 3**,** 251-257.

Liao, H., Y. Zhang, W. T. Chen, F. Raes & J. H. Seinfeld (2009) Effect of chemistry-aerosol-climate coupling on predictions of future climate and future levels of tropospheric ozone and aerosols. *Journal of Geophysical Research-Atmospheres,* 114.

Lihavainen, H., V. M. Kerminen, M. Komppula, J. Hatakka, V. Aaltonen, M. Kulmala & Y. Viisanen (2003) Production of "potential" cloud condensation nuclei associated with atmospheric new-particle formation in northern Finland. *Journal of Geophysical Research-Atmospheres,* 108**,** -.

Liu, B. Y. H. 1976. *Fine particles : aerosol generation, measurement, sampling, and analysis : [papers]*. New York: Academic Press.

Liu, B. Y. H. & C. S. Kim (1977) On the counting efficiency of condensation nuclei counters. *Atmospheric Environment (1967),* 11**,** 1097-1100.

Liu, B. Y. H. & D. Y. H. Pui (1974) A submicron aerosol standard and the primary, absolute calibration of the condensation nuclei counter. *Journal of Colloid and Interface Science,* 47**,** 155-171.

Lohmann, U. & J. Feichter (2005) Global indirect aerosol effects: a review. *Atmospheric Chemistry and Physics,* 5**,** 715-737.

Magnusson, L. E., J. A. Koropchak, M. P. Anisimov, V. M. Poznjakovskiy & J. F. de la Mora (2003) Correlations for vapor nucleating critical embryo parameters. *Journal of Physical and Chemical Reference Data,* 32**,** 1387-1410.

Makela, J. M., M. Dal Maso, L. Pirjola, P. Keronen, L. Laakso, M. Kulmala & A. Laaksonen (2000) Characteristics of the atmospheric particle formation events

observed at a boreal forest site in southern Finland. *Boreal Enviroment Research,* 5**,** 299-313.
Makela, J. M., S. Yli-Koivisto, V. Hiltunen, W. Seidl, E. Swietlicki, K. Teinila, M. Sillanpaa, I. K. Koponen, J. Paatero, K. Rosman & K. Hameri (2001) Chemical composition of aerosol during particle formation events in boreal forest. *Tellus Series B-Chemical and Physical Meteorology,* 53**,** 380-393.
Manninen, H. E., T. Nieminen, I. Riipinen, T. Yli-Juuti, S. Gagne, E. Asmi, P. P. Aalto, T. Petaja, V. M. Kerminen & M. Kulmala (2009) Charged and total particle formation and growth rates during EUCAARI 2007 campaign in Hyytiala. *Atmospheric Chemistry and Physics,* 9**,** 4077-4089.
Matsunaga, A. & P. J. Ziemann (2010) Gas-Wall Partitioning of Organic Compounds in a Teflon Film Chamber and Potential Effects on Reaction Product and Aerosol Yield Measurements. *Aerosol Science and Technology,* 44**,** 881-892.
McGrath, M. J., T. Olenius, I. K. Ortega, V. Loukonen, P. Paasonen, T. Kurtén, M. Kulmala & H. Vehkamäki (2012) Atmospheric Cluster Dynamics Code: a flexible method for solution of the birth-death equations. *Atmos. Chem. Phys.,* 12**,** 2345-2355.
McMurry, P. H. (1980) Photochemical Aerosol Formation from So2 - a Theoretical-Analysis of Smog Chamber Data. *Journal of Colloid and Interface Science,* 78**,** 513-527.
McMurry, P. H. (1983) New Particle Formation in the Presence of an Aerosol - Rates, Time Scales, and Sub-0.01 Mu-M Size Distributions. *Journal of Colloid and Interface Science,* 95**,** 72-80.
McMurry, P. H. (2000) The history of condensation nucleus counters. *Aerosol Science and Technology,* 33**,** 297-322.
McMurry, P. H., M. Fink, H. Sakurai, M. R. Stolzenburg, R. L. Mauldin, J. Smith, F. Eisele, K. Moore, S. Sjostedt, D. Tanner, L. G. Huey, J. B. Nowak, E. Edgerton & D. Voisin (2005) A criterion for new particle formation in the sulfur-rich Atlanta atmosphere. *Journal of Geophysical Research-Atmospheres,* 110**,** -.
McMurry, P. H. & S. K. Friedlander (1978) Aerosol Formation in Reacting Gases - Relation of Surface-Area to Rate of Gas-to-Particle Conversion. *Journal of Colloid and Interface Science,* 64**,** 248-257.
McMurry, P. H. & S. K. Friedlander (1979) New Particle Formation in the Presence of an Aerosol. *Atmospheric Environment,* 13**,** 1635-1651.
McMurry, P. H. & D. J. Rader (1985) Aerosol Wall Losses in Electrically Charged Chambers. *Aerosol Science and Technology,* 4**,** 249-268.
Menon, S., A. D. Del Genio, D. Koch & G. Tselioudis (2002) GCM Simulations of the aerosol indirect effect: Sensitivity to cloud parameterization and aerosol burden. *Journal of the Atmospheric Sciences,* 59**,** 692-713.
Merikanto, J., I. Napari, H. Vehkamaki, T. Anttila & M. Kulmala (2007) New parameterization of sulfuric acid-ammonia-water ternary nucleation rates at tropospheric conditions. *Journal of Geophysical Research-Atmospheres,* 112.
Merikanto, J., D. V. Spracklen, G. W. Mann, S. J. Pickering & K. S. Carslaw (2009) Impact of nucleation on Global CCN. *Atmos. Chem. Phys.,* 9**,** 8601-8616.

Mertes, S., F. Schroder & A. Wiedensohler (1995) The Particle-Detection Efficiency Curve of the Tsi-3010 Cpc as a Function of the Temperature Difference between Saturator and Condenser. *Aerosol Science and Technology,* 23**,** 257-261.

Mordas, G., H. E. Manninen, T. Petaja, P. P. Aalto, K. Hameri & M. Kulmala (2008a) On operation of the ultra-fine water-based CPC TSI3786 and comparison with other TSI models (TSI3776, TSI3772, TSI3025, TSI3010, TSI3007). *Aerosol Science and Technology,* 42**,** 152-158.

Mordas, G., M. Sipila & M. Kulmala (2008b) Nanometer particle detection by the condensation particle counter UF-02proto. *Aerosol Science and Technology,* 42**,** 521-527.

Nair, P. V. N. & K. G. Vohra (1975) Growth of aqueous sulphuric acid droplets as a function of relative humidity. *Journal of Aerosol Science,* 6**,** 265-271.

Nieminen, T., H. E. Manninen, S. L. Sihto, T. Yli-Juuti, R. L. Mauldin, T. Petaja, I. Riipinen, V. M. Kerminen & M. Kulmala (2009) Connection of Sulfuric Acid to Atmospheric Nucleation in Boreal Forest. *Environmental Science & Technology,* 43**,** 4715-4721.

Nowak, J. B., L. G. Huey, A. G. Russell, D. Tian, J. A. Neuman, D. Orsini, S. J. Sjostedt, A. P. Sullivan, D. J. Tanner, R. J. Weber, A. Nenes, E. Edgerton & F. C. Fehsenfeld (2006) Analysis of urban gas phase ammonia measurements from the 2002 Atlanta Aerosol Nucleation and Real-Time Characterization Experiment (ANARChE). *Journal of Geophysical Research-Atmospheres,* 111.

O'Dowd, C., G. McFiggans, D. J. Creasey, L. Pirjola, C. Hoell, M. H. Smith, B. J. Allan, J. M. C. Plane, D. E. Heard, J. D. Lee, M. J. Pilling & M. Kulmala (1999) On the photochemical production of new particles in the coastal boundary layer. *Geophysical Research Letters,* 26**,** 1707-1710.

O'Dowd, C. D., P. Aalto, K. Hameri, M. Kulmala & T. Hoffmann (2002a) Aerosol formation - Atmospheric particles from organic vapours. *Nature,* 416**,** 497-498.

O'Dowd, C. D., K. Hameri, J. M. Makela, L. Pirjola, M. Kulmala, S. G. Jennings, H. Berresheim, H. C. Hansson, G. de Leeuw, G. J. Kunz, A. G. Allen, C. N. Hewitt, A. Jackson, Y. Viisanen & T. Hoffmann (2002b) A dedicated study of New Particle Formation and Fate in the Coastal Environment (PARFORCE): Overview of objectives and achievements. *Journal of Geophysical Research-Atmospheres,* 107.

Okuyama, K., Y. Kousaka, S. Yamamoto & T. Hosokawa (1986) Particle Loss of Aerosols with Particle Diameters between 6 and 2000 Nm in Stirred Tank. *Journal of Colloid and Interface Science,* 110**,** 214-223.

Ortega, I. K., O. Kupiainen, T. Kurtén, T. Olenius, O. Wilkman, M. J. McGrath, V. Loukonen & H. Vehkamäki (2012) From quantum chemical formation free energies to evaporation rates. *Atmos. Chem. Phys.,* 12**,** 225-235.

Paasonen, P., S. L. Sihto, T. Nieminen, H. Vuollekoski, I. Riipinen, C. Plass-Dulmer, H. Berresheim, W. Birmili & M. Kulmala (2009) Connection between new particle formation and sulphuric acid at Hohenpeissenberg (Germany) including the influence of organic compounds. *Boreal Environment Research,* 14**,** 616-629.

Peineke, C., M. B. Attoui & A. Schmidt-Ott (2006) Using a glowing wire generator for production of charged, uniformly sized nanoparticles at high concentrations. *Journal of Aerosol Science,* 37**,** 1651-1661.

Pierce, J. R. & P. J. Adams (2007) Efficiency of cloud condensation nuclei formation from ultrafine particles. *Atmospheric Chemistry and Physics,* 7**,** 1367-1379.

Pierce, J. R. & P. J. Adams (2009) Uncertainty in global CCN concentrations from uncertain aerosol nucleation and primary emission rates. *Atmospheric Chemistry and Physics,* 9**,** 1339-1356.

Premnath, V., D. Oberreit & C. J. Hogan (2011) Collision-Based Ionization: Bridging the Gap between Chemical Ionization and Aerosol Particle Diffusion Charging. *Aerosol Science and Technology,* 45**,** 702 - 716.

Reineking (1986) Measurement of Particle loss Functions in a 3071 DMA for different flow rates. *aerosol Science and Technology*.

Reischl, G. P., J. M. Makela, R. Karch & J. Necid (1996) Bipolar charging of ultrafine particles in the size range below 10 nm. *Journal of Aerosol Science,* 27**,** 931-949.

Riipinen, I., H. E. Manninen, T. Yli-Juuti, M. Boy, M. Sipila, M. Ehn, H. Junninen, T. Petaja & M. Kulmala (2009) Applying the Condensation Particle Counter Battery (CPCB) to study the water-affinity of freshly-formed 2-9 nm particles in boreal forest. *Atmospheric Chemistry and Physics,* 9**,** 3317-3330.

Riipinen, I., S. L. Sihto, M. Kulmala, F. Arnold, M. Dal Maso, W. Birmili, K. Saarnio, K. Teinila, V. M. Kerminen, A. Laaksonen & K. E. J. Lehtinen (2007) Connections between atmospheric sulphuric acid and new particle formation during QUEST III-IV campaigns in Heidelberg and Hyyti. *Atmospheric Chemistry and Physics,* 7**,** 1899-1914.

Riipinen, I., T. Yli-Juuti, J. R. Pierce, T. Petaja, D. R. Worsnop, M. Kulmala & N. M. Donahue (2012) The contribution of organics to atmospheric nanoparticle growth. *Nature Geoscience,* 5**,** 453-458.

Rosser, S. & J. F. de la Mora (2005) Vienna-type DMA of high resolution and high flow rate. *Aerosol Science and Technology,* 39**,** 1191-1200.

Sakurai, H., M. A. Fink, P. H. McMurry, L. Mauldin, K. F. Moore, J. N. Smith & F. L. Eisele (2005) Hygroscopicity and volatility of 4-10 nm particles during summertime atmospheric nucleation events in urban Atlanta. *Journal of Geophysical Research-Atmospheres,* 110.

Saylor, R. D., E. S. Edgerton, B. E. Hartsell, K. Baumann & D. A. Hansen (2010) Continuous gaseous and total ammonia measurements from the southeastern research and characterization (SEARCH) study. *Atmos. Environ.,* 44**,** 4994-5004.

Scheibel, H. G. & J. Porstendorfer (1983) Generation of Monodisperse Ag-Aerosol and Nacl-Aerosol with Particle Diameters between 2-Nm and 300-Nm. *Journal of Aerosol Science,* 14**,** 113-&.

Seinfeld, J. H. & S. N. Pandis. 2006. *Atmospheric chemistry and physics : from air pollution to climate change*. Hoboken, N.J.: J. Wiley.

Sgro, L. A. & J. F. de la Mora (2004) A simple turbulent mixing CNC for charged particle detection down to 1.2 nm. *Aerosol Science and Technology,* 38**,** 1-11.

Sihto, S. L., M. Kulmala, V. M. Kerminen, M. Dal Maso, T. Petaja, I. Riipinen, H. Korhonen, F. Arnold, R. Janson, M. Boy, A. Laaksonen & K. E. J. Lehtinen (2006) Atmospheric sulphuric acid and aerosol formation: implications from atmospheric measurements for nucleation and early growth mechanisms. *Atmospheric Chemistry and Physics,* 6**,** 4079-4091.

Sipila, M., T. Berndt, T. Petaja, D. Brus, J. Vanhanen, F. Stratmann, J. Patokoski, R. L. Mauldin, A. P. Hyvarinen, H. Lihavainen & M. Kulmala (2010) The Role of Sulfuric Acid in Atmospheric Nucleation. *Science,* 327**,** 1243-1246.

Sipila, M., K. Lehtipalo, M. Attoui, K. Neitola, T. Petaja, P. P. Aalto, C. D. O'Dowd & M. Kulmala (2009) Laboratory Verification of PH-CPC's Ability to Monitor Atmospheric Sub-3 nm Clusters. *Aerosol Science and Technology,* 43**,** 126-135.

Smith, J. N., K. C. Barsanti, H. R. Friedli, M. Ehn, M. Kulmala, D. R. Collins, J. H. Scheckman, B. J. Williams & P. H. McMurry (2010) Observations of aminium salts in atmospheric nanoparticles and possible climatic implications. *Proceedings of the National Academy of Sciences of the United States of America,* 107**,** 6634-6639.

Smith, J. N., M. J. Dunn, T. M. VanReken, K. Iida, M. R. Stolzenburg, P. H. McMurry & L. G. Huey (2008) Chemical composition of atmospheric nanoparticles formed from nucleation in Tecamac, Mexico: Evidence for an important role for organic species in nanoparticle growth. *Geophysical Research Letters,* 35**,** -.

Smith, J. N., K. F. Moore, F. L. Eisele, D. Voisin, A. K. Ghimire, H. Sakurai & P. H. McMurry (2005) Chemical composition of atmospheric nanoparticles during nucleation events in Atlanta. *Journal of Geophysical Research-Atmospheres,* 110.

Solomon, P., K. Baumann, E. Edgerton, R. Tanner, D. Eatough, W. Modey, H. Marin, D. Savoie, S. Natarajan, M. B. Meyer & G. Norris (2003) Comparison of integrated samplers for mass and composition during the 1999 Atlanta Supersites project. *Journal of Geophysical Research-Atmospheres,* 108.

Spracklen, D. V., B. Bonn & K. S. Carslaw (2008a) Boreal forests, aerosols and the impacts on clouds and climate. *Philosophical Transactions of the Royal Society a-Mathematical Physical and Engineering Sciences,* 366**,** 4613-4626.

Spracklen, D. V., K. S. Carslaw, M. Kulmala, V. M. Kerminen, S. L. Sihto, I. Riipinen, J. Merikanto, G. W. Mann, M. P. Chipperfield, A. Wiedensohler, W. Birmili & H. Lihavainen (2008b) Contribution of particle formation to global cloud condensation nuclei concentrations. *Geophysical Research Letters,* 35**,** -.

Spracklen, D. V., K. S. Carslaw, J. Merikanto, G. W. Mann, C. L. Reddington, S. J. Pickering, J. A. Ogren, E. Andrews, U. Baltensperger & E. Weingartner (2010) Explaining Global Surface Aerosol Number Concentrations in Terms of Primary Emissions and Particle Formation. *Atmos. Chem. Phys.,* 10**,** 4775-4793.

Stieb, D. M., M. Smith-Doiron, J. R. Brook, R. T. Burnett, T. Dann, A. Mamedov & Y. Chen (2002) Air pollution and disability days in Toronto: Results from the National Population Health Survey. *Environmental Research,* 89**,** 210-219.

Stolzenburg, M. R. 1988. An ultrafine aerosol size distribution measuring system. University of Minnesota, Minneapolis.

Stolzenburg, M. R. & P. H. McMurry (1991) An Ultrafine Aerosol Condensation Nucleus Counter. *Aerosol Science and Technology,* 14**,** 48-65.
Stolzenburg, M. R. & P. H. McMurry (2008) Equations governing single and tandem DMA configurations and a new lognormal approximation to the transfer function. *Aerosol Science and Technology,* 42**,** 421-432.
Stolzenburg, M. R., P. H. McMurry, H. Sakurai, J. N. Smith, R. L. Mauldin, F. L. Eisele & C. F. Clement (2005) Growth rates of freshly nucleated atmospheric particles in Atlanta. *Journal of Geophysical Research-Atmospheres,* 110**,** -.
Strey, R., P. E. Wagner & Y. Viisanen (1994) The Problem of Measuring Homogeneous Nucleation Rates and the Molecular Contents of Nuclei - Progress in the Form of Nucleation Pulse Measurements. *Journal of Physical Chemistry,* 98**,** 7748-7758.
Svenningsson, B., A. Arneth, S. Hayward, T. Holst, A. Massling, E. Swietlicki, A. Hirsikko, H. Junninen, I. Riipinen, M. Vana, M. Dal Maso, T. Hussein & M. Kulmala (2008) Aerosol particle formation events and analysis of high growth rates observed above a subarctic wetland-forest mosaic. *Tellus Series B-Chemical and Physical Meteorology,* 60**,** 353-364.
Tammet, H. (1995) Size and Mobility of Nanometer Particles, Clusters and Ions. *Journal of Aerosol Science,* 26**,** 459-475.
Thomson, J. J. 1906. *Conduction of electricity through gases*. Cambridge,: University press.
Thomson, W. (1870) On the Equilibrium if Vapour at a. Curved Surface of Liquid. *Proceedings of the Royal Society of Edinburgh,* 7**,** 63-67.
Titcombe, M. 2012. New Particle Formation: Sulfuric Acid and Amine Chemical Nucleation, Photochemical Reaction Chamber Studies and the Laboratory Cluster-CIMS.
Ude, S. & J. F. de la Mora (2005) Molecular monodisperse mobility and mass standards from electrosprays of tetra-alkyl ammonium halides. *Journal of Aerosol Science,* 36**,** 1224-1237.
Vakeva, M., K. Hameri, T. Puhakka, E. D. Nilsson, H. Hohti & J. M. Makela (2000) Effects of meteorological processes on aerosol particle size distribution in an urban background area. *Journal of Geophysical Research-Atmospheres,* 105**,** 9807-9821.
Vanhanen, J., J. Mikkilä, K. Lehtipalo, M. Sipilä, H. E. Manninen, E. Siivola, T. Petäjä & M. Kulmala (2011) Particle Size Magnifier for Nano-CN Detection. *Aerosol Science and Technology,* 45**,** 533 - 542.
Vehkamaki, H., M. Kulmala, I. Napari, K. E. J. Lehtinen, C. Timmreck, M. Noppel & A. Laaksonen (2002) An improved parameterization for sulfuric acid-water nucleation rates for tropospheric and stratospheric conditions. *Journal of Geophysical Research-Atmospheres,* 107.
Wang, M. & J. E. Penner (2009) Aerosol Indirect Forcing in a Global Model with Particle Nucleation. *Atmos. Chem. Phys.,* 9**,** 239-260.
Wang, S. C. & R. C. Flagan (1990) Scanning Electrical Mobility Spectrometer. *Aerosol Sci. Tech.,* 13**,** 230-240.

Wang, Z. B., M. Hu, D. L. Yue, J. Zheng, R. Y. Zhang, A. Wiedensohler, Z. J. Wu, T. Nieminen & M. Boy (2011) Evaluation on the role of sulfuric acid in the mechanisms of new particle formation for Beijing case. *Atmos. Chem. Phys.,* 11**,** 12663-12671.

Weber, R. J., J. J. Marti, P. H. McMurry, F. L. Eisele, D. J. Tanner & A. Jefferson (1996) Measured atmospheric new particle formation rates: Implications for nucleation mechanisms. *Chemical Engineering Communications,* 151**,** 53-64.

Weber, R. J., J. J. Marti, P. H. McMurry, F. L. Eisele, D. J. Tanner & A. Jefferson (1997) Measurements of new particle formation and ultrafine particle growth rates at a clean continental site. *Journal of Geophysical Research-Atmospheres,* 102**,** 4375-4385.

Weber, R. J., P. H. McMurry, L. Mauldin, D. J. Tanner, F. L. Eisele, F. J. Brechtel, S. M. Kreidenweis, G. L. Kok, R. D. Schillawski & D. Baumgardner (1998) A study of new particle formation and growth involving biogenic and trace gas species measured during ACE 1. *Journal of Geophysical Research-Atmospheres,* 103**,** 16385-16396.

Wichmann, H. E. & A. Peters (2000) Epidemiological evidence of the effects of ultrafine particle exposure. *Philosophical Transactions of the Royal Society of London Series a-Mathematical Physical and Engineering Sciences,* 358**,** 2751-2768.

Wiedensohler, A. (1988) An Approximation of the Bipolar Charge-Distribution for Particles in the Sub-Micron Size Range. *Journal of Aerosol Science,* 19**,** 387-389.

Wiedensohler, A. & H. J. Fissan (1991) Bipolar Charge-Distributions of Aerosol-Particles in High-Purity Argon and Nitrogen. *Aerosol Science and Technology,* 14**,** 358-364.

Wilson, C. T. R. (1899) On the Comparative efficiency as Condensation Nuclei of Positively and Negatively Charged Ions. *London Philos. Trans.***,** 289-308.

Winkler, P. M., G. Steiner, A. Vrtala, G. P. Reischl, M. Kulmala & P. E. Wagner (2011) Unary and Binary Heterogeneous Nucleation of Organic Vapors on Monodisperse WO(x) Seed Particles with Diameters Down to 1.4 nm. *Aerosol Science and Technology,* 45**,** 493-498.

Winkler, P. M., G. Steiner, A. Vrtala, H. Vehkamaki, M. Noppel, K. E. J. Lehtinen, G. P. Reischl, P. E. Wagner & M. Kulmala (2008) Heterogeneous nucleation experiments bridging the scale from molecular ion clusters to nanoparticles. *Science,* 319**,** 1374-1377.

Winkler, P. M., A. Vrtala, G. Steiner, D. Wimmer, H. Vehkamaki, K. E. J. Lehtinen, G. P. Reischl, M. Kulmala & P. E. Wagner (2012) Quantitative Characterization of Critical Nanoclusters Nucleated on Large Single Molecules. *Physical Review Letters,* 108.

Woo, K. S., D. R. Chen, D. Y. H. Pui & P. H. McMurry (2001) Measurement of Atlanta aerosol size distributions: Observations of ultrafine particle events. *Aerosol Science and Technology,* 34**,** 75-87.

Yli-Juuti, T., T. Nieminen, A. Hirsikko, P. P. Aalto, E. Asmi, U. Horrak, H. E. Manninen, J. Patokoski, M. Dal Maso, T. Petaja, J. Rinne, M. Kulmala & I. Riipinen (2011) Growth rates of nucleation mode particles in Hyytiala during 2003-2009:

variation with particle size, season, data analysis method and ambient conditions. *Atmospheric Chemistry and Physics,* 11**,** 12865-12886.
Yu, H., R. McGraw & S. H. Lee (2012) Effects of amines on formation of sub-3 nm particles and their subsequent growth. *Geophysical Research Letters,* 39.
Zhang, Y., P. Liu, X.-H. Liu, M. Z. Jacobson, P. H. McMurry, Q. Fang, P. V. Bhave, S. Yu & K. L. Schere (2010a) A comparative study of homogeneous nucleation parameterizations, Part II. 3-D Model simulations and evaluation. *Journal of Geophysical Research,* 115**,** D20213.
Zhang, Y., X. Y. Wen & C. J. Jang (2010b) Simulating chemistry–aerosol–cloud–radiation–climate feedbacks over the continental U.S. using the online-coupled Weather Research Forecasting Model with chemistry (WRF/Chem). *Atmospheric Environment,* 44**,** 3568-3582.
Zhao, J., F. L. Eisele, M. Titcombe, C. G. Kuang & P. H. McMurry (2010) Chemical ionization mass spectrometric measurements of atmospheric neutral clusters using the cluster-CIMS. *Journal of Geophysical Research-Atmospheres,* 115**,** -.
Zhao, J., J. N. Smith, F. L. Eisele, M. Chen, C. Kuang & P. H. McMurry (2011) Observation of neutral sulfuric acid-amine containing clusters in laboratory and ambient measurements. *Atmospheric Chemistry and Physics,* 11**,** 10823-10836.
Zollner, J. H., W. A. Glasoe, B. Panta, K. K. Carlson, P. H. McMurry & D. R. Hanson (2012) Sulfuric acid nucleation: power dependencies, variation with relative humidity, and effect of bases. *Atmos. Chem. Phys.,* 12**,** 4399-4411.